DISSERTATION

A MULTISCALE PERSPECTIVE ON CONVECTIVE STORMS IN SOUTH AMERICA: FROM TORNADIC ENVIRONMENTS TO INTRASEASONAL MODULATION AND FUTURE CHANGES

Submitted by

Daniel Sebastián Veloso Águila

Department of Atmospheric Science

In partial fulfillment of the requirements

For the Degree of Doctor of Philosophy

Colorado State University

Fort Collins, Colorado

Spring 2026

Ph.D's Committee:

Co-Advisor: Eric D. Maloney
Co-Advisor: Kristen L. Rasmussen

James W. Hurrell
Delphine K. Farmer

Copyright by Daniel Sebastián Veloso Águila 2026

All Rights Reserved

ABSTRACT

A MULTISCALE PERSPECTIVE ON CONVECTIVE STORMS IN SOUTH AMERICA: FROM TORNADIC ENVIRONMENTS TO INTRASEASONAL MODULATION AND FUTURE CHANGES

Convective storms are a key component of the Earth's climate system, producing a significant fraction of global precipitation, and are often associated with severe weather, including flash floods, large hail, and strong winds. While convection is a global phenomenon, its nature is strongly modulated by geographical characteristics. South America is a natural laboratory for studying a wide spectrum of convective storms, including some of the planet's most intense convective storms. The uniqueness of this region is defined by its vast meridional extension (12°N–55°S), which fosters a broad range of climatic regimes, and by its complex geography, dominated by features such as the Amazon rainforest and the Andes mountains.

This dissertation provides a comprehensive, multi-scale investigation into the convective storms of South America, examining their behavior in the present-day climate, their modulation by subseasonal variability, and their projected response to global warming. By integrating satellite observations, reanalysis products, and convection-permitting climate modeling, this work addresses critical gaps in the understanding of high-impact weather in a vulnerable and understudied region.

First, an analysis of the environment supporting tornadoes in southeast South America (SESA) is presented. Based on a self-constructed database and ERA5 reanalysis, this work identifies the key ingredients for tornadogenesis at multiple timescales. The proximity

environment before and during tornado occurrence depicts enhanced instability, deep-layer wind shear, storm-relative helicity, reduced convective inhibition, and a lowered lifting condensation level. At the synoptic scale, tornado events are linked to a strong anomalous trough crossing the Andes, and the subsequent strengthening of the South American low-level jet that increases moisture advection supporting deep convection in the subtropics. At planetary scales, the environment is preconditioned by Rossby wave trains originated a few weeks prior to tornado occurrence in the western Pacific, and preferred Madden-Julian Oscillation (MJO) phase 3. This study reveals a complex interplay of processes that foster severe weather as well as potential for predictability a few weeks in advance.

Second, the influence of the MJO on austral summer convective storms is explored in South America. In tropical South America, MJO wind anomalies circumnavigating the tropics directly modulate the large-scale circulation and thermodynamics over the continental land, enhancing column moisture and precipitation during MJO phases 8 and 1, and bringing opposite conditions during phases 3 to 5. This modulation translates to distinct changes in individual storm structures in central and eastern tropical South America, with MJO phases 8 and 1 favoring wider and shallower storms that produce more rain, while phases 3 to 5 favor deeper and narrower storms. This connection establishes a critical link between subseasonal variability and storm-scale behavior, suggesting a potential pathway for improved predictability.

Finally, this dissertation investigates future changes in austral summer precipitation and storm characteristics using a long-term, high-resolution, convection-permitting climate simulation over South America. Using a pseudo-global warming approach, the model projects a continental shift toward less frequent but more intense precipitation, predominantly over tropical South America. This change is driven by an increase in the occurrence and total rainfall of storms

containing intense deep convective cores. This transition toward more deep convective cores at the expense of moderate wide convective systems is consistent with a projected increase in atmospheric instability (CAPE) across the continent.

Collectively, this research advances the fundamental understanding of the atmospheric processes governing convective storms in South America. By characterizing the present-day severe weather environment, identifying key sources of subseasonal predictability, and projecting future changes in extreme convective storms, this dissertation provides crucial insights into the evolving nature of high-impact weather in the region.

ACKNOWLEDGEMENTS

I would like to thank my advisors Eric Maloney and Kristen Rasmussen. Thank you for considering my application to CSU and offer me the opportunity to work with you despite that I was looking to work with another faculty on a different topic. Thank you both for working with me despite my non-traditional background as international and parent student. Thank you, Eric, for your scientific insight and perspective during all these years, especially when I jumped into tropical processes in South America and needed some additional guidance in a topic that was completely new for me. Thank you, Kristen, not only for your scientific insight as my advisor but also for being a great mentor during all these years. Thank you for your always keep track of my progress and constantly remind me about the big picture/hourglass perspective. Your scientific insight and great ideas really helped me to find ways to conduct my research. I will always be deeply grateful for all your career advice, the professional development sessions, and constant encouragement and support that went beyond my expectations.

I thank the community at the Department of Atmospheric Science at CSU, for being such a inclusive and supportive environment where I have always felt welcome.

I also thank the Department of Geophysics at the University of Concepcion in Chile, all the faculty, staff, and classmates that created a great learning environment and the best preparation possible to pursue graduate studies anywhere on the planet. In particular, I thank my undergraduate advisor and mentor, Aldo Montecinos (RIP) who was the person that ignited a passion in me for scientific research and atmospheric sciences. Thank you being a great teacher and the best mentor I could have asked for. I will always be grateful with you and I will keep your academic and life teachings with me.

I also thank my parents, Ivette and Juan. Gracias por darme la vida, por haberme cuidado y criado. Gracias por enseñarme a ser disciplinado y perseverante, y nunca restringirme en mis sueños y metas. También agradezco a mis hermanos, Leandro y Cindy, por su apoyo y amor durante los años que estado lejos de casa.

Finally, I thank my wife, Macarena, for her unconditional love and support, and her company during all these years living on Fort Collins. You were a cornerstone in this accomplishment, there is no way I could have successfully reached the finish line without your help. Te amo Chita.

DEDICATION

Este logro va dedicado para ti "pelaito", donde sea que estes en tu descanso eterno…

TABLE OF CONTENTS

CHAPTER 1

Introduction

1.1 Motivation

Convective storms are an important component of the global hydrological cycle. The nature of convection varies depending on multiple factors, which include the presence of continental landmasses, the proximity to major mountain ranges, sources of atmospheric moisture, the surrounding ocean temperature, the proximity to the equator, among others. While shallow and isolated storms are predominant over oceans, the deepest and most severe storms usually occur over continents (Zipser et al. 2006; Houze et al. 2015).

In South America, convective storms predominate as the main source of precipitation during the warm season. However, regional differences in the nature of convection are evident between the tropics and subtropics (Romatschke and Houze 2013). Tropical South America is home to the Amazon rainforest, where incoming solar radiation, dense vegetation, and atmospheric moisture are abundant, creating a maritime-like environment where congestus clouds and large mesoscale convective systems are favored and severe thunderstorms are uncommon (Williams et al. 2002; Wall et al. 2013). In subtropical South America, some of the most intense thunderstorms on Earth take place (Zipser et al. 2006) thanks to the sporadic transport of tropical moisture by the South American low-level jet (SALLJ, Vera et al. 2006; Montini et al. 2019; Sasaki et al. 2022; Jones et al. 2023) and a capping inversion induced by the Andes mountains that prevents the quick release of convective potential energy (Ribeiro and Bosart 2018).

Remote teleconnections can induce variability in summer convection over South America. Atmospheric waves excited by convection over the Indo-Pacific warm pool travel eastward, reaching South America and altering the large-scale tropical environment (Grimm and Ambrizzi 2009; Grimm 2019). Many studies have shown the propagation of extratropical Rossby wave trains influencing the atmospheric environments in the subtropics of South America (e.g., Alvarez et al. 2016; Rondanelli et al. 2019; Grimm 2019; Recalde-Coronel et al. 2020). The Madden-Julian Oscillation (MJO) is one of the main sources of teleconnection patterns on intraseasonal timescales in South America (Alvarez et al. 2017). Although it is expected that an MJO-induced modification of the atmospheric environment could alter the behavior of convective storms, such studies have mainly focused on the MJO modulation of daily temperatures, daily precipitation, or extreme precipitation events (De Souza and Ambrizzi 2006; Alvarez et al. 2016; Grimm 2019). It is unknown how the MJO could affect the general structure and intensity of convective storms in South America, which could help determine periods where storms could be benign or present severe impacts on population and property.

One of the main challenges that has complicated the comprehension of convective storms in South America is the lack of continuous observational records across the continent, along with the lack of a robust severe storm reporting system. The emergence of spaceborne radar observations from satellites such as TRMM (Kummerow et al. 1998) and GPM (Hou et al. 2014) with coverage over the global tropics and subtropics has increased our understanding in convective storms over the continent (Romatschke and Houze 2010; Rasmussen and Houze 2011; Romatschke and Houze 2013; Rasmussen et al. 2016, among others). However, the lack of continuous coverage in time and space and limited accuracy in comparison with ground-based radars limits the ability to conduct robust climatological studies.

One solution to address these sampling and coverage issues is the use of climate modeling. Global circulation models (GCMs) and regional climate models (RCMs) have been widely used in South America to reproduce precipitation events (da Rocha et al. 2009; Solman and Blázquez 2019; Bettolli et al. 2021). However, these simulations present large biases in the representation of certain aspects of South America's hydroclimate, particularly those at coarser resolutions and involving deep convection in areas with complex topography or large surface heterogeneities (López-Franca et al. 2016; Solman and Blázquez 2019; Pabón-Caicedo et al. 2020). Recent efforts made by the South America Affinity Group (SAAG) have concluded with the development of the first very high-resolution, convection-permitting, multidecadal climate simulation for South America (SAAG-CTL, Dominguez et al. 2024). This SAAG simulation outperforms GCMs and RCMs in reproducing precipitation over parts of tropical and subtropical South America (Paccini and Stevens 2023; Zilli et al. 2024).

Climate models can also be used to examine projected future changes in South American precipitation and convective storms. While several studies have addressed future changes in precipitation across different parts of the continent (Zaninelli et al. 2019; Pabón-Caicedo et al. 2020; Alves et al. 2021; Reboita et al. 2022a,b, among others), very few studies have explored these changes using convection-permitting climate simulations (e.g., Halladay et al. 2023). SAAG conducted an additional convection-permitting climate simulation that used the pseudo-global warming approach (PGW, Schär et al. 1996) to model a future climate scenario for South America (SAAG-PGW, Dominguez et al. 2024). This simulation can be used not only to explore changes in precipitation with the added value that a storm-resolving simulation can offer, but also changes in the three-dimensional characteristics of convective storms, which has not been examined before in South America.

The objective of this dissertation is to increase our understanding of convective storms in South America, how they are influenced by atmospheric processes acting at multiple spatiotemporal scales, and how they are expected to change under a warmer climate. By describing the environments that support severe thunderstorms and different storm structures, assessing the role of large-scale climate drivers such as the MJO in modulating those environments, and projecting future changes in extreme convective storms based on a PGW convection-permitting climate simulation, this work provides a potential pathway for improving the prediction of severe weather risk, offering valuable lead time for emergency preparedness and risk mitigation.

1.2 Dissertation outline

The comprehensive investigation of different aspects of convective storms in South America developed through this dissertation has generated multiple peer-reviewed publications that are included or previewed here. Chapter 2 is a published paper (Veloso-Aguila et al. 2024), Chapter 3 is a submitted paper that is currently under a second round of revisions (Veloso-Aguila et al. 2025a), and Chapter 4 is a manuscript to be submitted by the end of 2025 (Veloso-Aguila et al. 2025b). Each study is presented in complete form, including an introduction, methods, results (containing figures), and conclusion sections.

Chapter 2 (Veloso-Aguila et al. 2024) was published in *Monthly Weather Review*[1] and describes what atmospheric conditions (from mesoscale to planetary scales) are present prior to and during tornadic storms impacting southeast South America (SESA), based on a self-constructed database of tornado reports and reanalysis data. This is one of the first studies to explore the modulation by the MJO of the occurrence of tornadoes in South America, linking

[1] Included with the permission of the American Meteorological Society

Rossby waves excited in the tropical western Pacific at one-to-two-week lead times with tornado occurrence.

Chapter 3 (Veloso-Aguila et al. 2025a, under review) was submitted to the *Journal of the Atmospheric Sciences* and explores how intraseasonal variability associated with the MJO can influence summer convective activity over South America. The MJO teleconnections induce periods where storms in central and eastern tropical South America are shallower and wider, thus favoring more extensive rainfall accumulation (i.e., enhanced flooding risk over a large area), and others where storms in that region are taller and narrower, thus causing intense but less extensive rainfall accumulation (i.e., enhanced severe storm impacts).

Chapter 4 (Veloso-Aguila et al. 2025b, in preparation) investigates future changes in austral summer precipitation and extreme storm characteristics over South America using a 22-year, high-resolution (4-km) convection-permitting climate simulation run by SAAG under both present and future climate conditions. The results suggest a future shift toward storms containing more intense cores that produce larger amounts of volumetric rainfall in tropical and subtropical South America, which appears to be driven by increased instability across the continent.

Chapter 5 presents a summary of the combined conclusions from Chapters 2-4.

CHAPTER 2

Tornadoes in Southeast South America: Mesoscale to Planetary-Scale Environments[2]

2.1 Introduction

Severe thunderstorms cause extensive damage to property and devastating loss of human life. The exposure to severe storms has substantially increased during the last few decades and is expected to continue rising in the future. Among the main reasons explaining this are changes in population dynamics and extreme weather events caused by climate change (Yang et al. 2019; Swain et al. 2020; Tuholske et al. 2021), which are increasing monetary losses (Bouwer 2019) and disaster risk (IPCC 2012) worldwide. Tornadic storms have been extensively studied in the United States, where robust observing networks and advances in numerical weather prediction models allow tornado threats to be anticipated with reasonable accuracy (Brotzge and Donner 2013; Brooks and Correia 2018). Other regions such as South America do not have dense observational networks (including vertical soundings and ground-based radars) nor routine collection and archiving of severe weather reports, contributing to a lack of studies about and limiting advanced warning of these life-threatening events (Nascimento and Doswell 2006).

South America is prone to some of the most intense severe thunderstorms globally (Zipser et al. 2006; Cecil and Blankenship 2012; Houze et al. 2015) including tornadoes (Goliger and Milford 1998; Brooks et al. 2003). The environments that support the formation of tornadoes are generally located east of major mountain ranges (e.g., the Rockies and the Andes), where severe

[2] The work presented in Chapter 2 was published in *Monthly Weather Review* in 2024 as: Veloso-Aguila, D., K. L. Rasmussen, and E. D. Maloney, 2024: Tornadoes in Southeast South America: Mesoscale to Planetary-Scale Environments. *Monthly Weather Review*, **152**, 295–318, https://doi.org/10.1175/MWR-D-22-0248.1.

weather conditions are frequent during the warm season (Zipser et al. 2006; Houze et al. 2015). In SESA, conditions favoring severe weather are supported by a poleward-extended low-level jet (i.e., South American low-level jet [SALLJ; Vera et al. 2006; Montini et al. 2019; Sasaki et al. 2022]), often enhanced by a synoptic trough, which helps to destabilize the environment by advecting warm and humid air from the Amazon basin (Rasmussen and Houze 2016). Dry westerly flow crossing the mountains can override this low-level meridional moisture flux, creating steep mid-level lapse rates (Banacos and Ekster 2010; Ribeiro and Bosart 2018), with a capping inversion downstream that prevents widespread convection (Rasmussen and Houze 2011, 2016). The synoptic forcing also produces strong midlevel vertical wind shear (Piersante et al. 2021), a key ingredient for mesoscale convective systems (MCSs) that are often initiated along the foothills of the Andes and the Sierras de Córdoba (hereafter SDC) that help to overcome the capping.

Tornadoes have been frequently observed in SESA (Schwarzkopf 1988; Nunes et al. 2011; Silva Dias 2011; Rasmussen et al. 2014), but it is difficult to determine how frequent they are relative to other regions of the world, as the reporting procedures are different, the observational network in SESA is very sparse, and early estimates are likely biased by low reporting numbers in low population regions (e.g., throughout the Pampas of Argentina [Potvin et al. 2022]). Tornado occurrence in SESA is assumed to be lower than in the U.S., where the number of reports is typically over 1000 per year (https://www.ncdc.noaa.gov/societal-impacts/tornadoes/), even though the U.S. tornado reports have increased over time due to greater population growth, installation of a dense radar network beginning in the 1980's, and other factors (Nouri et al. 2021; Potvin et al. 2022). In terms of tornado environments, Brooks et al. (2003) used the ingredients that support significant tornado events in the U.S. to estimate tornado frequency across the globe based on reanalysis data. Their findings suggest that tornadoes over SESA are less frequent than in the U.S., although extrapolating the same parameters that favor tornadic storms in the United States to South America may be a poor assumption due to differences in environmental forcing and topography, among other factors. A more detailed and modern study of mesoscale through planetary-scale environments supporting the occurrence of tornadic storms is necessary for improved understanding of severe weather in this region. In this context, the emergence of novel reanalysis products such as ERA5 (Hersbach et al. 2020) have been useful in representing convective environments associated with tornadoes in the U.S. and Europe with high accuracy (Taszarek et al. 2020, 2021; Coffer et al. 2020; Varga and Breuer 2022) and may prove similarly useful for SESA.

Numerous tornado case studies for South America have been conducted, including Brazil (Lima 1982; Oliveira 2004; Nascimento et al. 2014; Rehbein et al. 2018; Pereira Filho et al. 2019; Lopes and Nascimento 2020; Nunes et al. 2021; Oliveira et al. 2022); Argentina (Schwarzkopf and Rosso 1993; Natalini et al. 2012; Pita and Schwarzkopf 2016); Uruguay (DNM 2002; Durañona 2016; http://tornadoseneluruguay.blogspot.com/); Colombia (Ortiz-Royero and Rosales 2012); and Chile (Barrett et al. 2020, Vicencio et al. 2021). However, very few studies have focused on climatological aspects of tornado reports and their intensities (Schwarzkopf 1988; Nunes et al. 2011; Silva Dias 2011; Rasmussen et al. 2014; Lopes 2020), and virtually no studies exist on the environments supporting tornadic storms. Schwarzkopf (1988) conducted the first effort in materializing a tornado database in SESA by compiling hundreds of carefully identified reports between 1930 and 1987. More recently, through local newspapers, Rasmussen et al. (2014) compiled several tornado storm reports that occurred in central and northeastern Argentina since 1997 and were observed by the TRMM satellite's Precipitation Radar. Further efforts from local scientists have made it possible to compile historical reports of tornadoes in Brazil (Nunes et al.

2011; Silva Dias 2011) and Chile (Vicencio et al. 2021), including analysis of tornado distribution and intensity. Vicencio et al. (2021) found that an extended period of postfrontal activity with modest instability (<1000 J/kg) and strong low- and mid-level shear was instrumental for a cold-season tornado outbreak in Chile. Beyond these limited efforts, there are no formal studies specifically addressing the general environment supportive of tornadoes using an ingredients-based approach (Doswell et al. 1996) for severe thunderstorms in SESA.

Teleconnections associated with large-scale modes of variability such as El Niño-Southern Oscillation (ENSO) and the Madden-Julian Oscillation (MJO) can also affect the local conditions that support severe weather. For example, the Pacific-South America (PSA) teleconnection pattern can be modulated by ENSO that affects the strength of the SALLJ and associated mesoscale convective systems (e.g., Silva and Ambrizzi 2006; Montini et al. 2019). Changes in extreme precipitation and the characteristics of convection in SESA have been documented through such ENSO teleconnections (e.g., Grimm and Tedeschi 2009; Bruick et al. 2019). The MJO can similarly excite extratropical teleconnections that modulate circulations and precipitation in South America (Carvalho et al. 2004; Alvarez et al. 2016). Teleconnections from the tropics associated with phenomena like ENSO and the MJO have been extensively documented to modulate severe weather and tornadoes over North America (e.g., Tippett 2018; Thompson and Roundy 2013; Baggett et al. 2018), but little work has been done in South America (e.g., Barrett et al. 2020).

A key objective of this study is to determine what environmental conditions support tornadoes in SESA at various scales, contrasting with tornadoes in the U.S. given the apparent differences in frequency between these two regions. We will address the following questions: What dynamic or thermodynamic parameters are important for tornadogenesis in SESA at the mesoscale? What synoptic conditions favor the formation of tornadoes in SESA? How important is planetary-scale forcing for modulating tornadic storms with implications for predicting their occurrence in SESA? Are there any tropical sources of predictability for tornadic storms in SESA? To address these questions, Chapter 2.2 will describe the data and methods used to describe the tornadic environment over SESA using a compendium of tornado reports in the region; Chapter 2.3 will examine tornado distributions and storm mode characteristics; Chapter 2.4 will address the mesoscale environment supporting tornadoes and discussion of differences and similarities between the environments supporting tornadic storms in SESA and the U.S.; Chapter 2.5 will address synoptic- and planetary-scale forcing (including teleconnections) modulating the environment conducive to tornadic storms. Finally, Chapter 2.6 will present the main conclusions of the study.

2.2 Methodology

2.2.1 Tornado Event Climatology

Given that no official severe weather report database (including tornadoes) exists in South America, we performed a full search of digital newspaper archives, social media, and other online sources to create a database of tornadic events in subtropical South America after 1991. This effort resulted in a compendium of 74 tornadic events spanning Argentina, Paraguay, Uruguay, and southern Brazil, between 1991 and 2020 (Veloso-Aguila 2024). Most of the reports are from Argentina and Uruguay, as can be seen in Figure 2.1. It is important to note that not all the reports we use experience the same rigorous quality control that is conducted within the U.S., for example, by the National Weather Service. Most of the reports were collected from an anonymous online repository that assembled confirmed and unconfirmed events in Argentina, Brazil, Paraguay, and Uruguay, using the *Google My Maps* Application (https://www.google.com/maps/d/viewer?mid=1E_a0e2B9ftXNQ-F5XIZgnGps2So&usp=sharing). Nonetheless, supporting details were needed due to the lack of evidence to validate many of these reports. Thus, numerous events were confirmed by using information about tornado events shared by meteorology enthusiasts (who occasionally included data from radar and satellite imagery) in an online meteorology forum (http://foro.gustfront.com.ar/). Individual efforts from meteorologists who gathered evidence (pictures and videos) and visited the damaged area to confirm the occurrence of a tornado in a specific location, and shared the information in personal blogs (e.g., http://tornadoseneluruguay.blogspot.com/), were also included. Clock changes due to daylight saving time and other factors across the South American countries were also considered to preserve correct conversion to UTC time when required. A table with detailed information on every tornado event used in this study is found in Veloso-Aguila (2024), including online sources of information that confirm the occurrence of every single case, approximate location, any available intensity information, and time of occurrence.

It is important to point out that the actual number of reports collected for the present study was much higher. However, the lack of information such as the time of occurrence that is required to conduct hourly analysis, approximate location of the event, or strong visual evidence of the funnel cloud or the damage caused required to label the event as a tornado (e.g., local people sometimes confuse a tornado with strong straight-line winds) prevented us from building a larger database. Due to time constraints, we were also not able to explore all tornado events in southern Brazil, so we only included two of the dozens of potential reports in our database. Consequently, we do not accurately represent the tornado environment in southern Brazil, but the reader can refer to Silva Dias (2011) or Lopes (2020) for further information over that region. Another aspect that reduced the total number of reports was that we only selected a single report within an outbreak to provide equal weighting to environmental conditions when composites were calculated. As a result, the distribution of the events shown in Figure 2.1 may not be representative of the actual density of tornadoes in SESA.

2.2.2 ERA5

Hourly ERA5 reanalysis (Hersbach et al. 2020) is used to characterize the mesoscale and large-scale environments associated with the tornado events. ERA5 is the fifth-generation reanalysis product from ECMWF, covering the period 1979-2021 with 0.25ºx0.25º horizontal grid spacing. Composite anomalies of the synoptic and large-scale environments supporting tornadic storms are calculated using data on single levels (e.g., vertically-integrated or surface fields) and pressure levels (upper-air fields). Differences relative to the long-term means are used to calculate daily anomalies based on the climatological period of 1991-2020, the same period of the reported tornadoes used here. In addition, model-level ERA5 data were employed, which has a higher vertical resolution (137 vs. 37 levels) and terrain-following coordinates, thus allowing a more precise calculation of some convective parameters. Proximity soundings were obtained using the closest ERA5 grid point to every tornado report at the closest time and time-evolution composites spanning 24 hours before and after the event were obtained by applying the same approach. A sensitivity test of the results to be presented in Chapter 3.4 that considered the average of the closest 25 grid points to every tornado as the proximity sounding showed negligible differences with the closest grid point approach (not shown). Around 10% of the proximity soundings at the closest time of tornado occurrence show some evidence of potential convective contamination (e.g., cold pool sampling or deep saturated layer). Composite analyses removing those cases show a significant, but small impact overall. Hence, given the small sample of tornado events collected over SESA, all events are retained for the analyses conducted in Chapter 2.4. It is worth noting that ERA5 fields are strongly influenced by the model used to generate the reanalysis, especially in data-sparse regions away from sounding sites. Hence, we acknowledge that the representation of the tornadic environment may be strongly influenced by the physical parameterizations in the reanalysis model.

2.2.2.1Tornadic Parameters

An assortment of severe weather parameters that are normally used to study tornadic environments are analyzed in this research:

- **Mixed Layer Convective Available Potential Energy (MLCAPE, J/kg)**, the potential energy of the atmosphere to produce free convection and unforced air ascent. Unlike typical estimates of surface-based CAPE (where the air parcel initially holds the near-surface conditions), MLCAPE considers an air parcel starting with the mean conditions in the lowest 100 hPa. As a result, it accounts better for the atmospheric conditions in the boundary layer. MLCAPE has been widely used to explore tornadic environments (Brooks et al. 2003; Brooks 2009; Grams et al. 2012; Thompson et al. 2012; Anderson-Frey et al. 2016; Taszarek et al. 2020). High MLCAPE (>1000 J/kg) is often required to trigger deep convective clouds, though low CAPE environments (<500 J/kg) can also support severe thunderstorms (Guyer and Dean 2010; Davis and Parker 2014; Sherburn and Parker 2014).
- **Mixed Layer Convective INhibition (MLCIN, J/kg)**, the amount of energy that an air parcel needs to overcome while negatively buoyant in order to reach the level of free convection. Moderate CIN can allow convection to be severe instead of widespread and

short-lived by allowing convective instability to build over time. However, if CIN is too strong, convection may not occur if a suitable lifting mechanism cannot overcome the negative buoyancy.

- **Mean-Layer Lifting Condensation Level (MLLCL, m**), the height level at which an ascending parcel becomes saturated, based on a surface temperature and dew point calculated from the mean profile in the lowest 100 hPa. High relative humidity at low levels causes rising air parcels to reach saturation at lower elevations. Evidence shows that the mean-layer technique is more suitable for studies of convective processes in the atmosphere instead of that using a surface-based parcel (e.g., Craven et al. 2002). Tornadogenesis is more likely when no strong cold pools develop that suppress the updraft, and hence a low cloud base height is present. Evaporative cooling that induces cold pools is controlled by the moisture content (i.e., relative humidity) at low-levels, meaning that a humid layer will prevent raindrops from evaporating, thus enabling updrafts to grow.
- **Bulk vertical wind SHear (BSH, m/s)**, the surface to above ground level change in wind, calculated over the lowest 1-km (BSH01) and 6-km (BSH06) layer above ground level. We use the wind difference between the respective layer limits. Deep-layer shear is important to the organization and longevity of storms (e.g., supercells or MCSs), while high low-level shear environments tend to favor tornadic storms by enhancing the updraft and vertical vorticity at low levels (Coffer and Parker 2015).
- **Storm Relative Helicity (SRH, m^2/s^2)**, the potential for a cyclonic updraft in a storm (i.e., potential for supercellular, rotating storms), is calculated over the 0-1 km (SRH01) and 0-3 km (SRH03) layers above ground level. To estimate the storm-relative winds, we use the Bunkers storm motion vector in the Southern Hemisphere, i.e., left-moving supercell

(Bunkers et al. 2014), thus making SRH normally negative. Low-level SRH is particularly helpful to assess tornadogenesis potential of a storm (Coffer et al., 2019).

- **Significant Tornado Parameter (STP)**, a parameter composed of multiple variables relevant to tornadogenesis, is calculated by combining the values from multiple convective parameters to obtain a single value. The effective inflow layer is considered for SRH and BSH computations (ESRH and EBSH), and the lowest 100 mb mixed-layer for CAPE, CIN, and LCL (MLCAPE, MLCIN, and MLLCL) (see Thompson et al. (2004) for further details in its computation). STP values are greater (lower) or equal to zero in the Northern (Southern) Hemisphere, based on positive (negative) SRH input. STP greater than 1 in magnitude appears to indicate higher chances for significant tornadic supercells in lieu of nontornadic supercells (Thompson et al. 2003).

The following convective parameters were computed using the *SharpPy* Python library (Blumberg et al. 2017): MLCAPE, MLCIN, MLLCL, BSH, SRH, and STP.

2.2.3 International Satellite Cloud Climatology Project (ISCCP)

Given the lack of observational data in the region and to provide insights about the storm size accompanying every tornadic event, cloud top temperatures for clouds detected by IR threshold brightness temperatures (Tc) from the HGG (H-series Gridded Global) ISCCP - Basic H-Series product were used (Young et al. 2018). The ISCCP product has a 1ºx1º equal angle horizontal spacing and 3h temporal resolution and extends from July 1983 through June 2017. In order to estimate the cloud shield size for every event to discriminate between small isolated and large convective systems, a threshold of Tc = –48ºC is used. The convective feature that is closest to the tornadic event in time and space is taken into account by adding all the pixels having

Tc<−48ºC that are connected. If the tornado is not collocated with the convective feature, we consider the closest feature associated to the tornado. In this way, a broad perspective on whether tornadoes in subtropical South America are produced by isolated supercells or are embedded into larger and organized MCSs is possible. Note that modest inaccuracies in the estimation of the cloud shields sizes caused by different satellite view zenith angles are possible (Knapp et al. 2021). Given the period of this data (ending in July 2017), only 66 events are considered for the comparison with satellite fields, with an additional 4 of them subsequently removed due to inconsistencies between the convective feature shown by the satellite product and the approximate location and time of the tornado. Among the potential reasons for the mismatch are errors in the tornado location, errors in tornado time of occurrence, very short-lived convective cells not captured by the 3-hourly data, or unknown errors in the ISCCP dataset caused by steep satellite view zenith angles.

2.2.4 NOAA Outgoing Longwave Radiation (OLR) and Madden-Julian Oscillation (MJO)

To give an idea of potential sources of teleconnections originating from the tropics that modulate the large-scale conditions affecting tornado-producing storms in SESA, the daily NOAA OLR product (Liebmann and Smith 1996) is used. This product is on a regular 1ºx1º grid and is available from 1974 to 2021. To further explore the contribution of tropical sub-seasonal variability to SESA tornado activity, an analysis of the MJO and its relationship with the tornadic environment is performed using the Real-time Multivariate MJO Index (RMM) (Wheeler and Hendon 2004). We assess the phase of the MJO 1-2 weeks in advance of every tornadic event for any active MJO day (RMM amplitude higher than 1) to determine if preferred MJO phases are associated with tornadogenesis.

2.3 Tornadic Storm Characteristics

2.3.1 Tornado Storm Report Database

The location of every tornado storm report identified in Argentina, Uruguay, and southern Brazil in this study is illustrated in Figure 2.1. According to the map, most of the reports are concentrated between 30ºS and 40ºS, in the area with the lowest elevations in the region to the east of the Andes mountains. However, there are many reports tied to small topographic features such as east of the SDC (e.g., in Córdoba). Although very uncommon, a couple of tornadic events also occurred in the Andes foothills in Northwestern Argentina. Some areas have a higher concentration of events (e.g., Buenos Aires and Córdoba metropolitan areas), likely because of the denser population over these locations compared to other parts of SESA that enhances the chances of experiencing and reporting a tornadic event (e.g., Anderson et al. 2007; Ray et al. 2003). Information about tornado intensity - when available - is also included on the map. About 60% of the cases do have some report about intensity in the F-scale (Fujita 1971), but only 40% of them (18 events) have been confirmed (i.e., intensity has been verified), either by peer review studies (e.g., Pita and Schwarzkopf 2016), independent investigations conducted by meteorologists or scientists (e.g., http://tornadoseneluruguay.blogspot.com/), or official reports issued by the weather service or related organizations. The F-scale ratings collected here may not follow same quality standards of, for instance, the U.S. National Weather Service, though. The most frequent tornado intensities reported are F1 and F2, and a few confirmed F3 and F4 tornadoes are also included. For the remaining 40% of the events, reliable evidence to label them with any intensity category was not found. There is evidence of a few F5 tornadoes happening in SESA prior to 1990, but they are beyond the study period (Schwarzkopf 1988).

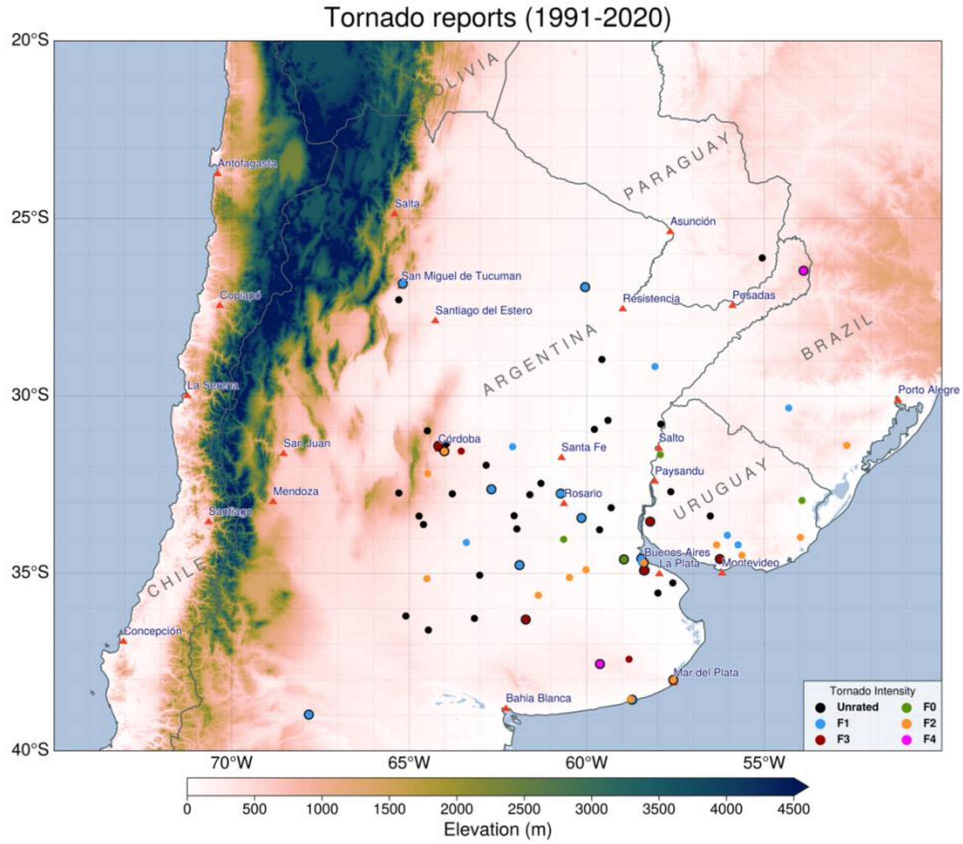

Figure 2.1. Selected tornado reports collected over subtropical South America (N=74). Color in dots represents estimated tornado intensity in the F-scale. Cases whose intensity was confirmed have a bold black edge. Terrain elevation (m) is shown in shading color. A red triangle indicates the location of selected cities.

The temporal distribution of tornadic storm reports (Fig. 2.2a) shows that the majority tend to happen during the extended warm season (October through April), with few reports during the cold season (May through September). December is the month with the highest frequency of reports, while tornadoes in June and July are the least frequent. February has the lowest number of reports within the extended warm season. The annual cycle distribution is generally like that in Schwarzkopf (1988), although they found January to have the highest number of tornado reports. This distribution shows that tornadoes in SESA occur not only in spring and summer, but also during fall, which reinforces the findings from Zipser et al. (2006) who showed frequent intense thunderstorms happening in SESA in almost all the seasons.

Analysis of the diurnal cycle of tornadic events from Figure 2.1 reveals a bimodal distribution (Fig. 2.2b). Most of the events occur during the local afternoon hours, peaking around 16-17 LT, and decreasing in frequency through the early night. A secondary and lower peak in frequency occurs between late night and early morning. The morning hours (8 LT through 12 LT) showed the fewest number of reports. This distribution may not necessarily represent the actual diurnal cycle of tornado frequency in SESA. The database used does not include many reported tornadoes in southern Brazil, where nocturnal tornadoes might be more frequent. Besides, a bias toward more reports during daytime is expected due to reduced visibility and fewer people witnessing events during the night in a region with weak radar coverage (Trapp et al. 2006).

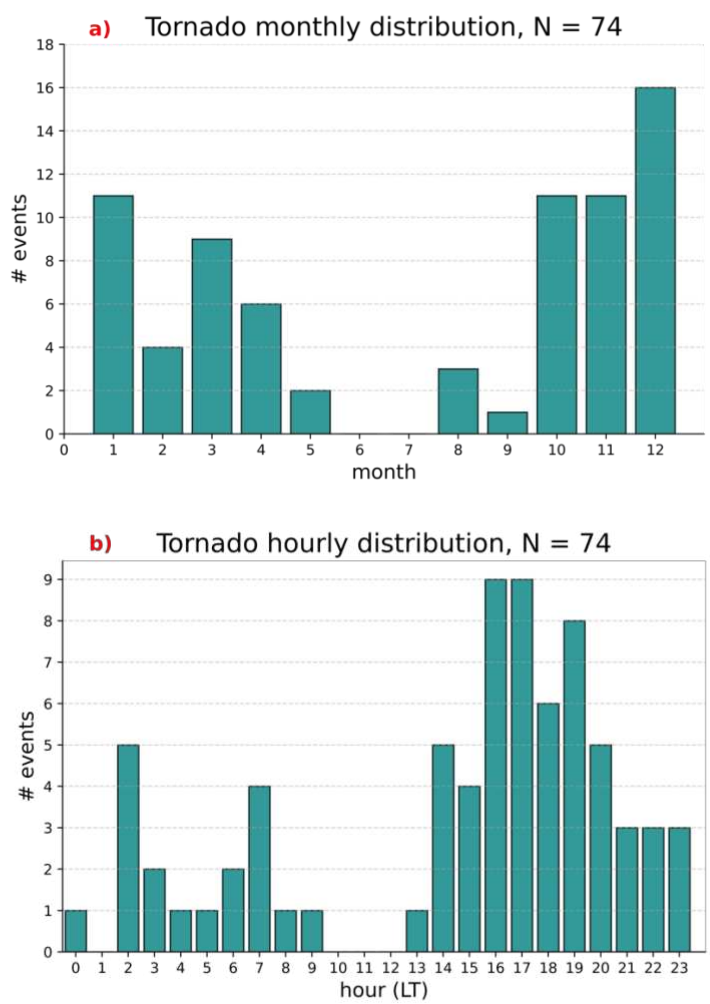

Figure 2.2. Distribution of the 74 tornadoes collected between 1991 and 2020 for the present study by (top) month of the year and (bottom) hour of the day (local time).

2.3.2 Storm Size Distribution

Figure 2.3 shows the size distribution of the cloud shields associated with the storms producing the tornadoes (please refer to Chapter 2.2.3 for details in the storm size estimation). 49 storms had a cloud shield that was ≥ 1 pixel (~10,000 km^2), while 13 of the remaining cases did not meet the criteria, either because the storm was deep but smaller than the 10,000 km^2 needed to be captured on a 1º-by-1º gridbox, or the cloud top was not cold enough, which can be the case for low-topped supercells (Kennedy et al. 1993). To get insights into the estimated size and strength of cells for these 13 cases, the high resolution (0.1º grid spacing) ISCCP H-series pixel-level global product (HXG) (Young et al. 2018) was examined, including a visual inspection of satellite imagery from the Global ISCCP B1 Browse System (GIBBS) (accessible here: https://www.ncdc.noaa.gov/gibbs/). For the remaining 4 cases it was not possible to connect the location of the tornado to a cloud shield, likely because of the lack of a convective feature close enough to the tornado, as determined using the multiple approaches mentioned above (not shown). The lack of higher temporal resolution data may also cause a mismatch between the tornado location and the convective feature. Tornadoes mismatched by more than one hour from the satellite data may miss the evolution and location of fast-evolving storms. For events that occurred in between two snapshots (e.g., tornado reported at 1:30 pm and the closest imagery occurring at 12 pm and 3 pm), we assigned the average storm size from the convective feature located over the tornado as the average of both times. Therefore, the ultimate analysis performed in this section is based on 62 tornadic storms from January 1991 to June 2017.

The distribution of storm sizes presented in Figure 2.3 shows a large spread in the cloud shield size, where storms can be less than 50,000 km^2 or be as big as 1,300,000 km^2, though most of them concentrate below 650,000 km^2. Given that MCSs are considered to have scales of hundreds of kilometers in diameter (Houze 2004; Schumacher and Rasmussen 2020), at least 30 tornadoes appear to be embedded into MCS-like storms (>150,000 km^2). Yet, this does not necessarily mean that tornadoes are being produced mostly by MCSs (e.g., squall lines); tornado-producing supercells may be located close to large convective systems showing large cloud shield signals that potentially disguise independent isolated cells. On the other hand, around 13 events with sizes below the data resolution (and thus cannot be shown in Figure 2.3) may be supercell tornadoes or landspouts given their characteristic smaller sizes. Additionally, a comparison of the time of occurrence of tornadoes and the corresponding cloud shield size shows that nocturnal tornadoes are associated with 20% larger cloud shields than daytime events. This may be due to convective systems that initiate in the afternoon and grow upscale through the night, a process frequently observed in this region (Mulholland et al. 2018, 2019; Piersante et al. 2021; Rasmussen and Houze 2011, 2016; Rasmussen et al. 2014, 2016). A general outcome from Figure 2.3 and the additional 13 cases examined is that tornadic storms more frequently develop from isolated thunderstorms or small MCSs rather than large convective systems, which broadly agrees with the predominance of discrete and embedded supercell tornadic storms over other storm modes observed in the U.S. Great Plains (Smith et al. 2012).

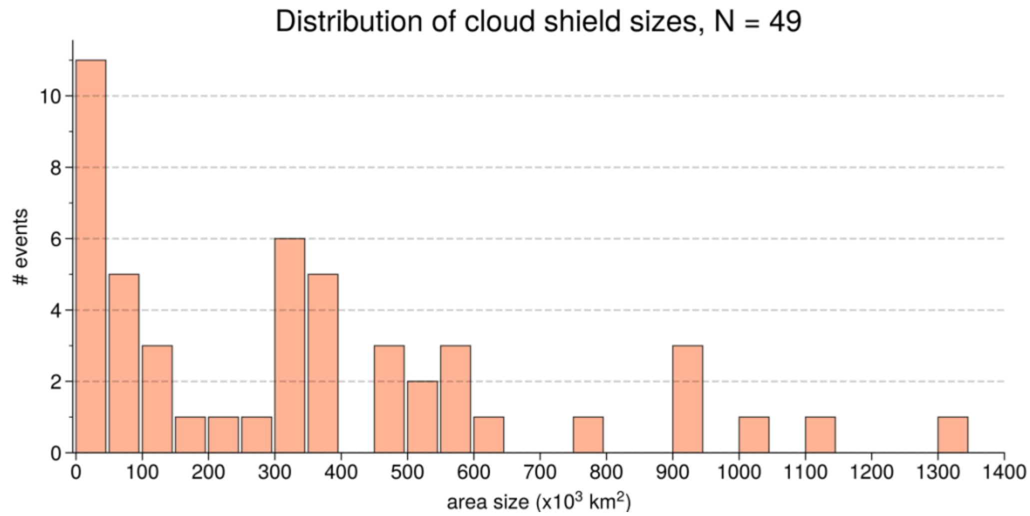

Figure 2.3. Histogram of estimated cloud shield size from 49 tornadic storms using an ISCCP cloud top temperature threshold of -48ºC. Cases whose size is estimated to be small enough to be captured by the ISCCP gridded data are not included here. See text for details.

2.4 Mesoscale Environments Supporting Tornadic Storms

2.4.1 Mesoscale proximity environments

ERA5 reanalysis is used to analyze the mesoscale ingredients that support tornadic storms in SESA. Figure 2.4a presents the distribution of the MLCAPE and BSH06 environment at the closest times and grid point locations to the tornado events. From research on U.S. convective storms, it is well known that large CAPE and deep-layer shear values are favorable for producing severe weather, including tornadoes (Rasmussen and Blanchard 1998; Brooks et al. 2003; Grams et al. 2012; Thompson et al. 2012) and organized convective storm modes (Jorgensen and Weckwerth 2003). In our tornado event database, there is a concentration of events showing moderate to high MLCAPE and high BSH06 values; the median of the distribution is located at 929 J/kg for MLCAPE and 24 m/s for BSH06. Around 2/3 of the cases present high wind shear values (>20 m/s) and ~38% a highly unstable environment (MLCAPE >1250 J/kg). Only 3% of the tornadic storms are positioned in the low-shear, low-CAPE quadrant (<10 m/s and <500 J/kg, respectively). When compared to the typical U.S. tornado environment, the CAPE vs. BSH06 scatterplot in Figure 2.4a broadly agrees with that shown by Brooks et al. (2003) and Anderson-Frey et al. (2016) for tornado events over the U.S. in terms of the maximum density location. Additionally, some events presenting MLCAPE < 10 J/kg (~12% of all cases) can be observed; potential caveats in the reanalysis product (errors in representing boundary layer structure due to limited observations in SESA and insufficient spatial resolution and/or time stepping) could explain these numbers. Indeed, most of these events had moderate to large MLCAPE values a few gridpoints/hours displaced from the tornado event (not shown). High-shear, high-CAPE environments are more likely to support large and organized MCSs in U.S. storms (Jorgensen and Weckwerth 2003). Storms with cloud shield sizes of 400,000 km^2 or more (i.e., very large MCSs) are also mostly concentrated in the high-shear, high-CAPE environment (Fig. 2.4a) in our analysis.

Although CAPE and BSH06 are relevant for severe weather production, boundary layer relative humidity (i.e., cloud base height), and low-level wind shear have been shown to be among the two most important factors in discriminating between non-tornadic and tornadic storms (Thompson et al. 2012; Markowski et al. 2003; Brooks and Craven 2002). Figure 2.4b shows the MLLCL versus BSH01 environment from the 74 tornadic events over SESA. For tornadoes having large BSH01 values, MLLCL is small, and vice versa. For instance, when BSH01 > 15m/s, MLLCL is below 950 m, and when MLLCL > 1300m, BSH01 values exceed 6.5 m/s in 1 out of 10 events. The median values for MLLCL and BSH01 for the 74 events are 778 m and 8.1 m/s, respectively. MLLCL is on the order of that observed for significant tornadic storms in the U.S., although BSH01 is moderate to weak as it is within the lowest 25% of the BSH01 distribution for U.S. tornadoes (Thompson et al. 2003; Thompson et al. 2012). The MLLCL vs. BSH01 environment in Fig. 2.4b more closely resembles the significant severe scatterplot shown in Brooks et al. (2003) than the significant tornado scatterplot, with the latter presenting higher BSH01 values overall. Additionally, Figure 2.4b shows the longitudinal location and storm size in relation to the MLLCL vs. BSH01 environment under which the tornado events occur. Although the behavior is complex, there is a suggestion that strong low-level shear is more likely when events occur far from the Andes and the storms are relatively large, while a weak shear environment is more frequent for events near the Andes and the SDC with smaller cloud shield sizes. One hypothesis for this behavior is that the extreme Andes elevation and very steep sloping cause low-level winds to be weak while the frequent strong synoptic forcing explains the strong mid-level shear seen in observations from RELAMPAGO (Sasaki et al. 2022; Piersante et al. 2021). In terrain-modification modeling WRF experiments that varied the height of the Andes, Rasmussen and Houze (2016) showed that when reducing the Andes by 50%, the strength of the SALLJ reduced almost in half and also was shallower in vertical extent. Sasaki et al. (2022) showed that the SALLJ jet height was higher for strongly-forced synoptic environments compared to the lower SALLJ heights for weakly-forced synoptic environments. According to Fig. 2.4b, this influence in the low-levels seems to diminish farther away from the Andes in eastern subtropical South America. On the other hand, frequent upscale growth over SESA (Rasmussen and Houze 2011; Rasmussen et al. 2016; Mulholland et al. 2018) may explain the tendency to get broader cloud shield tendency farther east. Future research with better observations of tornadic storm environments could investigate the variability in SALLJ depth and strength and its influence on the generation of low-level shear necessary for tornadogenesis, as well as the spatial variability on tornado storm mode, and the role of the Andes in these dynamic processes over SESA.

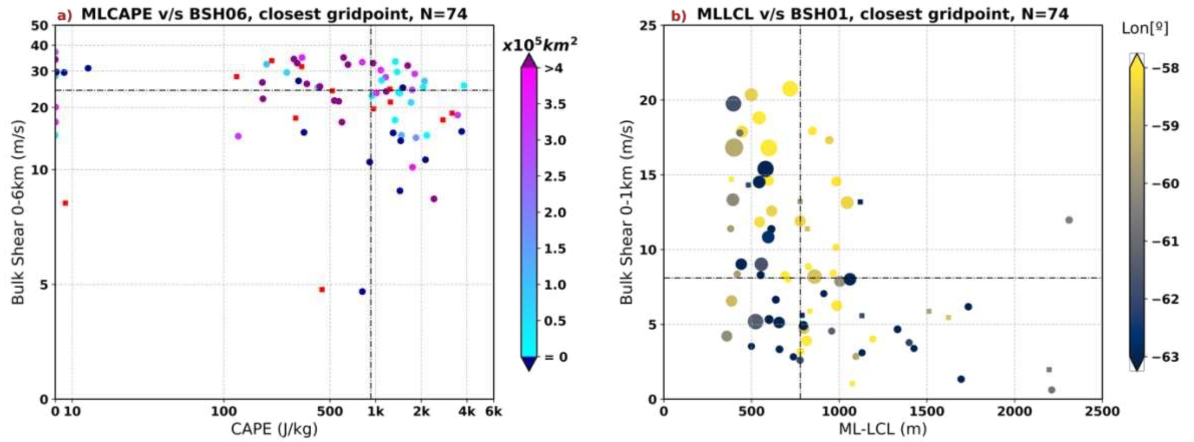

Figure 2.4. Scatterplot for the 74 tornadoes, using the closest gridpoint at the closest time to the respective event. (left) MLCAPE vs BSH06, colorbar indicates the size of the cloud shield (size below 1px in dark blue and over 40px in dark magenta). (right) MLLCL vs BSH01, colorbar indicates the location of the event in longitude and the marker size represents the size of the cloud shield. Red (colored) squares in panel a (b) indicate events happening after June 2017, when ISCCP data to estimate storm sizes were not available. Dashed lines show the median value for the corresponding parameter.

To explore the characteristic vertical profile of winds for tornadic storms in SESA, a composite hodograph based on the vertical wind profile from the closest grid point to every tornado is computed (Fig. 2.5). Counterclockwise rotation (backing in the Southern Hemisphere) is clear in most of the individual profiles and in the composite, especially at low levels, where NNE winds near the surface turn mostly westerly after reaching 2 km. This curved hodograph is broadly consistent with the veering structure for tornadic storms in the U.S. Great Plains, although the intensity and rotation are weaker at low-levels in the SESA composite (the trajectory is already westerly by 1 km for U.S. tornadoes) (Maddox 1976; Markowski et al. 2003; Coffer and Parker 2015), which might be related to the taller Andes blocking westerly winds at higher levels. As a matter of fact, the core of the SALLJ has been observed at higher levels than its counterpart in the U.S. (Montini et al. 2019; Piersante et al. 2021; Sasaki et al. 2022). The hodograph is also consistent with the wind profile found by Rasmussen and Houze (2011) for storms having radar echoes with wide convective cores in SESA, which supports the supercellular or early-maturing

MCS storm structure prevalent in Figure 2.3. The speed change with height agrees with the median values shown previously in Figure 2.4. In the 3-6 km layer, a small veering in winds occurs that is likely not significant due to the low sample size, but consistent with hodograph composites for U.S. tornadic storms (Maddox 1976; Markowski et al. 2003). The spread of the individual hodographs is small near the surface as winds are weak, while near the tropopause the spread is large due to different pathways taken along the 12-km layer. Tropopause winds tend to favor the WSW direction, however.

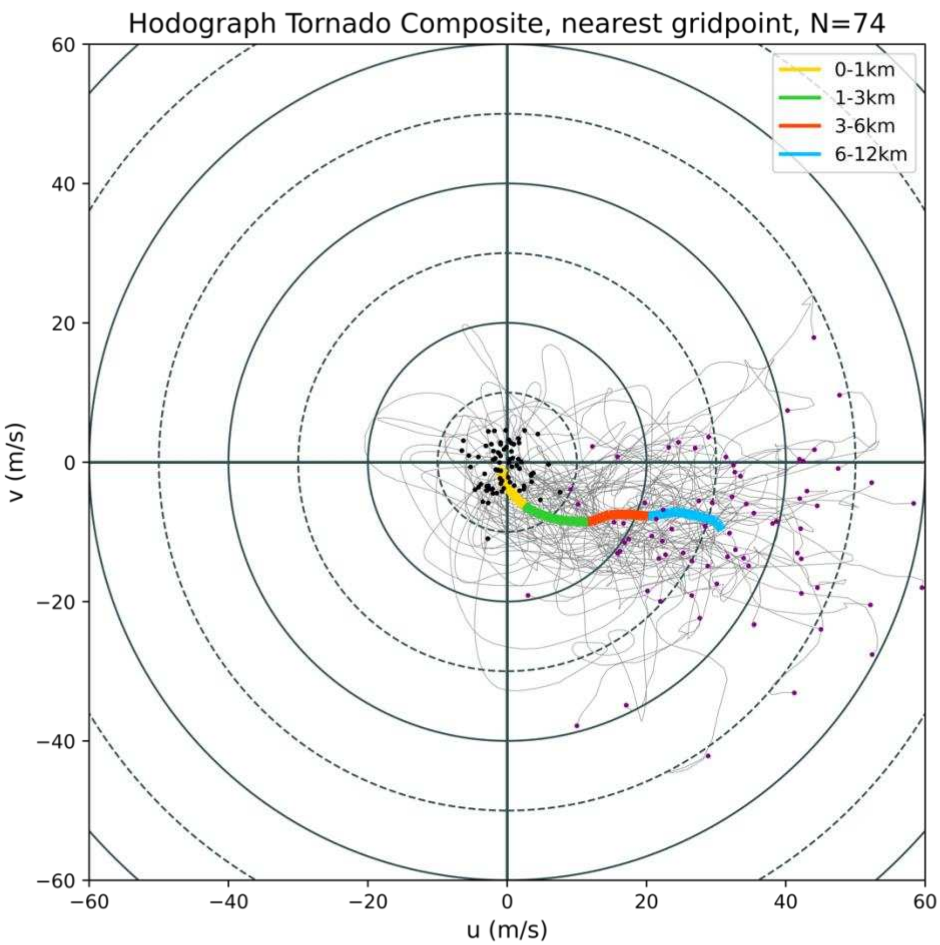

Figure 2.5. Hodograph representing the 74 tornadoes (gray lines) and the mean circulation (thick colored line). Black (magenta) dots indicate the starting (ending) point of every hodograph at 10 m (12 km). Color-segmented lines indicate different layers. The closest grid point at the closest time to every event was used to get the wind profiles.

Analysis of the composite time evolution of different tornadic parameters before and after the reported SESA tornado is presented in Figure 2.6. These results will be contrasted with climatological studies done in the U.S. for tornadoes from different storm modes by Thompson et al. (2012) (hereafter T12) using the RUC (Rapid Update Cycle, currently Rapid Refresh, RAP) model and analysis system, and tornadoes with various intensities (F-scale) by Taszarek et al. (2020) (hereafter T20) using the ERA5 reanalysis. As expected, an unstable atmosphere is important for tornadic storm evolution (Fig. 2.6a), with MLCAPE starting to increase 24 hours before the tornado is observed, followed by a steeper increase during the immediately preceding 10 hours. Maximum average MLCAPE around 1250 J/kg is reached 2 hours before the tornado (median MLCAPE ~1140 J/kg at that time), followed by a sharp decrease, which reflects the importance of this parameter in building a robust storm that can spawn a tornado. The median MLCAPE during tornado occurrence (929 J/kg) is slightly weaker than MLCAPE values found in T12 for MCS or hybrid tornadoes but consistent with F0-F3 tornadoes in T20. Average MLCIN evolution (Fig. 2.6b) is somewhat noisy. High values (~−110 J/kg) 24 to 14 hours before the tornado, followed by stronger inhibition (~−125 J/kg) 12 to 6 hours before tornadogenesis, are consistent with what is normally seen prior to severe weather phenomena (Emanuel 1994). From −6h to −1h, MLCIN decreases by ~55 J/kg, reaching a minimum of ~−70 J/kg on average at −1h. The MLCIN observed at 0h (median of ~-65 J/kg) is slightly larger in magnitude than the values observed for tornadoes in the U.S. (T12; T20), suggesting a stronger resistance to widespread convection over SESA during tornadogenesis. Rasmussen and Houze (2016) showed that CIN is usually stronger in subtropical South America in comparison to the U.S. Great Plains due to a topographic enhancement caused by the higher elevation of the Andes, thus impacting the storm mode characteristics.

The low-level environment near the storm presents an interesting evolution. Both BSH01 and SRH01 increase in magnitude 24 to 12 hours before the tornado, and then stay relatively steady (about 8 to 8.5 m/s and −105 to −100 m^2/s^2) up to the tornado time. No clear peak was observed for these variables. BSH01 in SESA at hour 0 (median of ~8 m/s) is significantly weaker than in the U.S. low-level environment, where it is ~15-20 m/s for F2+ tornadoes, depending on the storm mode (T12; T20), but it approaches 10 m/s for F0 events. Similar differences are observed when contrasting SRH01 (median of ~−80 m^2/s^2), at best reaching non-tornadic severe storms median values observed in the U.S. (T12). The mid- to deep-layer environment behaves differently. BSH06 shows a nearly linear increase from more than 12 hours before the tornado (~19 m/s) through 6 hours after (~25 m/s). SRH03 increases in magnitude at a constant rate that becomes steeper after −6h, reaching a minimum of about −210 m^2/s^2 at −2h, followed by a rapid decrease in magnitude until it stabilizes at about −90 m^2/s^2 past +12h. In comparison, both BSH06 and SRH03 are as strong as for U.S. tornado environments (median ~25 m/s and >180 m^2/s^2 at 0h in T12; T20). It is important to highlight the connection between the SRH03 maximum and tornado occurrence (Rasmussen and Blanchard 1998; T12; T20), as the quick increase in this parameter might reflect storms becoming tornadic when moving over a local high SRH region (Markowski et al. 1998).

Two additional shear layers (0-2 km and 0-3 km), not commonly used to forecast severe storms, were also explored due to past research showing that the SALLJ is deeper than similar low-level jets in the U.S. (Sasaki et al. 2022; Rasmussen and Houze 2016) and the fact that the 0-3 km shear could have some forecast potential for MCS tornadoes in the U.S. (e.g., Gibbs 2021). Unlike BSH01 and BSH06, these shear parameters show overall larger values that are consistent with the layer size increase, and (interestingly) peak at 0h. More analyses are needed to explore the role of 0-2 and 0-3 km shear layers in tornadogenesis over SESA, which is a subject for future research.

Evidence suggests that a low cloud base height (estimated by the MLLCL) is important for tornadic storm environments (Brooks et al. 2003; Markowski and Richardson 2009; Thompson et al. 2012). The time evolution of the MLLCL is very similar to BSH01, with a decrease in height between −24h and −12h, steady behavior at ~1100 m for 6-8 hours, and then an absolute minimum is reached (~750 m) 4 hours after the tornado. The MLLCL is about 863 m at the time of the event (median of 785 m), broadly consistent with values observed for U.S. tornado environments (T12; T20).

Finally, the STP is a composite parameter created to support operational forecasts by discriminating tornadic/non-tornadic environments (Thompson et al. 2003). In our analysis, the STP demonstrates a linear increase in magnitude from about −11 until −2 hours with a maximum of about −1, and then a sharp decrease (mean and median of –0.65 and –0.15 at 0h, respectively). Of the parameters used to calculate STP, its evolution resembles that of CAPE the most. STP values below 1 in magnitude are in general not supportive of supercell tornado environments in the U.S. (e.g., Thompson et al. 2003; Grams et al. 2012; T20), so it may not be as useful for operational forecast of significant tornadoes in SESA given the values at the time of occurrence. However, this threshold can vary depending on the environment (e.g., Sherburn and Parker 2014; Anderson-Frey et al. 2017) and here we are compositing quite a range of environments. Moreover, the presumably small fraction of tornado reports with intensity F2+ used here, along with the inclusion of non-supercell tornadoes in the composites might also explain the reduced composite STP values at the time of occurrence. Indeed, median estimations of STP for U.S. tornadic environments using ERA5 at the time of occurrence (T20) are of ~0.4 for F2-F3 tornadoes (~1.0

for F4-F5), which is well above the 0.15 obtained for SESA. Regardless, STP peaking prior to tornado occurrence reflects that the tornadic environment in SESA is showing enhancement in some of the same key ingredients for tornadogenesis as for the U.S., but the typical threshold values may need to be carefully reviewed in operational forecasting applications.

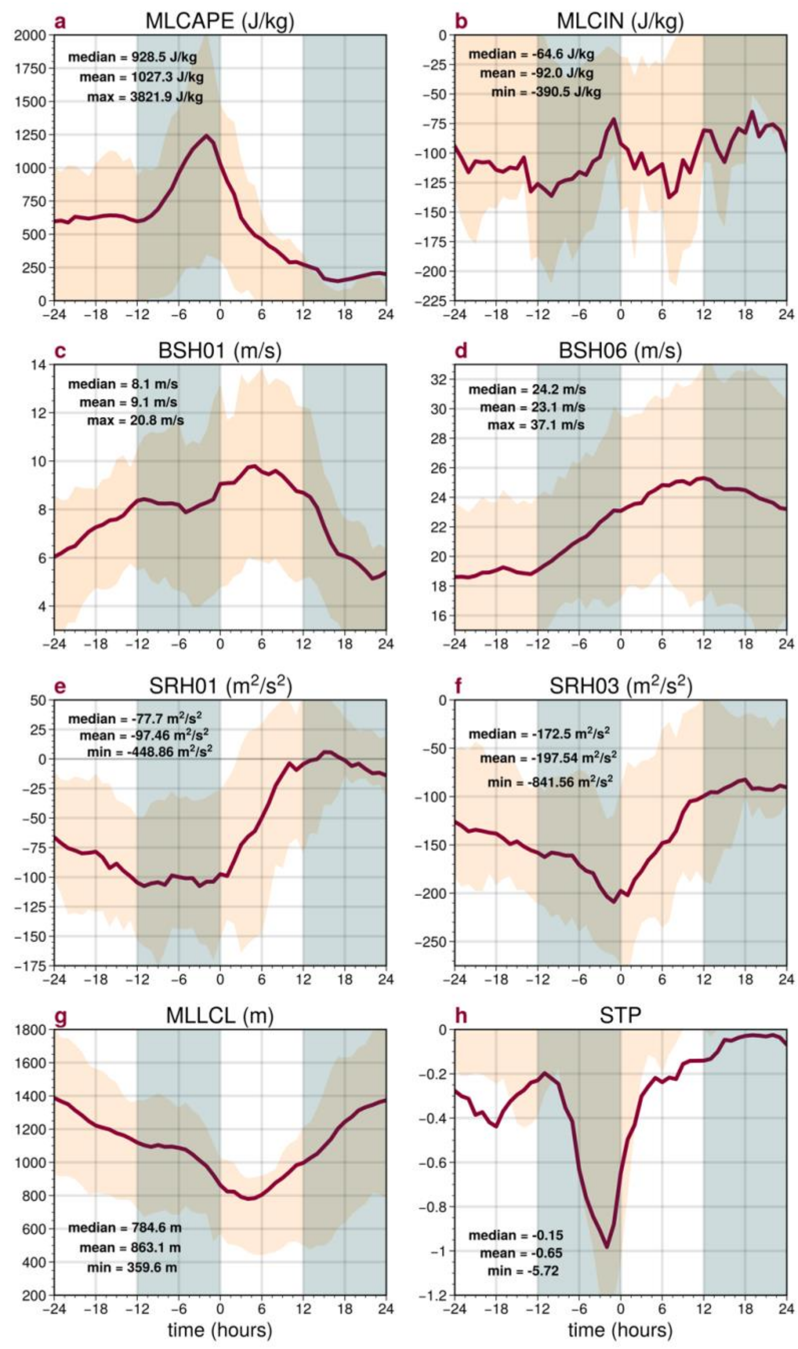

Figure 2.6. Composite evolution of several convective parameters through a 48h period centered at the time of occurrence of each event, obtained by selecting the closest proximity sounding (i.e.,

closest grid point) to every tornado. Light red shading indicates the spread of the interquartile range, while dark red line shows the mean evolution. Summary statistics at hour 0 are included as text for every parameter. Vertical shading highlights 6h spans.

2.4.2 Mesoscale regional environment

To provide greater context to the storm evolution results, fixed-domain spatial evolution composite maps are generated. These maps give important information related to the geographic and topographic features of the region (i.e., the Andes and Sierras de Córdoba mountains, and the Atlantic Ocean) and how they may influence the tornadic environments in SESA. Figure 2.7 shows the composite spatial evolution of SRH01 from −12 to +12 hours with respect to the tornadic events. Enhanced negative helicity that develops along the Pampas at −12h evolves into a maximum in SRH01, settling over southern Uruguay at 0h and remaining relatively stationary for the next 6 hours. Interestingly, the negative SRH01 peak (110-125 m^2/s^2) is not located over the area with the highest concentration of tornado reports. On the other hand, a positive helicity region located to the south of the SDC emerges and grows in size and magnitude up to 75-90 m^2/s^2 after 0h. Consistently, almost no tornadoes were reported over that area, although anticyclonic tornadoes under positive SRH are likely near complex terrain (e.g., Carbajal et al. 2019). Prior to tornado occurrence, the BSH01 field shows near-zero values collocated with the positive SRH01 area. The most plausible explanation for this phenomenon is simply that the signature reflects cold front passage. This idea is reinforced by what tornado-relative composite maps of SRH01 and BSH01 show: a similar SW-NE oriented dipole structure that is more evident during and after tornado occurrence as well (not shown). Another idea to explain this positive SRH01 might be the presence of the SDC, which acts as a barrier that distorts the northerly flux coming to the mountains. During and after tornado occurrences, southerly shear is located south of the SDC, thereby reinforcing the positive SRH01 anomaly. This southerly flow might be related to the returning flow from the mid-level anomalous trough passage and subsequent lee cyclogenesis (Fig. 2.10), as shown by other studies (Rasmussen and Houze 2016; Piersante et al. 2021). The Andes may also play a role; their elevation and steepness may make zonal winds weak in the first 2 km, as evidenced by the composite hodograph (Fig. 2.5). Further analyses are needed to investigate these hypotheses that are beyond the scope of the current study.

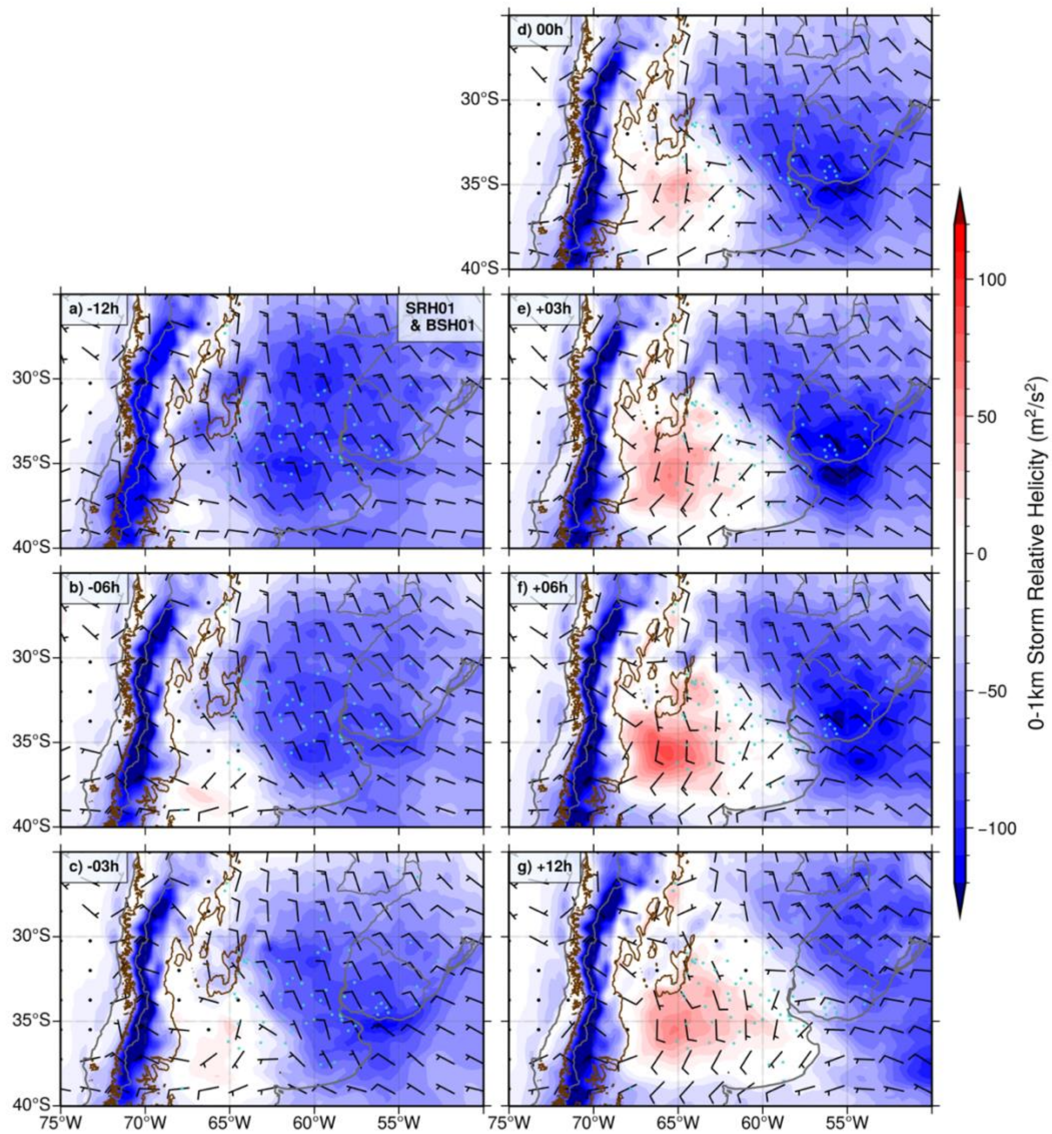

Figure 2.7. Composite fields of 0-1 km storm-relative helicity (shaded) and 0-1 km bulk wind difference (wind barbs) at a) −12h, b) −6h, c) −3h, d) 0h, e) +3h, f) +6h, and g) +12h with respect to the tornado occurrence in SESA. Short barbs indicate 2.5 m/s while long barbs indicate 5 m/s. 800-m AGL elevation is indicated with brown contours to help the reader better visualize the main topographic features. Turquoise dots show the location of the tornadoes used in this study.

Figure 2.8 shows the composite spatial evolution of STP. This parameter increases in magnitude starting at −12h, reaches its maximum extent a few hours before and at the time of tornado occurrence, and then diminishes by +12 hours. The position of the maximum STP (shading below −0.4) matches well with the region where most of the tornadoes occur. The maximum magnitude of composite STP from Figure 2.8 approaches 1 (in apparent agreement with the Figure 2.6h magnitude maximum), but some individual cases can present higher STP (see the STP spread in Figure 2.6h). Indeed, there are instances where STP can reach values significantly lower than −1, especially east and southeast of the SDC (not shown). However, since our composites are derived from tornadoes occurring at distinct locations, reduced values are expected at any given spatial location.

To further explore the spatial signature of STP before and after tornadogenesis in SESA, tornado-relative composite maps of STP are computed. Figure 2.9 presents these maps for a ~22º latitude by ~15º longitude (89 by 61 gridpoints) domain, with the tornadic storm report locations at the center of the map. It is evident from the temporal evolution of STP that the maximum values are reached in the −3h to 0h timeframe, when STP is, on average, larger than 1 in magnitude and about 0.25º–0.75º north of the tornado location. In other words, this indicates that tornadoes are taking place just south-southwest of a peak in STP, which could further support the idea of storms becoming tornadic when entering a high STP region (which is also a high SRH region, not shown) (Markowski et al. 1998). More analysis is needed to elucidate this connection. The fact that high STP values are seen predominantly equatorward from where a tornado eventually occurs (and near-zero values poleward of it) gives an idea of the placement of the inflow of the storms. Figure 2.9 also shows composites of MLCAPE peaking equatorward of the tornado's position at −3h and

0h (>1500J/kg), but with the most unstable region located north of the STP maximum. At the tornado location, MLCAPE presents its largest spatial gradient. Parker (2014) used observational data to show that a peak in STP is also located just equatorward from supercell tornadoes observed in the U.S. and that this STP feature is significantly weaker and less organized when compared to non-tornadic supercells. Other studies addressing various tornado environments have also found STP peaking equatorward of tornadogenesis regions as a recurrent feature (Sherburn et al. 2016; Anderson-Frey et al. 2017). This finding could provide additional insight in anticipating areas for tornadogenesis over SESA.

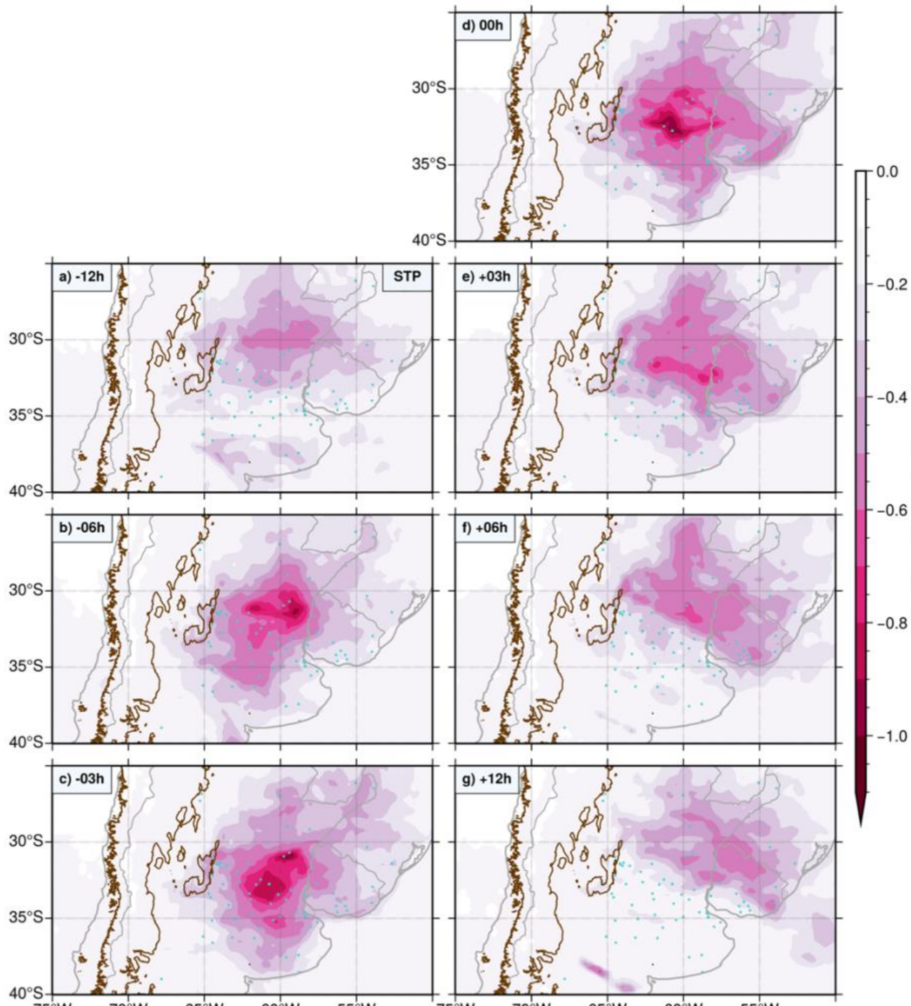

Figure 2.8. Composite fields of significant tornado parameter (shaded) at a) −12h, b) −6h, c) −3h, d) 0h, e) +3h, f) +6h, and g) +12h with respect to the tornado occurrence in SESA. 800-m AGL

elevation is indicated with brown contours to help the reader better visualize the main topographic features. Turquoise dots show the location of the tornadoes used in this study.

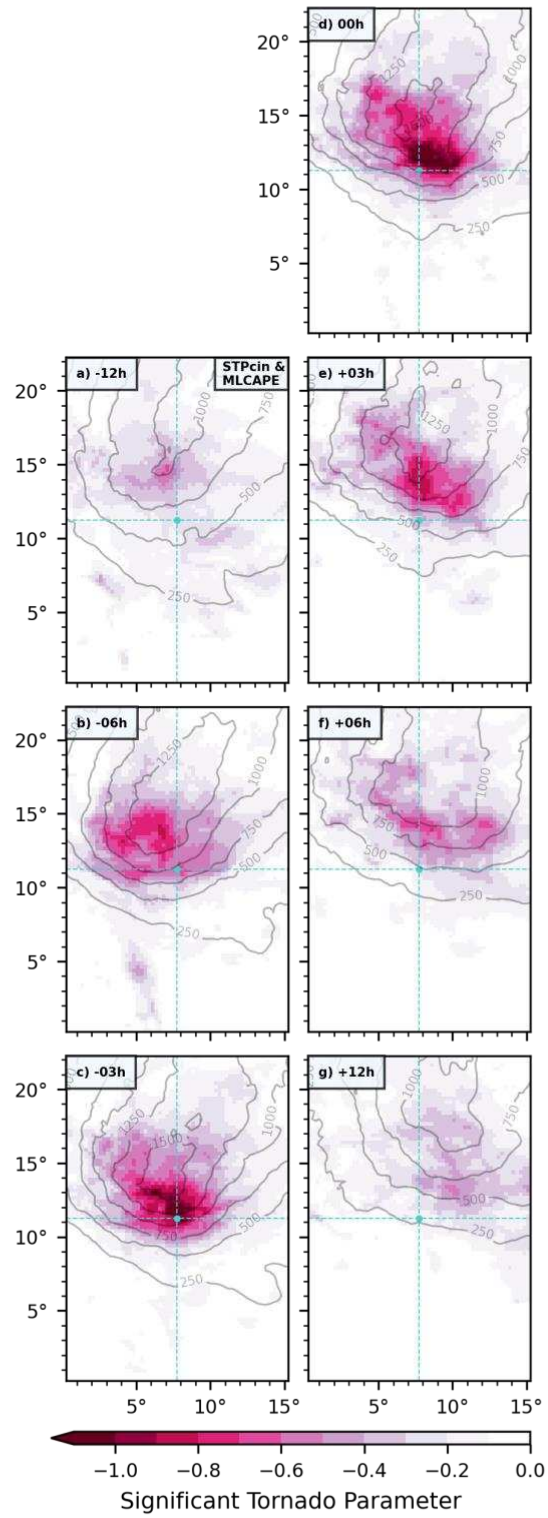

Figure 2.9. Tornado-relative composite maps of significant tornado parameter (shaded) and mixed-layer CAPE (gray contours, every 250 J/kg), at a) −12h, b) −6h, c) −3h, d) 0h, e) +3h, f)

+6h, and g) +12h with respect to the tornado occurrence in SESA. Maps correspond to a domain of 89 by 61 grid points (~22º latitude by ~15º longitude) centered at the location of the tornadic storms (cyan circle).

2.4.3 Tornadic storm comparison between SESA and the U.S. Great Plains

It is believed that tornadoes are more frequent in the U.S. Great Plains than in SESA plains, even though population density in countries like Argentina is relatively lower compared to the U.S. Despite their geographical similarities, it is important to note some differences that may shed light in frequency disparities. The Andes are taller and narrower than the Rockies in the subtropics, leading to enhanced CAPE and CIN in SESA that often require the additional lifting motion provided by secondary topographic features such as the SDC in Argentina (Rasmussen and Houze 2016). This can affect the initiation and evolution of deep and severe convection downstream, as has been evidenced by recent studies (Rasmussen and Houze 2016; Nesbitt et al. 2021; Rocque and Rasmussen 2022). In addition, the U.S. land extension, including the Great Plains and eastern U.S., is much larger than the Pampas region over Argentina, where the distance between the Andes and the Atlantic coast becomes shorter poleward (Fig. 2.1). This reduced land extension in southern Argentina can prevent the formation of an appropriate severe environment further south. Indeed, tornadoes are very frequent up to the northernmost state in the central U.S. (46-49ºN), while beyond 38-40ºS in Argentina these seem to be exceptional (e.g., Fig. 2.1; Schwarzkopf 1988).

Other reasons may be related to the convective environment. Recent results from Schumacher et al. (2021) depicted weak 0-1 km winds being relatively frequent during convective days in the RELAMPAGO field campaign that occurred in central Argentina, with a median of 4.9 m/s for BSH01 across all the soundings (R. Schumacher 2022, personal communication). These observations suggest that the typical 0-1 km wind shear is hardly supportive of tornadic storms in SESA in the RELAMPAGO study region. Actually, no tornadoes were officially measured or sighted during the campaign (though our own tornado database includes two events that happened during the RELAMPAGO deployment, but away from the operation sites). Results from Lopes (2020) who analyzed 40 tornado events in southern Brazil using the Climate Forecast System Reanalysis presented higher values for low-level dynamic parameters (median for BSH01~12 m/s, SRH01~−140 m^2/s^2) and surface-based CAPE (~1400 J/kg). This difference with our results may suggest spatial variability of the tornadic environment within SESA as our study considered only a few reports from southern Brazil. For example, isolating tornadoes closer to the mountains in Figure 2.4b mostly indicates BSH01 below 5 m/s, with only 7 out of 32 cases having values over 10 m/s, which is also consistent with the weak low-level shear environment in the RELAMPAGO domain (Schumacher et al. 2021). Therefore, having weak low-level winds might imply that tornadoes need to overcome a less favorable environment to be produced, which can occur less frequently. However, the stronger BSH01 environment observed east of La Plata Basin in Lopes (2020) might also be due to 30% of the tornadoes occurring in wintertime having a stronger low-level jet (Montini et al. 2019), related to more frequent synoptic forcing (Nascimento et al. 2016; Marengo et al. 2004). The weak low-level flow for SESA tornadoes could also be associated with weak tornadoes. Tornadoes generated in the U.S. have different BSH01 values when split into significant (F2+, ~16 m/s) and non-significant (F0-F1, ~10 m/s) tornadoes (T20). Our study did not have enough intensity information reported to connect these results to tornado intensity, however. Another factor that could explain differences observed in the low-level flow is the distinct moisture sources in North and South America and associated surface roughness. Li et al. (2023) conducted modeling experiments that replaced and smoothed the land equatorward of SESA with an ocean-like surface (similar to North America), which enhanced the low-level winds and, subsequently, the potential for tornadogenesis. Opposite results were observed for the U.S. when the Gulf of Mexico was replaced by forest-like land with increased surface roughness.

The apparently less favorable environment for tornadogenesis in SESA is also evidenced in the STP composites (Figs. 2.6h, 2.8), especially when contrasting median values at the time of occurrence. Given the geographical similarities with severe weather environments in the U.S., there is value in comparing the STP for SESA with similar calculations in the U.S. Indeed, tornado-relative spatial composites of STP (Fig. 2.9) illustrated similar equatorward placement of the peak in STP centered on tornadic storm report locations. Nevertheless, potential differences in the storm modes between both regions, observed a priori in Figure 2.3 and other studies (Rasmussen and Houze 2011, 2016; Rasmussen et al. 2014; Mulholland et al. 2018), may explain the difficulties in using STP for forecasting tornadoes in SESA, as this index was computed based on supercell tornado environments. Similarly, storm-relative helicity computations could also be affected by the tornado storm mode, as they rely on estimated storm motion from supercells (Bunkers et al. 2014). More comprehensive analyses would need to be done (including detailed field measurements) to determine if most tornadoes occur in MCSs as opposed to supercells.

2.5 Larger scale environments modulating tornadic storms

In this section, the synoptic and planetary-scale environments supporting the development of tornadic storms in SESA are examined to provide context to the mesoscale analyses presented in the previous section. Remote sources of predictability in the tropics will be also explored.

2.5.1 Synoptic scale

Figure 2.10 presents the composite 850 and 500 hPa geopotential height anomaly fields based on the 74 tornado reports collected over SESA, between two days before and two days after the events. Two days before a tornado, negative 500 hPa geopotential height anomalies related to a trough located south of 30ºS over the South Pacific impinge on the southern tip of South America (Fig. 2.10a). This trough then slowly moves to the northeast, placing its center over Patagonia while lee cyclogenesis emerges in central and northern Argentina by day 0 (Figs. 2.10b-c). This slow-moving system (~5-10 m/s, according to our estimations of mean displacement per day) may contribute to the abundance and severity of the storms as the persistence of the forcing maintains the unstable environment for a longer time, consistent with, for example, tornado outbreaks in the U.S. (e.g., Hamill et al. 2005; Mercer et al. 2012; Knupp et al. 2014). In fact, 15-20% of our tornado database considers events where two or more tornadoes occurred in the same day (Veloso-Aguila, 2023), but these repeat events were considered as only one day for the composite analyses. After day 0, the 500 hPa trough starts to move faster, crossing the Andes completely with its center located over the Atlantic south of 40ºS, while the intensity of the anomalies decays by 20 m. The evolution of cyclonic anomalies at the 850 hPa level is similar to that at 500 hPa during the previous 2 days, except that lee cyclogenesis occurs along the Andes foothills up to about 20ºS when tornadoes occur. The cyclogenesis in the lee of the Andes is maximized over the central Pampas and the northern Andes foothills in Argentina. In the period after the tornado (Figs. 2.10d-e), the negative 850 hPa anomalies start to diminish along the eastern edge of the Andes, while the low-pressure system at 850 hPa moves to the southeast at a faster rate than its counterpart at 500 hPa. The positive anomalies located over the Atlantic around 40ºS and to the east of the trough are likely also important to the generation of the severe weather environment. When coupled with the trough, the ridge may aid the generation of northerly flow anomalies, especially at low levels, which produces enhanced moisture transport associated with the SALLJ (Vera et al. 2006; Rasmussen et al. 2016; Sasaki et al. 2022) impinging upon the tornado region.

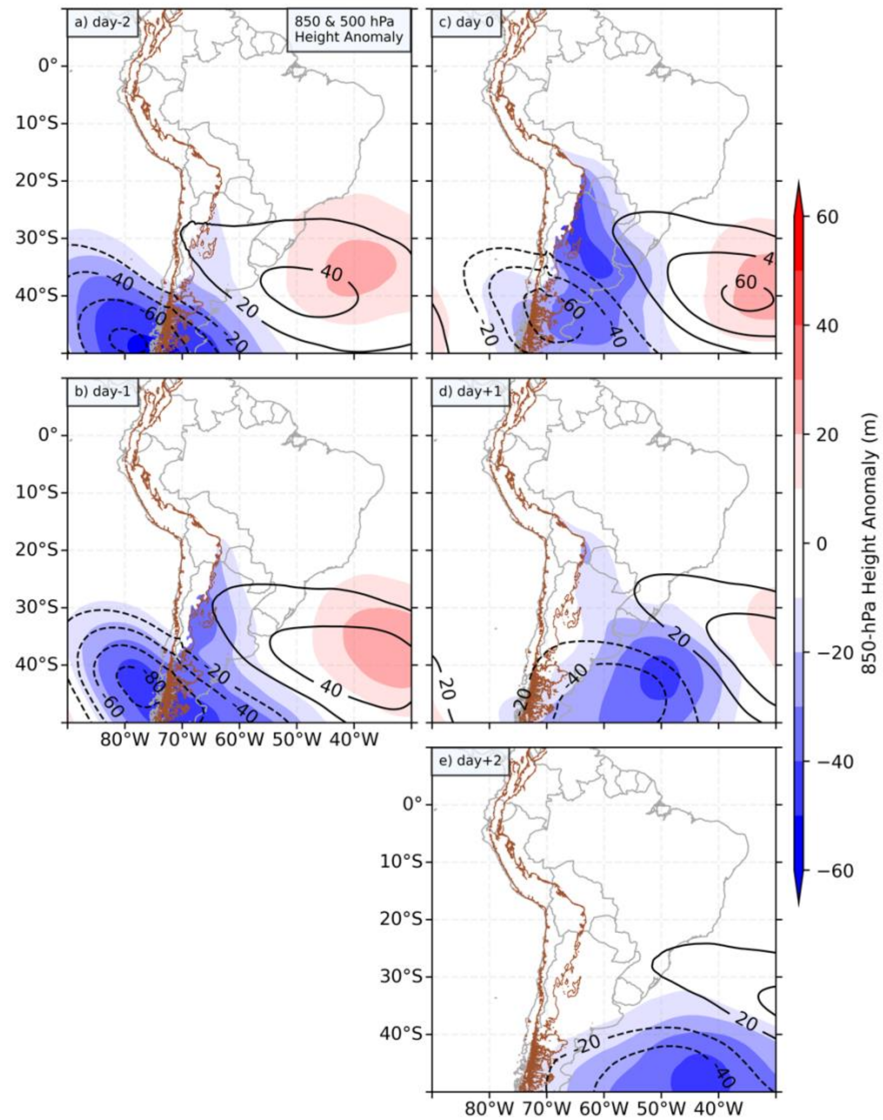

Figure 2.10. 24h-composite anomalies of 500 hPa (m, contours), and 850 hPa (m, shaded) geopotential height, for a) −60h to −37h (day−2), b) −36h to −13h (day-1), c) −12h to +11h (day 0), d) +12h to +35h (day+1), and e) +36h to +59h (day+2) with respect to the tornadic events. 800-m AGL elevation is indicated with brown contours to help the reader better visualize the main topographic features.

To support this hypothesis, Figure 2.11 shows anomalies of 850 hPa specific humidity and winds. The transport of water vapor from the Amazon to the Pampas region maximizes around the time the tornadoes take place. While the humidity anomalies maximize over the central Pampas (Figs. 2.11c-d), the maximum humidity transport anomalies (for the entire air column) occur in the Andes foothills between southern Bolivia and northwestern Argentina (not shown), where a strong 850 hPa humidity gradient is present and the SALLJ (Figs. 2.11c-d) is enhanced by the anticyclonic anomalies over the Atlantic and the low-pressure system around 30ºS (Fig. 2.10). The lee cyclogenesis in this region creates a pressure gradient that enhances the winds to the south, thus maximizing the humidity advection between 20 and 30ºS (Rasmussen and Houze 2016). This humidity transport is a key component in the tornadogenesis over SESA, which helps boosting the instability there (i.e., CAPE enhancement, Fig. 2.6a). However, elevated mixed-layers, which are relevant features for severe thunderstorms east of major mountain ranges, (e.g., Ribeiro and Bosart 2018), could also contribute to the CAPE generation before tornadogenesis, presenting avenues for future investigation. The moisture advection also sets the stage to produce severe storms when superposed with high vertical wind shear (induced by the synoptic forcing that enhances the meridional low-level jet and the westerlies at mid-levels; Figs. 2.10, 2.11, 2.12) (Piersante et al. 2021) and lifting mechanisms (e.g., orographic lifting caused by small topographic features). However, for tornado events that occur closer to the Atlantic Ocean, there may be a role for low-level moisture advection from oceanic sources as well. The synoptic composite results are notably like those presented by Rasmussen and Houze (2016) connected with convective modes associated with MCSs, providing support for the importance of large-scale forcing in severe weather environments in SESA in general. When partitioning the synoptic evolution composites by seasons, although modest variations in location and intensity, qualitatively similar synoptic features modulating the convective environment are seen (not shown). These results stand in contrast to Piersante et al. (2021) that showed strong synoptic forcing in austral spring (SON) and much weaker forcing in austral summer (DJF). As such, tornadic events in SESA appear to be strongly forced at the synoptic scale regardless of the season.

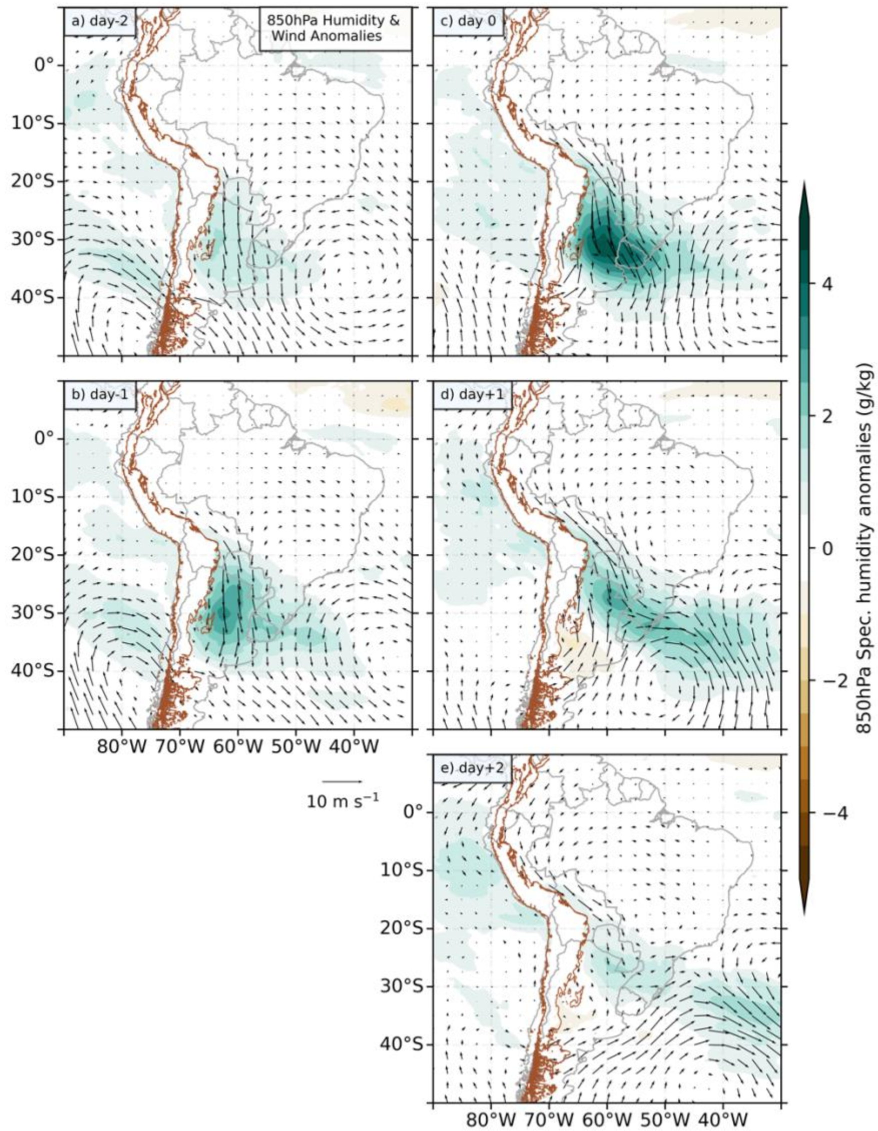

Figure 2.11. As Figure 2.10 but for 850 hPa specific humidity (gkg^{-1}, shaded) and winds (ms^{-1}, vectors).

2.5.2 Planetary scale and teleconnections

Several previous studies have examined how synoptic-scale modulate convective storms and severe weather production in SESA (Rasmussen and Houze 2011, 2016; Rasmussen et al. 2014; Piersante et al. 2021; Lopes 2020). However, a connection to planetary-scale patterns connected to tornado events in SESA has not previously been examined in detail. To address this gap, we examine how global teleconnection patterns influence tornadic storms in SESA. 250 hPa geopotential height and zonal wind anomalies (Fig. 2.12) show a well-defined wave-train pattern connecting South America and the tropical west Pacific a few days before a tornado occurs. The pattern resembles the PSA pattern found in previous studies (Mo and Higgins 1998; Mo and Paegle 2001), which can be modulated by remote heating with the MJO and other phenomena. The trough-ridge-trough pattern can be traced up to 7 to 9 days prior to a tornado event in SESA and diminished afterward (not shown). The portion of the wave train located over South America resembles the pattern analyzed in the 500 and 850 hPa fields (Fig. 2.10) and in prior research (Rasmussen and Houze 2011, 2016; Piersante et al. 2021), where an anomalous trough located over southern Chile is about to cross the Andes, flanked by an anomalous downstream ridge. Another interesting aspect is that the ridge located over the Southern Ocean around 140ºW-120ºW (Figure 2.12c-d) intensifies a few days before the tornado day, possibly supporting downstream amplification of the wave pattern over South America and its northeastward displacement. A detailed examination of individual cases could confirm this hypothesis, including a possible role for wave breaking, which is left for future work. Thus, it appears that the strong synoptic forcing accompanying severe thunderstorms in SESA is connected to large-scale circulations having a remote origin.

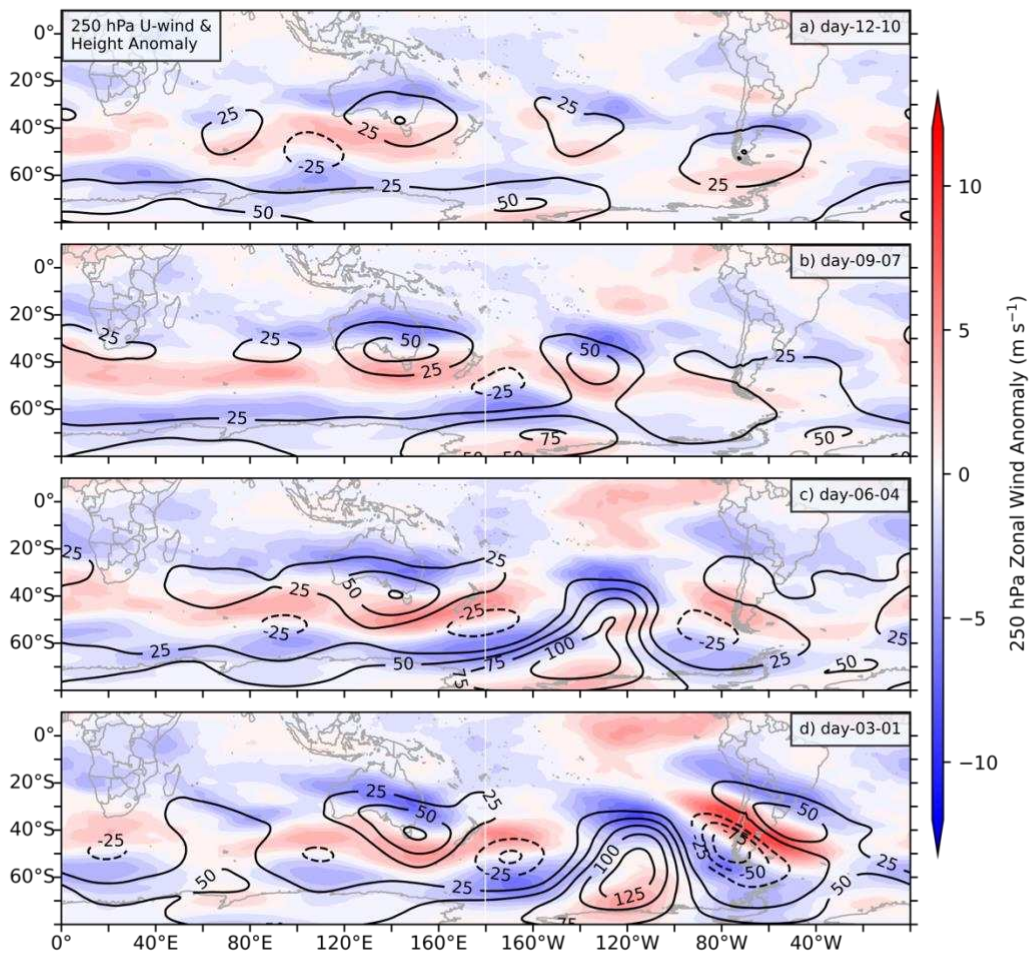

Figure 2.12. Triad composite anomalies of the 250 hPa geopotential height (m, contours) and zonal wind (ms^{-1}, shaded) prior to the development of tornadoes in SESA, a) 10-12 days, b) 7-9 days, c) 4-6 days, and d) 1-3 days before the events.

To get insights into the initiation mechanism of the stationary Rossby wave train pattern influencing severe weather in South America, composites of outgoing longwave radiation (OLR) anomalies are computed (Fig. 2.13). A negative OLR signal, indicating cold cloud tops and deep convection, is prominent on the northwestern Australian coast 7 to 9 days before the tornadic storms develop in SESA. This signal strengthens by Day –4 to –6, and then begins to diminish. Negative OLR anomalies are indicative of enhanced convection occurring over the area, which may provide a Rossby wave source that produces the wave-train signal seen in the composite 250 hPa field. Composites of the PSA modes conducted by Mo and Paegle (2001) show a similar wave train pattern connected to convection in the Maritime Continent that resembles that of Figure 2.12d. The fact that the OLR anomalies are stronger for the −4 to −6 triad in Figure 2.13 versus a stronger Rossby wave pattern on the −1 to −3 triad in Figure 12 gives some support to the idea that anomalous convection over northwestern Australia triggers a wave train that arrives in South America a few days later.

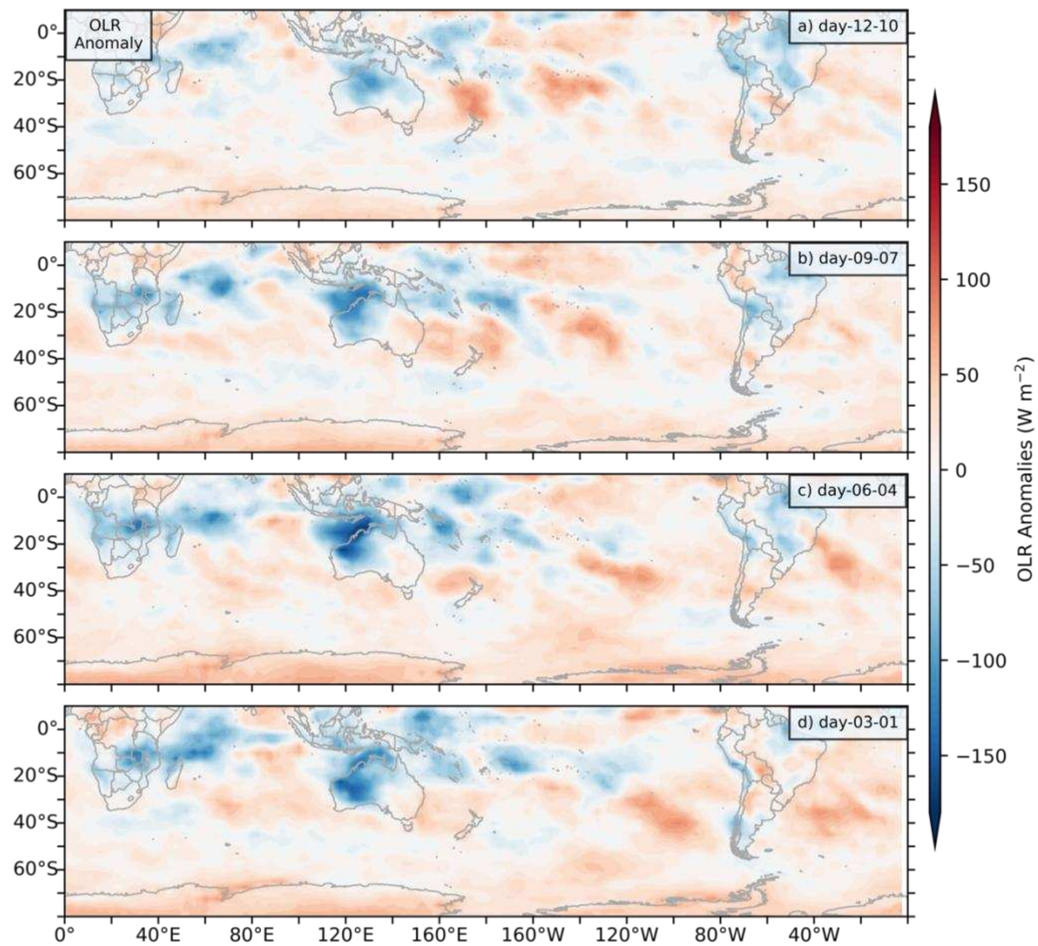

Figure 2.13. As in Figure 2.12, but for outgoing longwave radiation anomalies (Wm^{-2}, shaded).

Previous studies have shown that disturbances like the MJO can produce teleconnection patterns such as this (e.g., Grimm 2019; Sena et al. 2022). An analysis of the distribution of the MJO phases from 15 to 0 days prior to the development of every tornado event is performed, including a breakdown by season (Fig. 2.14). The histograms show that when all months are considered, tornadoes are most frequent when the MJO is active in phase 3 (20%). Phases 2 and 4 are the second most frequent (near 15% each), but their values are not significantly different from random chance across all phases. A breakdown of the distribution into shorter periods (e.g., triads, like Figures 2.12 and 2.13) showed no significant differences in the predominant phases. Composite MJO events tend to have enhanced convection to the northwest of Australia in association with these phases (Wheeler and Hendon 2004), although generally further away from the continent than shown in our Figure 2.13 OLR composites. This mismatch is probably caused by the poor representation by the RMM index of the MJO convection as its computation is dominated by the wind components rather than OLR (see Straub 2013, and Liu et al. 2016 for further details). Phase 5 also shows significant suppression of tornadic storms. In terms of the seasonal distribution, both summer and autumn tornadoes are dominated by MJO phase 3 during the previous two weeks (~25%), though the MJO phases that exhibit a significant suppression of tornadic activity are not consistent (phases 1 and 8 for DJF vs. 1 and 5 for MAM, between 5% and 8%). The spring season presents a distinct distribution, however. The active MJO phases associated with most frequent tornadoes (over 17%) are 1, 2, and 4, with the latter showing the highest frequency (~21%). On the contrary, phases 5, 6, and 7 show significant tornado suppression (below 8%), with phase 6 being present in only 3% of the events. In this regard, the impact of the MJO on tornado formation seems to vary more smoothly during SON, versus DJF and MAM which are noisier.

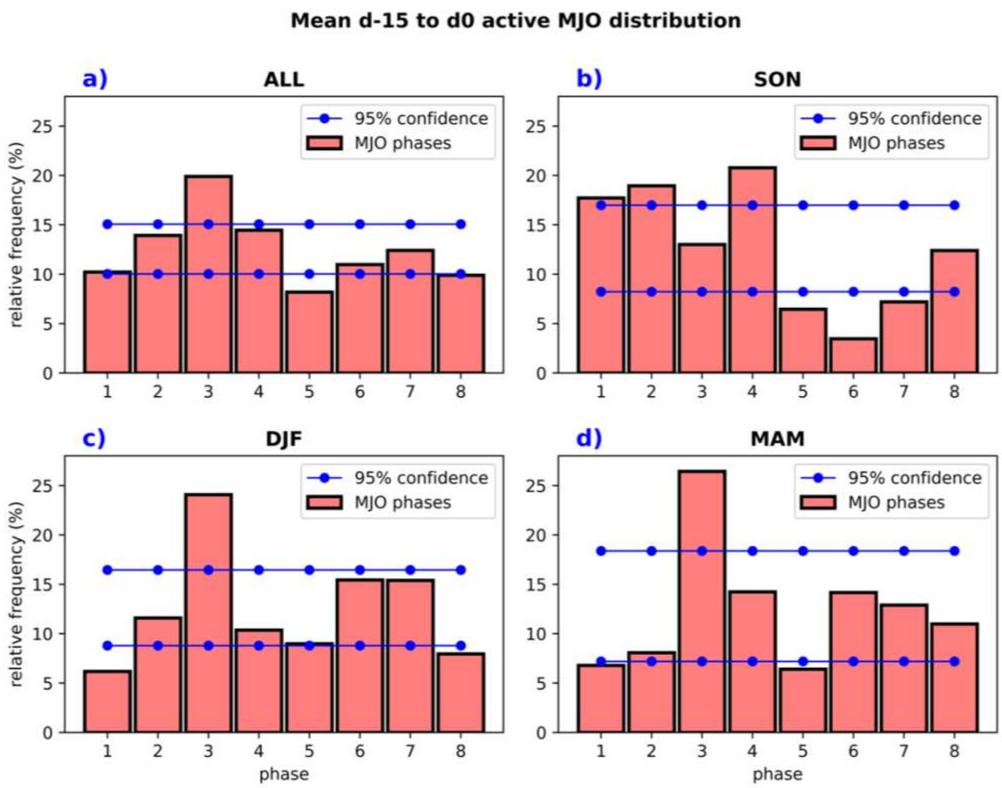

Figure 2.14. Histogram of the MJO active phase distribution for the 16-day period prior to the tornadic events, considering a) all events, b) SON, c) DJF, and d) MAM events only. The 95% confidence interval (blue line) is computed by applying a bootstrap test with 10,000 realizations.

2.6 Conclusions

The environment supportive of tornadic storms in Southeast South America (SESA) is analyzed, focusing on the mesoscale, synoptic, and planetary-scale patterns that contribute to their development. Tropical teleconnections that contribute to these large-scale patterns were assessed. This is the first time that the supporting environment for tornadoes in SESA has been studied on a multiscale basis, based on a new self-constructed database of reports from the last 30 years and using novel reanalysis data with high spatial and temporal resolution. Results highlight important similarities in the convective environment that sustains tornadoes in the U.S. and SESA, though key dissimilarities in some parameters were found.

Consistent with a convective season that is active from spring through fall (Zipser et al. 2006; Rasmussen and Houze 2011), the tornado database used here shows that tornadoes in SESA are relatively common in all seasons except winter (Fig. 2.2a). Tornadoes mostly form in late afternoon, although they sometimes occur in the evening and during the night (Fig. 2.2b). The spatial distribution of reports was found to be like the distribution of events collected over earlier periods of the 20th century for Argentina (Schwarzkopf 1988), with most the reports over the plains, and only a few near the Andes foothills (Fig. 2.1). Lack of reports south of the Sierras de Córdoba (Fig. 2.1) is consistent with unfavorable conditions for tornado formation observed there (Figs. 2.7 and 2.8).

ISCCP data was used to show that tornadoes in SESA are embedded in a wide variety of storm sizes, ranging from discrete storms to large MCSs (Fig. 2.3). Tornadoes appear to be more regularly embedded in isolated thunderstorms or small MCSs rather than large convective systems. Nocturnal tornadoes are associated with 20% larger cloud shield systems compared to daytime events.

Several dynamic and thermodynamic parameters known to influence tornadic environments were composited across all the tornadoes reported. Proximity environment evolution before and during tornadoes showed that strong instability, deep-layer vertical shear, and storm-relative helicity need to be built, while convective inhibition and lifting condensation level need to be reduced, prior to or during the development of tornadic storms in SESA (Fig. 2.6). At the time of tornado occurrence, high-CAPE, high-BSH06, and low-LCL were generally preferred while no clear preference was observed for BSH01, though particularly low values were observed for most of the events close to the high terrain (Fig. 2.4). Also, a curved hodograph with anticyclonic rotation was observed, presenting strong low-level directional shear but weak speed shear (Fig. 2.5).

The SESA tornadic environments analyzed in this study are compared with other studies focused on U.S. Great Plains tornadoes. In SESA, parameters such as MLCAPE, BSH06, and MLLCL presented values broadly supportive of tornadic storms, according to typical U.S. values. However, weak low-level dynamic environments (BSH01 and SRH01) and moderate convection inhibition (MLCIN) found for SESA tornadoes versus those in the U.S. would make their formation more difficult in the U.S. This is echoed by the moderate STP values reported (Figs. 2.6h, 2.8), although an STP maximum located equatorward of the tornado locations (Fig. 2.9) could help determine potential areas for tornadogenesis. Thus, more research is required in determining STP's effectiveness in predicting tornadoes of all intensities in SESA. Geographical disparities, in particular the taller mountain range east of SESA relative to the Rockies and U.S. Great Plains and their impact on the generation of low-level flows and associated moisture advection, could explain some of the observed differences in frequency and environments supporting tornadic storms in the U.S. versus SESA. Thus, these differences should be more carefully analyzed in future work, likely in numerical modeling simulations, to understand how contrasts in topography, moisture source, wind shear generation throughout the troposphere, and environmental parameters influence the nature and evolution of tornadic storms in both continents (e.g., Li et al. 2023).

The mesoscale environments associated with tornadic storms are supported by strong synoptic forcing in both austral spring and summer that initiates cyclogenesis in the lee of the Andes (Fig. 2.10) and enhances the upper-level zonal winds (Fig. 2.12e), resulting in an enhanced SALLJ yielding sufficient moisture to aid in destabilizing the atmosphere (Fig. 2.11) and strong deep-layer shear supporting organized storms in the region. This forcing also provides lifting mechanisms that along with terrain features, initiate the storms that subsequently become tornadic. The anomalous trough required to set the stage for tornadic storms appears to displace slowly while crossing the Andes, so the persistence of the forcing may be a relevant factor for tornado formation in SESA.

Zooming out to hemispheric scales suggests that convection near the northwestern coast of Australia may influence SESA tornado occurrence via teleconnection patterns (i.e., Rossby waves) that influence the synoptic-scale environment over SESA. The teleconnection pattern resembles the Pacific South American pattern, found in previous studies (Mo and Higgins 1998; Mo and Paegle 2001). MJO analysis further supports the relationship of tornadoes in SESA with tropical sources, suggesting the preferred presence of phase 3 in the RMM index during the two weeks prior to a tornado event, although isolating the season of SON shows a broad enhancement of tornado activity across MJO phases 1 through 4. These results may be useful from a predictability standpoint and suggest there could be skill in identifying synoptic and mesoscale configurations that may lead to severe weather hazards — including tornadoes — over SESA up to a week or two in advance. This is the first study that connects tornadic storms in SESA to large-scale patterns induced by remote tropical sources in a climatological sense.

The multiscale approach employed here illustrates the relevance of atmospheric processes occurring at different spatial and temporal scales in the occurrence of tornadoes (Tochimoto 2022). Improving observing systems and encouraging routine collection of severe weather reports in South America are urged, as future studies using denser observational data and reports would give new and improved insights into the convective environments that support tornadoes in SESA, including validation of results from this investigation — mostly based on reanalysis data.

Exploration of new sources of predictability from tropical teleconnections and elsewhere can also be extremely useful for providing early weather outlooks to emergency management agencies to prepare the population for severe weather threats, especially in highly vulnerable communities across the continent. Lastly, assessing future changes in the convective environment due to climate change requires comprehension of current severe weather signatures in the region, which has urgency given the increasing frequency of extreme weather across the planet.

CHAPTER 3

Modulation of Storm Features in South America by the Madden-Julian Oscillation [3]

3.1 Introduction

Convective storms are a frequent and critical component of the hydrological cycle in the tropics and subtropics of South America during the warm season (Romatschke and Houze 2010; Houze et al. 2015; Rasmussen et al. 2016). Thanks to the abundance of atmospheric moisture and surface warming in this season, along with a maritime-like environment, a prominent diurnal cycle in convection and precipitation is observed over the Amazon basin (da Rocha et al. 2009; Giles et al. 2020). However, in the subtropics less abundant local moisture implies that water vapor transport toward the region is often needed to produce moist convection (e.g., Salio et al. 2007; Varuolo-Clarke et al. 2022; Sasaki et al. 2024), which makes the variability of convective activity inherently larger in this region (Liebmann et al. 1999). These regional differences in the variability of convection in tropical and subtropical South America and their implications on the three-dimensional characteristics of summer storms are the scope of this investigation.

One of the main drivers of atmospheric variability in South America is the Madden-Julian Oscillation (MJO) (Liebmann et al. 1999; Paegle et al. 2000). The MJO is the leading mode of intraseasonal variability in the global tropics, corresponding to an eastward propagation of large-scale convection that repeats its cycle approximately every 30-90 days (Madden and Julian 1971). MJO deep convection and associated anomalous heating over the tropical Indian and west Pacific Oceans excites stationary planetary Rossby waves and a tropical Kelvin wave-like response near

[3] This chapter contains material that is currently under review to be published in *Journal of the Atmospheric Sciences*. (**Veloso-Aguila, D.**, E. Maloney, and K. L. Rasmussen, 2025a: Modulation of Storm Structures in South America by the Madden-Julian Oscillation. *Journal of the Atmospheric Sciences*, under review)

the equator that induces anomalous circulations in remote areas (Rydbeck et al. 2013). The Kelvin wave-like response features bands of easterly and westerly wind anomalies confined to the equatorial band that radiate eastward from the region of enhanced convection in the Indo-Pacific warm pool. When the eastward-propagating MJO convective center reaches colder waters east of the International Date Line, deep convection is no longer supported, but the wind perturbations continue circumnavigating the equator, modifying the atmospheric large-scale environment in tropical remote regions, including over continental areas (Milliff and Madden 1996; Matthews 2000). Additionally, stationary Rossby waves induced by MJO heating propagate across the Southern Hemisphere extratropics, reaching South America. Grimm (2019) demonstrated with model experiments how MJO-induced upper-level divergence in the western Pacific can reproduce the observed tropical-extratropical upper-level wave train reaching South America. This wave train resembles the well-known Pacific-South America teleconnection pattern, which has been described as one of the dominant modes of variability of the upper-level circulation in the Southern Hemisphere at intraseasonal timescales (Mo and Higgins 1998; Mo and Paegle 2001). Over South America, this wave pattern features large-scale cyclonic and anticyclonic anomalies that can alter the convective environment (Mo and Higgins 1998; Cunningham and Cavalcanti 2006; Stan et al. 2017).

Before the 1997 launch of the Tropical Rainfall Measuring Mission (TRMM) satellite (Kummerow et al. 1998), precipitation radar measurements were limited to regions with ground-based instrumentation. The TRMM satellite, with the first spaceborne radar, enabled the study of three-dimensional precipitation structures in previously unexplored areas, including tropical and subtropical South America (Romatschke and Houze 2010; Rasmussen and Houze 2011; Houze et al. 2015). Given that TRMM broadly covered tropical and subtropical regions, long-term climatologies of rainfall and physically-based studies looking at the nature of convective storms were made possible. Different studies have used TRMM and ground-based radar observations to document how distinct cloud structures vary from MJO enhanced to suppressed convection phases across the Indo-Pacific warm pool (Morita et al. 2006; Barnes and Houze Jr. 2013; Zuluaga and Houze 2013; Powell and Houze Jr. 2013; Virts and Houze 2015). One of the most common storm modes identified in precipitating cloud structures in the Indian and western Pacific oceans during active MJO phases are broad stratiform regions, while during suppressed MJO stages other storm modes such as shallow isolated convection maximize (Barnes and Houze, 2013). Other studies analyzing rainfall and lightning within the MJO convective cycle across the Indo-Pacific warm pool have found that deeper storms with enhanced lightning production, occurring under an anomalously unstable environment, predominate during suppressed MJO phases; active phases favored large mesoscale convective systems with reduced lightning and dominant stratiform rain fraction, under a less unstable environment (Morita et al., 2006; Virts and Houze, 2015). Very few studies have investigated the remote MJO influence on cloud structures across the global tropics (e.g., Riley et al. 2011), and no studies to our knowledge have been conducted over subtropical regions.

In South America, multiple studies have documented the influence of MJO teleconnections on intraseasonal variability in precipitation and extreme event occurrence at daily and regional scales (Carvalho et al. 2004; De Souza and Ambrizzi 2006; Barrett et al. 2012; Alvarez et al. 2016; Grimm 2019; Mayta et al. 2019; Rondanelli et al. 2019; Recalde-Coronel et al. 2020; Jacques-Coper et al. 2021; Veloso-Aguila et al. 2024). For precipitation, most studies have focused on the MJO modulation of daily rain accumulation during the warm season. The predominant regional intraseasonal pattern observed in summer corresponds to a precipitation anomaly dipole between tropics and subtropics of South America, with enhanced precipitation in the central and eastern tropics across phases 8, 1, and 2, and in eastern subtropics for phases 3, 4, and 5 (suppressed precipitation occurs in these regions for opposite phases of the MJO cycle) (Nogués-Paegle and Mo 1997; Alvarez et al. 2016; Grimm 2019). These precipitation enhancements in the subtropics have been linked to the strengthening of the South American Low-Level Jet (SALLJ; Vera et al. 2006; Montini et al. 2019; Sasaki et al. 2022), mainly due to transport of tropical moist air poleward into the plains (e.g., Veloso-Aguila et al. 2024). Recent studies have shown that the MJO can modulate the occurrence of SALLJ events (Jones et al. 2023).

However, little work has been conducted on the modulation of the storm structures leading to those rainfall anomalies in South America, which could provide a broader range of potential impacts besides simply modifying intraseasonal precipitation. Bruick et al. (2019) analyzed the impact of El Niño Southern Oscillation on the structure of intense convective storms in subtropical South America and found that while the frequency of these storms does not change significantly, their echo top heights are higher during El Niño years. While variations in precipitating storm structures as a function of MJO phase have been described locally over the Indo-Pacific warm pool region, we are not aware of any studies in the peer-review literature that have explicitly examined this for South America or elsewhere. Understanding the influence of the MJO on storm modes in South America could help anticipate periods where certain impacts could be more likely, such as flash flooding or severe storm impacts (Zhang 2013). For this reason, the present study aims to explore the MJO modulation of precipitating storm structures in the tropics and subtropics of South America during the summer season. The research questions that drive this study are: Does the MJO modulate the occurrence of certain storm features in South America? If so, what is the nature of this modulation? Is the character of storm mode variability associated with the MJO different between tropical and subtropical South America? How do variations in the large-scale environment produced by the MJO support these modulations of storm properties? Answering these questions could provide novel insight into the MJO influence on storm features over South America.

3.2 Data and Methods

3.2.1 TRMM Satellite

Observations from the TRMM satellite (Kummerow et al. 1998) are used to characterize the nature of precipitating systems in South America in this study. In particular, three-dimensional reflectivity data from the TRMM Precipitation Radar (PR) that covered the globe from 36.5ºN and 36.5ºS during the period 1998-2014 is utilized. The PR had a frequency near 13.8 GHz (Ku-band), with a minimum reflectivity sensitivity of around 17 dBZ, and a 250-km wide swath, providing three-dimensional reflectivity at about 4.3 km and 0.25 km horizontal and vertical resolution, respectively. Based on 2A25 rainfall retrievals from the PR, a widely used precipitation feature (PF) database that groups pixels with contiguous 2A25 detectable rainfall rates as independent objects is utilized (Liu et al. 2008). As is standard for this established database, a minimum of four contiguous pixels is used to identify an independent PF object, following the same criteria used in previous studies working with PFs (Nesbitt et al. 2000; Cecil et al. 2005; Zipser et al. 2006; Liu et al. 2008; Liu and Zipser 2015; Zipser and Liu 2021, among others). This strategy helps to remove spurious data from isolated pixels, including unmitigated ground clutter. Under this definition, we include storms as small as 75 km^2 with rainfall rates as weak as 0.1 mm/h (e.g., large cumulus congestus clouds) up to large mesoscale convective systems with heavy rainfall and severe impacts (although there are limitations in the width of the systems viewed given the 247 km wide swath of the TRMM PR data). Compared to the large minimum reflectivity sensitivity with longer wavelength ground-based radars (i.e., S- and C-band), the Ku-band TRMM PR can detect very weak convection, as demonstrated by other studies analyzing shallow isolated convection across the globe (Houze et al. 2015).

Using this approach, different storm-related features associated with each independent object can be extracted. In this study, we focus on three storm features: volumetric rain rate (VOLR, the accumulated rain over the surface area of the respective object), storm horizontal extent (AREA, the number of contiguous precipitating pixels, represented as total area), and maximum height of 40 dBZ radar reflectivity echoes (MXHT40, a proxy for updraft strength; the higher these echoes can reach on a PF, the more vertical development and intense the storm (Cecil et al. 2005; Zipser et al. 2006)). We focus on these three variables as they represent distinct aspects of storm spatial structure and associated rainfall. Other variables either strongly covary with the variables mentioned above (e.g., flash count or maximum echo top height) or do not show a clear modulation by the MJO (e.g., number of individual PFs or maximum rain rate) (not shown). Since we analyze convective storms in South America, we focus on the austral summer season (December-January-February), when storms are generally most intense and frequent over the region (Zipser et al. 2006; Rasmussen et al. 2016).

3.2.2 ERA5 Reanalysis

The fifth-generation ECMWF reanalysis data, ERA5 (Hersbach et al. 2020), is utilized to characterize the environmental conditions that accompany convective activity at regional and global scales. ERA5 is provided on a regular 0.25º by 0.25º horizontal grid and 1-hour temporal resolution and used during 1998-2014 to match the TRMM observational period. Anomalies of various fields are computed by subtracting the day of year climatology derived from the average of the 17-year record, after being smoothed with an 11-day running mean. Additionally, ERA5 profiles included in the PF database were extracted for each individual PF at the closest grid point to the center of the object and closest hour of observation.

3.2.3 MJO Index

The daily RMM index (Wheeler and Hendon 2004) is used to define MJO activity. This index is computed using the leading two principal components of anomalous tropical lower and upper troposphere winds and OLR. Seasonal cycle (120-day mean) and ENSO variability are removed from the index computation. It represents the MJO with a phase (corresponding to the location of enhanced convection) and an amplitude. Eight phases are defined representing the approximate location of the associated enhanced convective region across the tropical oceans. To document the remote effects associated with planetary waves excited by MJO convection, we define active MJO days as when the RMM index has an amplitude greater than or equal to one. Composite analysis is used to obtain mean conditions in each of the eight phases when the MJO is active.

Nearly 1000 MJO active days were observed during summer between 1998 and 2014, ranging from as few as 67 MJO days in phase 1 and as many as 174 days in phase 7 (see Figures 3.8 and 3.10 for further details on MJO days per phase). While these numbers are likely sufficient to extract meaningful results, we acknowledge that not all the MJO days per phase represent an independent MJO event as a given phase can sometimes persist for multiple consecutive days, which could lower the total number of independent events being composited. Time-lagged analysis was not considered in this study, as the quasi-periodic nature of the MJO (evidenced by Figure 3.3) suggests that information from previous phases is reflected in subsequent phases, and thus time lagged responses are already contained to some extent in the composite analysis.

A t-test was performed to include confidence intervals as error bars in some of the composites conducted per MJO phase, which helps to discriminate whether an anomalous signal for a given MJO phase is significantly different from zero or from other phases' signal. The total number of active MJO days per phase was used as the total number of samples for the statistical testing.

3.2.4 Intraseasonal filtering

A bandpass filter is applied in the 30-90-day range to anomalies of various atmospheric fields to isolate intraseasonal features relative to other timescales (e.g., synoptic-scale disturbances or interannual variability from other climatic oscillations).

3.2.5 Study area

The study area corresponds to tropical and subtropical South America (Figure 3.1). In particular, this study focuses on the analysis of convective storms to the east of the Andes, where convection is frequent in summer (e.g., Rasmussen et al. 2016). A climatology of precipitation is shown in Figure 3.1b, with the Amazon generally having more mean rainfall than the subtropic plains. For regions to the west of the Andes mountains and the northernmost portion of SA, DJF is the dry season, and so those areas were not considered as part of the analysis (Figure 3.1). While in Chapter 3.3.2 the spatial modulation of various atmospheric variables across the continent is described, Chapters 3.3.3 and 3.3.4 examine the MJO modulation in storm features occurring over portions of the tropics and subtropics, respectively. Based on the spatial modulation of precipitation and the homogeneity of rainfall regimes, the tropics region selected covers the continental area east of 60W (Figure 3.1), where similar storm regime modulation occurs at intraseasonal timescales (Chapter 3.3.3). The tropical area west of 60W is not considered part of the analysis because it shows a marginal MJO modulation of storm features (not shown). The subtropics region selected corresponds to the Andes foothills and the Pampas, omitting part of southeast Brazil, where the Brazilian highlands and the occasional influence of the South Atlantic Convergence Zone makes the convection regime in this region distinct compared to the plains and the Andes foothills.

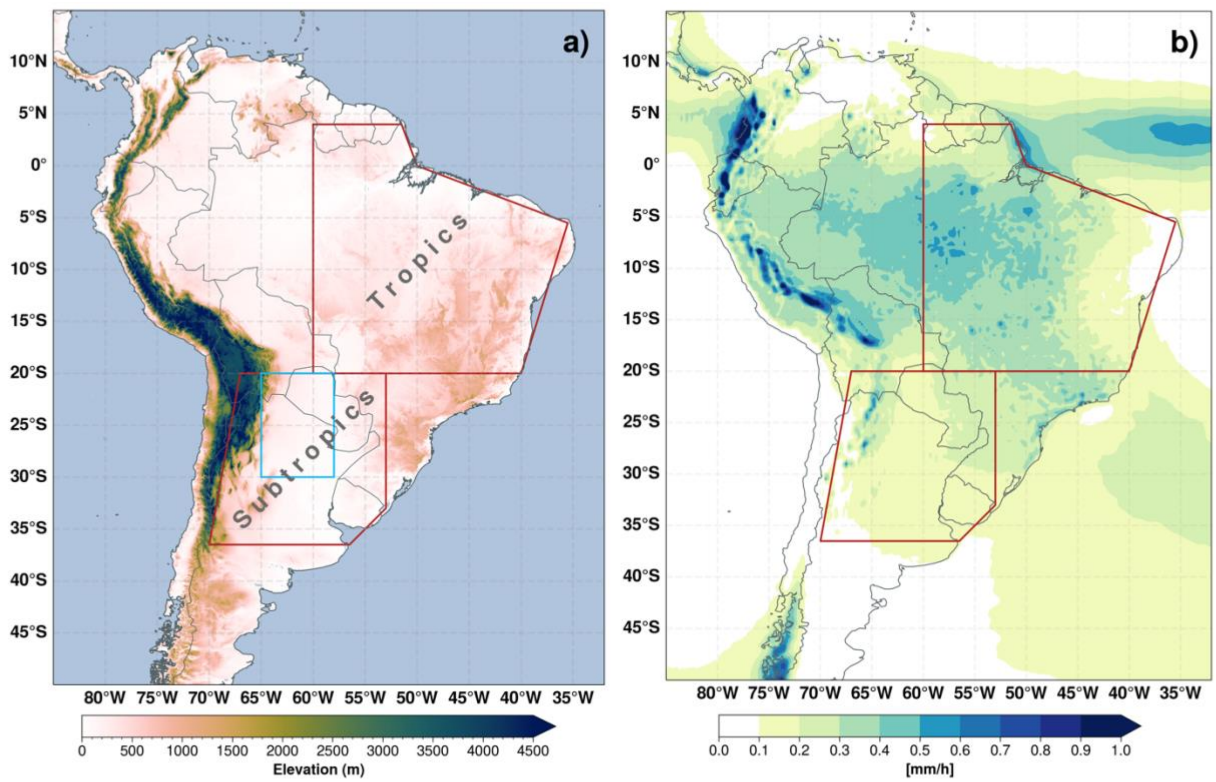

Figure 3.1. a) Topographical map of South America (elevation is in meters). Red polygons represent the tropical and subtropical regions selected to conduct storm feature analyses using TRMM observations. The light blue box indicates the region where the South American Low-Level Jet was calculated (see Table 3.1). b) Austral summer climatology of precipitation rate (mm/h) in ERA5 data during 1998-2014.

3.3 Results

3.3.1 MJO Teleconnections

The MJO modulates the atmospheric circulation in the Southern Hemisphere, as previous studies have demonstrated (e.g., Carvalho et al. 2005; Alvarez et al. 2016; Grimm 2019) While these studies have already presented results on MJO teleconnections and their impacts over South America, they are included and analyzed here for the benefit of the reader. Figure 3.2 shows composite intraseasonal anomalies of 200 hPa wind and 850 hPa geopotential height as a function of MJO phase during austral summer. In the tropics, near-equatorial zonal wind anomalies and associated regions of upper-level convergence and divergence propagate eastward as the MJO evolves through its lifecycle. Areas of enhanced (suppressed) convection near the equator generally reflect divergence (convergence) in the upper troposphere. A more compact depiction of this equatorial MJO propagation in the tropics is shown in Figure 3.3, where the propagation of the composite MJO 850 hPa geopotential height and wind signal is displayed from 15 days before the day at which the MJO phase is defined. The center of action of the low-level atmospheric pattern associated with the low-level divergence (approximately where positive geopotential height anomalies are located) and convergence (negative geopotential height anomalies) branches both propagate eastward at a speed of ~5.6-6.3 m/s. While MJO convection anomalies generally do not extend past 160W in the central Pacific (not shown), associated zonal wind anomalies travel across the entire tropics. Anomalies at 850 hPa are weak over tropical South America (80W-50W) at all phases likely due to blocking by the Andes (Matthews 2000; Kiladis et al. 2005; Yu et al. 2011), but at upper levels substantial wind anomalies and regions of convergence and divergence occur over South America that can influence convection (e.g., Figure 3.2). The average eastward propagation pattern at lower and upper levels is consistent with the signal presented in previous studies (e.g., Madden and Julian 1972; Grimm 2019). The wind anomalies observed impinging on tropical South America depict a radiating Kelvin-wave signal forced by MJO heating that impacts the large-scale tropical circulation and convergence in South America (Rydbeck et al. 2013).

In the extratropics, the MJO is known to influence anomalous atmospheric circulations through stationary Rossby waves (Mo and Higgins 1998; Mo and Paegle 2001). This can be observed in Figure 3.2 where an extratropical wave-like pattern is apparent at most phases. An examination of behavior near South America indicates that circulation anomalies of different signs and intensities are observed in midlatitudes spanning the continent and vary depending on the MJO phase. For example, the environmental conditions for phases 7, 8, and 1 feature a dipole of low-level geopotential anomalies sitting on both sides of South America's southern tip that grows and moves northward into the subtropics. An opposite-signed dipole develops between phases 3, 4 and 5 over the same region. This signal has implications for the predominant weather patterns and moisture transport that occur during particular MJO phases, as will be shown in the next section.

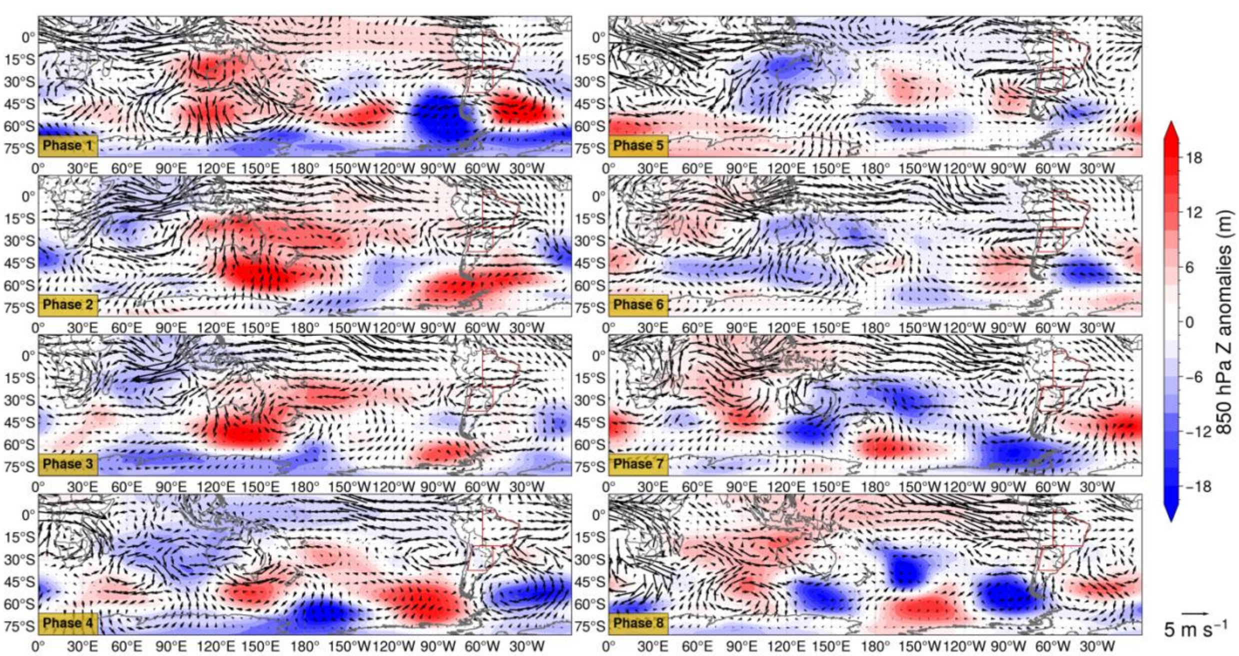

Figure 3.2. Composite maps of austral summer intraseasonal (30-90 days) anomalies of daily mean 850 hPa geopotential height (shaded) and 200 hPa horizontal winds (vectors). Every panel represents mean conditions observed at each (active) phase of the MJO.

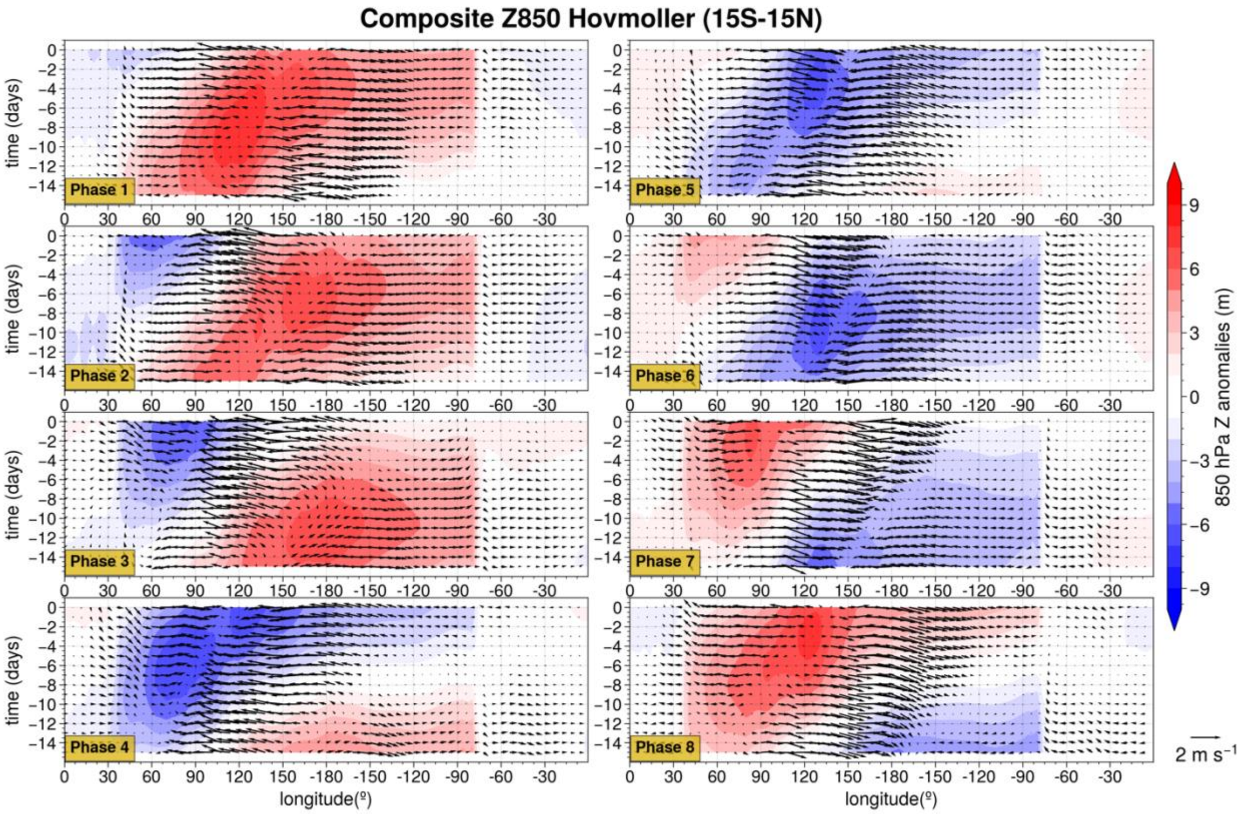

Figure 3.3. Composite time-longitude diagrams of austral summer intraseasonal (30-90 days) anomalies of 850 hPa geopotential height (shaded) and winds (vectors). Daily mean values are obtained by averaging across the tropics (15N-15S). Every panel represents mean conditions observed at each (active) phase of the MJO (day 0) and up to 15 days before.

3.3.2 Regional modulation of atmospheric conditions in South America

One of the direct effects of the MJO on the South American continent is induced large-scale vertical motion associated with the transient equatorial circulation response to MJO heating in the west Pacific. This MJO heating can also indirectly induce anomalous regional circulations over the continent through Rossby wave trains that propagate across the Southern Hemisphere extratropics, as was discussed in the previous section. These perturbations can cause enhancement or suppression of convection, which subsequently reinforces regions of atmospheric convergence or divergence. Figure 3.4 shows maps of intraseasonal vertically-integrated moisture divergence, composited by MJO phase. These maps are highly correlated with maps of vertical velocity at 500 hPa, where areas of moisture divergence are collocated with downward motion and areas of moisture convergence coincide with upward perturbations (not shown). Tropical South America is generally characterized by convergence and upward motion that initiates during phase 7 and further expands in phases 8 and 1. The opposite phases of the MJO cycle generally show divergence and downward motion, starting in phase 3 and further expanding in phases 4 - 6. However, the northwest part of tropical South America is characterized by opposite-signed anomalies relative to the rest of the tropical continental area. Subtropical South America also provides a contrast, where generally opposite signed anomalies occur relative to central and eastern tropical South America for most MJO phases, although the signal is less spatially coherent.

A common starting point to explore the implications of MJO teleconnections for South American convective storms is through precipitation anomalies. MJO-induced variability on precipitation in tropical and subtropical South America has been well described in multiple studies (e.g., Carvalho et al. 2004; De Souza and Ambrizzi 2006; Alvarez et al. 2016; Grimm 2019). For the benefit of the reader, this relationship is presented and analyzed here (Figure 3.5). The precipitation anomalies are consistent with regions of anomalous moisture divergence, where enhanced precipitation is associated with moisture convergence in both the tropics and the subtropics. In the tropics, the opposite phases of the MJO cycle (compare left and right panels in Figure 3.5) generally show different signed precipitation anomalies. Phases 8 - 1 show strong positive anomalies over most of the tropics, except in the northwest Amazon. A shift to negative anomalies is observed in the central Amazon at phase 3, with negative anomalies growing and propagating eastward from phases 4 to 6. The northwest region consistently shows opposite signed anomalies to the rest of the tropics across these phases. In the subtropics, precipitation anomalies also change sign across an MJO lifecycle (left versus right panels in Figure 3.5) and are broadly out of phase with those in the Tropics, especially for phases with strong precipitation anomalies. The anomalies tend to be stronger across portions of the subtropical plains and southern Brazil, where positive (negative) anomalies are generally observed for phases 3 - 5 (7, 8, 1). In the Andes and its foothills, precipitation anomalies are weaker, but positive anomalies occur during phases 7 and 8.

To further explore the atmospheric drivers of the precipitation patterns shown above, intraseasonal anomalies of precipitable water and integrated water vapor transport are analyzed (Figure 3.6). In the tropics, moisture anomalies are generally correlated with the location of precipitation anomalies (Schiro et al. 2016). Here, moisture transport anomalies are mostly zonal and show convergence or transport where moist anomalies are observed and divergence when dry anomalies are present, especially over eastern Brazil. This correspondence appears stronger for the MJO phases with the largest precipitation perturbations in central and eastern tropics (e.g., phases 8-1 in wet regime and 4-5 in dry regime), but during the transition phases (e.g., phases 2-3) this relationship is less clear. These discrepancies could be due to the relationship between precipitable water and precipitation rate in tropical regions being stronger at subdaily timescales, whereas at daily timescales this relationship might get degraded or stronger at a lag (Schiro et al. 2016). In the subtropics, moisture anomalies appear strongly linked to the transport of moisture from the tropics, a signal particularly prominent during certain MJO phases. An increase in moisture in the atmospheric column is associated with northerly transport anomalies. The positioning of this enhanced moisture transport coincides with the expected location of the South American Low-Level Jet (SALLJ, Vera et al. 2006; Montini et al. 2019; Sasaki et al. 2022; Jones et al. 2023), which is known to modulate moisture and precipitation anomalies downstream (Salio et al. 2007; Nascimento et al. 2016; Piersante et al. 2021; Sasaki et al. 2024). The stronger the transport and its meridional extension, the larger the precipitable water and precipitation anomalies in Figure 3.6 (e.g., phases 3 and 4). The opposite effect is observed when southerly transport anomalies occur (e.g., phases 7 and 8). Moisture anomalies are also notable along the subtropical Andes foothills for some MJO phases, especially when meridional transport anomalies are located further east, where opposite signed anomalies to those near the foothills occur. This is the case for phases 7 and 8, showing positive precipitable water and precipitation anomalies along the subtropical Andes, which may be associated with anomalous upslope flow during those phases. Integrated water vapor transport anomaly vectors in both the tropics and subtropics are collocated with wind anomaly vectors at low levels (e.g., 850 hPa, not shown). It is important to note that the spatial coherence of the moisture and precipitation perturbations is not evident at all MJO phases and all parts of the subtropical domain, especially when the meridional moisture transport anomalies are weaker. The precipitation rate and column moisture relationship described in Schiro et al. (2016) is valid in tropical regions only, while in the extratropics a lifting mechanism or a synoptic forcing is often required to overcome a capping inversion.

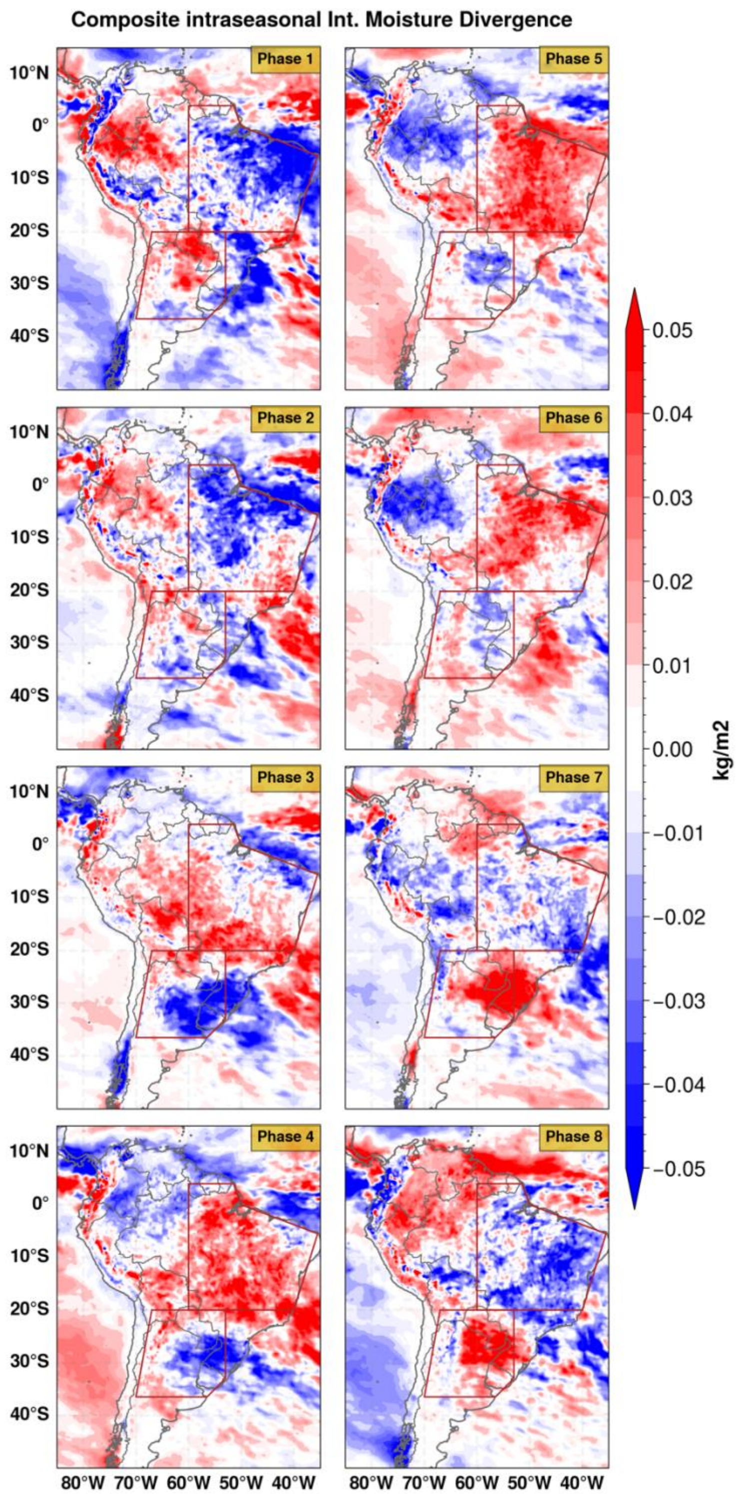

Figure 3.4. Composite maps of austral summer intraseasonal (30-90 days) anomalies of daily-mean vertically-integrated moisture divergence (in kg m^{-2}, shaded), centered over South America. Every panel represents mean conditions observed at each (active) phase of the MJO. Red polygons depict tropical and subtropical South America. Data from ERA5.

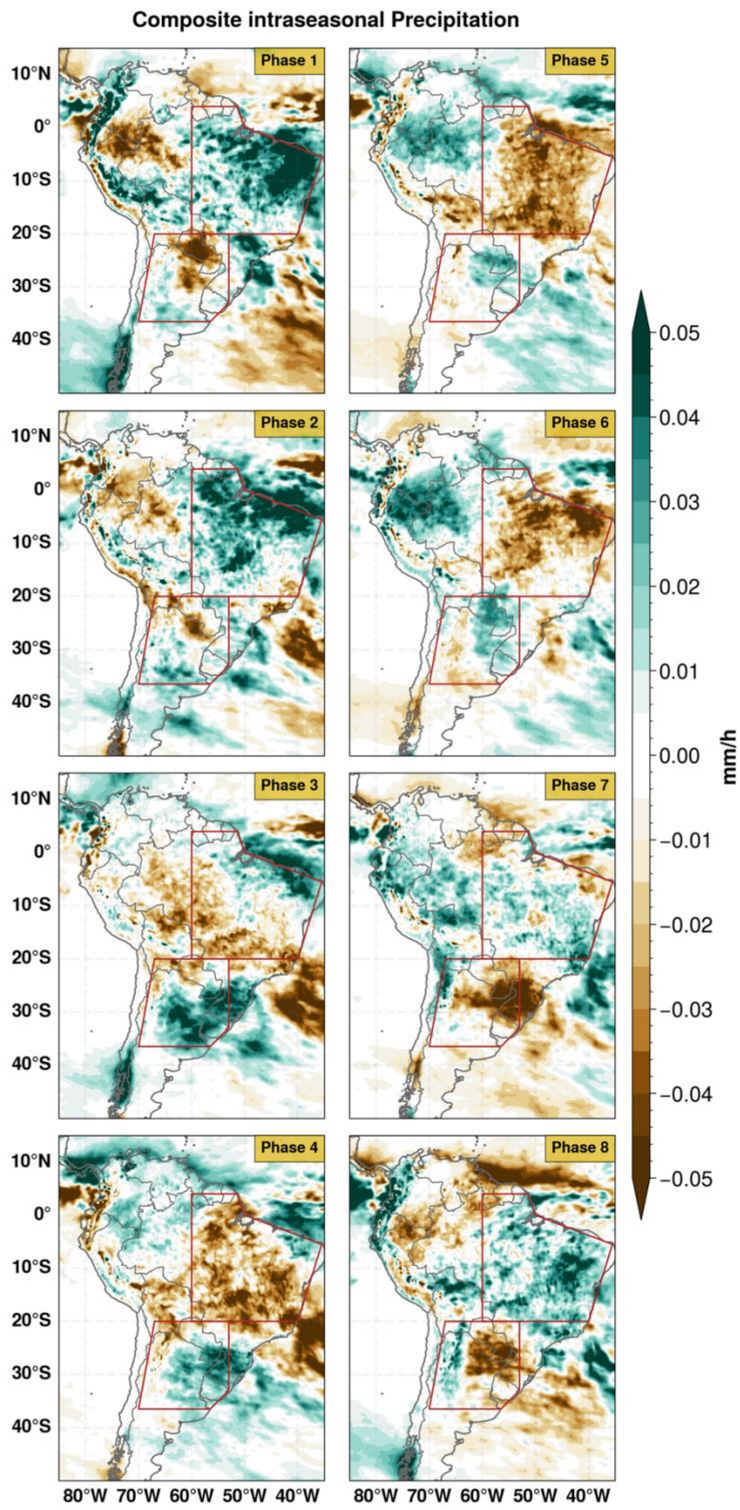

Figure 3.5. As in Figure 3.4 but for precipitation (in mm/h, shaded). Data from ERA5.

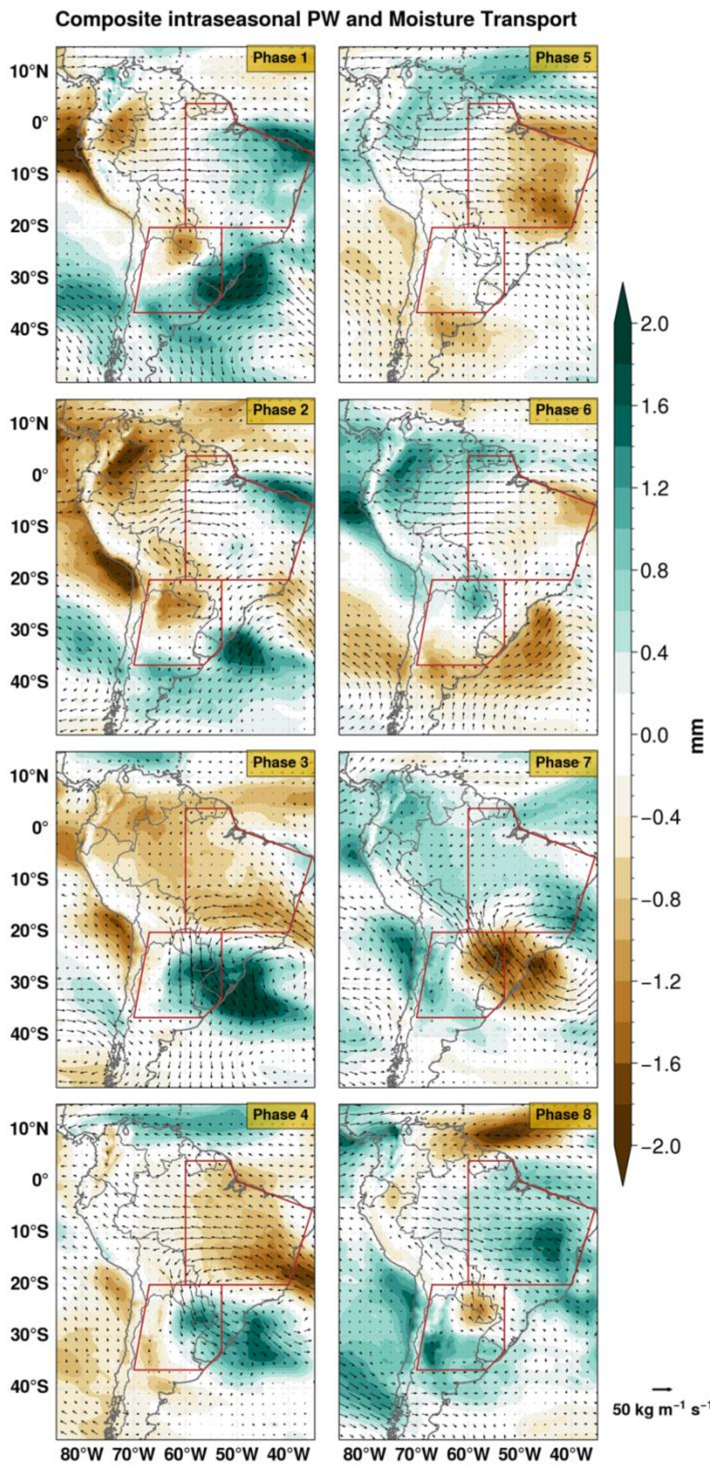

Figure 3.6. As in Figure 3.4 but for precipitable water (in mm, shaded) and integrated water vapor transport (in kg m^{-1} s^{-1}, vectors). Data from ERA5.

Composite maps of convective available potential energy (CAPE) from ERA5 are examined to assess its relationship to convection and precipitation (Figure 3.7). CAPE in ERA5 is computed using the most unstable parcel found below 350 hPa. Unlike previous variables analyzed above, the CAPE – precipitation relationship observed in the tropics is very different from the one in the subtropics. In the tropics, specifically over the Amazon basin, enhanced precipitation generally aligns with lower CAPE, and vice versa. This has been evidenced over the Amazon in previous studies (e.g., Giangrande et al. 2023). Other monsoon land regions such as northern Australia (McBride and Frank 1999) and the Indo-Pacific warm pool region during MJO active and suppressed periods (Virts and Houze 2015) have presented similar relationships , although the sign of this correlation depends on the temporal and spatial scales of the analyzed variables (Tompkins 2001; Subrahmanyam et al. 2015). Over eastern Brazil, however, this negative covariability is not observed, especially since intraseasonal CAPE perturbations seem to be weak there. This could be because the low-level moist static energy over eastern Brazil is lower than in the Amazon basin and its location next to the ocean makes it prone to anomalous low-level moist static energy advection from the Atlantic Ocean, which in turn is induced by low-level zonal wind perturbations (Ma et al. 2011).

In the subtropics, enhanced precipitation is broadly accompanied by positive CAPE anomalies (i.e., positive correlation). However, compared to the Amazon basin, CAPE does not show a consistent covariance with precipitation at every location. This reflects a different CAPE – precipitation relationship in the subtropics, where moisture advection is typically required to both enhance instability and induce precipitation (Rasmussen et al. 2016; Piersante et al. 2021; Sasaki et al. 2022), thus resulting in a positive correlation at daily timescales (Adams and Souza

2009). These existing differences in the CAPE – rainfall relationship between tropics and subtropics have also been observed in global studies (e.g., Zhou et al. 2013).

The differences observed in the modulation of convective environments across South America deserve closer inspection, especially in the context of how they could influence storm characteristics. In the next section, an analysis of the three-dimensional structure of precipitating cloud systems will be conducted to evaluate whether an MJO modulation can be observed at the mesoscale and near storm environment, and how these potential modulations connect with the regional features analyzed above.

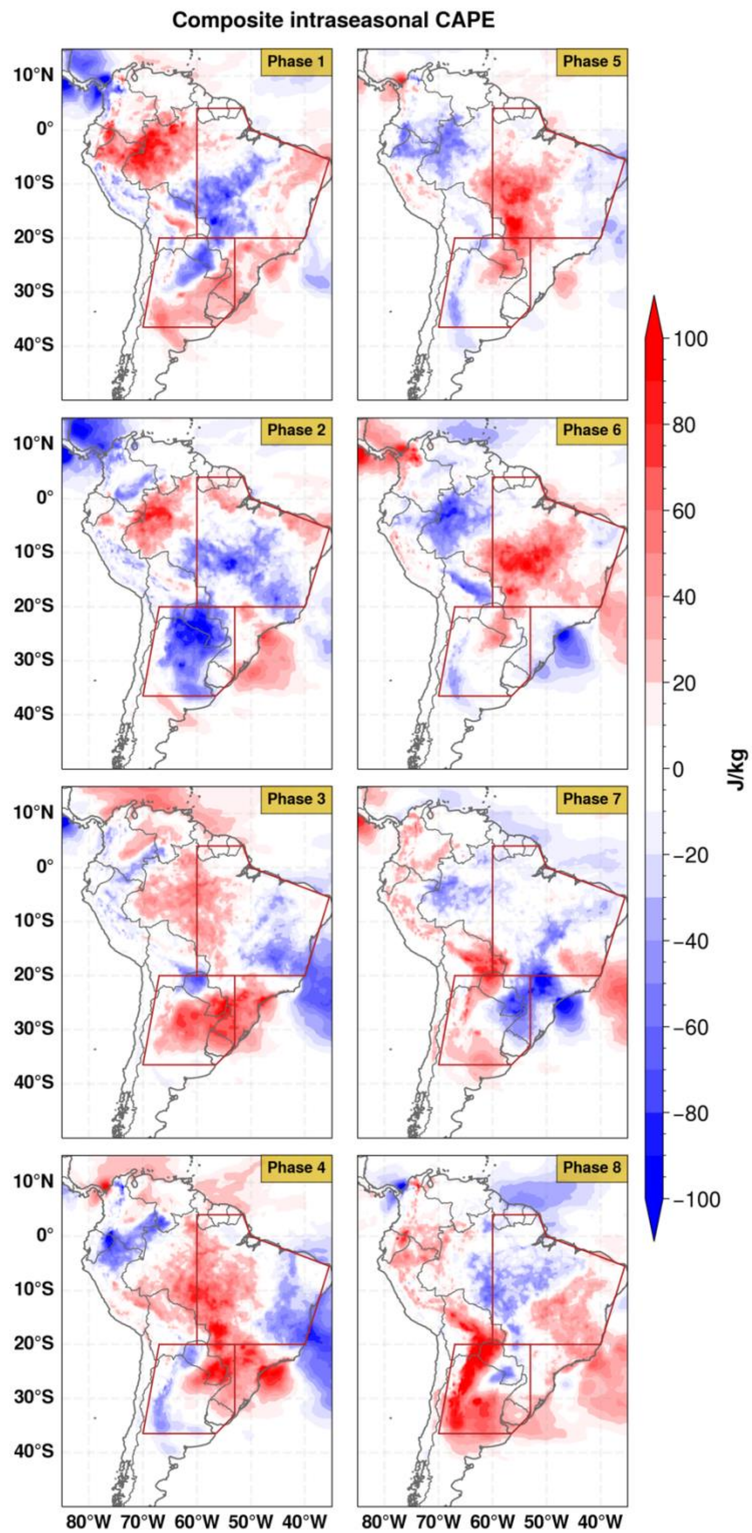

Figure 3.7. As in Figure 3.4 but for convective available potential energy (in J/kg, shaded). Data from ERA5.

3.3.3 Modulation of storm characteristics in the tropics

Figure 3.8 shows composite values as a function of MJO phase for the three different storm features described in Chapter 3.3.2. To produce this figure, characteristics from all individual PFs observed by TRMM over eastern tropical South America (in the area enclosed in Figure 3.1) when the MJO was active in each respective phase were averaged. VOLR and AREA vary together, which is expected given that the total precipitation from a storm is often related to its horizontal extent (Rasmussen et al. 2016; Prein et al. 2017). VOLR ranges from about 2940 km^2 mm h^{-1} in phase 4 to 3715 km^2 mm h^{-1} in phase 1 (range is ~33% of the mean value), while for AREA it ranges between 805 km^2 in phase 4 and 1060 km^2 in phase 1 (~27% of the mean value). However, MXHT40 shows an almost perfect out of phase relationship with VOLR and AREA. This implies that in phases where the MJO enhances volumetric rain and the area of individual storm features, below-average storm vertical extent is observed, while phases with suppressed storm area and precipitation show above-average storm vertical extent. This height parameter ranges from 0.94 km (phase 1) to 1.18 km (phase 4), representing a ~23% of the mean value.

Phases featuring storms with enhanced VOLR and larger AREA in the central and eastern tropics (phases 1, 8, and to a lesser extent 2 and 7) correspond to phases where westerly moisture transport anomalies, large-scale upward motion, and enhanced daily precipitation accumulations are generally observed (Figures 3.4 – 3.6). This is especially evident in phases 1 and 8, where precipitation and moisture anomalies are strongest at both regional and storm scales. Conversely, MXHT40 presents the smallest values for phases 7, 8, and 1, consistent with negative CAPE anomalies obtained by averaging CAPE from the closest grid point to each individual PF (not shown). Previous studies have associated a westerly wind regime across the South American tropics with similar environmental conditions to those described here; the storms under this regime tend to present significantly larger spatial extent and lower vertical development, based on ground-based observations in the central tropics (Rickenbach et al. 2002; Williams et al. 2002). The western tropics tend to present an opposite modulation in precipitation, moisture, and instability than the central and eastern tropics, although the average modulation of storm features does not present a significant signal that is worthy of further exploration (not shown). Therefore, atmospheric conditions under phases 8 and 1, and to a limited extent 2 and 7, favor storms that tend to be wider and shallower, which is a feature frequently observed for storms with enhanced large-scale precipitation in other tropical regions (e.g., Panasawatwong et al. 2022).

Phases showing suppressed VOLR and reduced AREA in the central and eastern tropics (phases 3, 4, and 5) are associated with predominantly easterly integrated moisture transport anomalies across the region, a drier atmosphere, anomalous large-scale downward motion, and reduced daily precipitation accumulation (Figures 3.4 – 3.6). MXHT40 is enhanced for the same MJO phases. This result is consistent with storm heights being greater during periods of prevailing enhanced CAPE – obtained by averaging CAPE from the closest grid point to each individual PF (not shown) – and reduced precipitable water over most of central and eastern Brazil (e.g., Figure 3.6), favoring storms that are deeper and more isolated in nature. In fact, other studies have shown that this storm mode predominates in the central tropics of South America when an easterly wind regime favoring similar environmental conditions to those observed for phases 3 - 5 is in place (Rickenbach et al. 2002; Williams et al. 2002). Opposite signed anomalies are again observed in western tropics from the regional maps (Figures 3.4 – 3.7), especially for phases 4, and 5, but a significant mean storm modulation across that region is less clear (not shown).

Additional insight at the storm scale can be extracted from mean vertical profiles of temperature and moisture obtained from ERA5 for every individual PF using the closest grid point to the core of the object. It is important to acknowledge that the closest grid point approach might not fully represent the PF's surrounding environment (e.g., due to convection contamination), however, previous studies over South America have shown negligible differences in the ERA5 convective environments between a closest grid point approach and a mean multigrid average surrounding a storm center (Chapter 2.2.2). Therefore, for simplicity we selected the vertical profile that is closest to each individual PF core. Figure 3.9 shows the composite vertical profile anomalies as a function of MJO phase for air temperature and specific humidity. Phases with enhanced precipitation over the eastern tropics (8, 1, and 2) tend to have weaker lapse rates due to warmer anomalies aloft and cooler boundary layer temperatures, while phases favoring deeper storms (3, 4, and 5) show colder anomalies aloft, warmer boundary layer temperatures, and steeper lapse rates. Differences in moisture anomalies across phases are particularly robust. Phases with enhanced rainfall accumulation generally show increased moisture in the atmospheric column (especially in phases 8 and 1), while phases with reduced rainfall accumulation correspond to a drier troposphere at all levels (especially for phases 3, 4, and 5). This relationship between precipitation and column moisture anomalies is consistent with previous studies (Holloway and Neelin 2009; Schiro et al. 2016). Differences between opposite MJO phases are nearly symmetric in the vertical for some phases, and especially notable at mid-levels (450 - 600 hPa), where differences can exceed 0.5 g/kg between phases 1 and 5. These differences can have implications in the convective environment where storms are taking place, as convection is known to be susceptible to entrainment of moist/dry air at mid-levels (Holloway and Neelin 2009; Schiro et al. 2016).

The lapse rate and moisture anomalies described above are expected to influence CAPE (Tuckman and Emanuel 2024) While the tropospheric moisture modulation alone does not seem to explain the CAPE modulation in Figure 3.7 (e.g., low-level drying in phases 3-5 would reduce instability rather than increasing it), the observed the lapse rate anomalies are generally consistent with the corresponding CAPE perturbations over central tropics for most of the MJO phases discussed above (Figure 3.7). A more consistent correspondence between lapse rates and CAPE arises when the MJO modulation of CAPE is computed by extracting ERA5 CAPE from the closest grid point to each PF center: significantly enhanced CAPE during phases 3, 4, and 5, and reduced CAPE for phases 8 and 1 (not shown). Therefore, for the different storm modes over the area of study, anomalously steeper lapse rates are observed when deeper and narrower storms predominate, and smaller lapse rates are present when storms are mainly wider and shallower. While moisture perturbations (Figure 3.9b) can also affect CAPE, they appear to play a secondary role in modulating instability over the region, with opposite signed anomalies at low-levels that would be expected to have an opposite effect on CAPE. The predominant role of lapse rate changes in inducing CAPE changes have been evidenced in previous studies (Chen et al. 2020a).

In addition, MJO modulation of the two predominant storm modes in tropical South America is consistent with the “rains” and “showers” regimes described by Raymond et al. (2024) from simultaneous observations in various locations in the tropical east Pacific. Previously, similar precipitation regimes were observed over northern Australia (Williams et al. 1992) and with in-situ measurements over the Eastern Pacific Intertropical Convergence Zone (ITCZ) (Petersen et al. 2003). The “rains” regime consists of extended periods with weaker but widespread precipitation that produce greater rainfall accumulation associated with very moist and more stable environments. This is characteristic of the environment and storm modes in central and eastern tropical South America during MJO phases 7, 8, 1, and 2. The “showers” regime corresponds with more episodic and isolated but intense convection that produces lower rainfall accumulation, coinciding with drier and highly unstable environments similar to MJO phases 3, 4, and 5 across the same region.

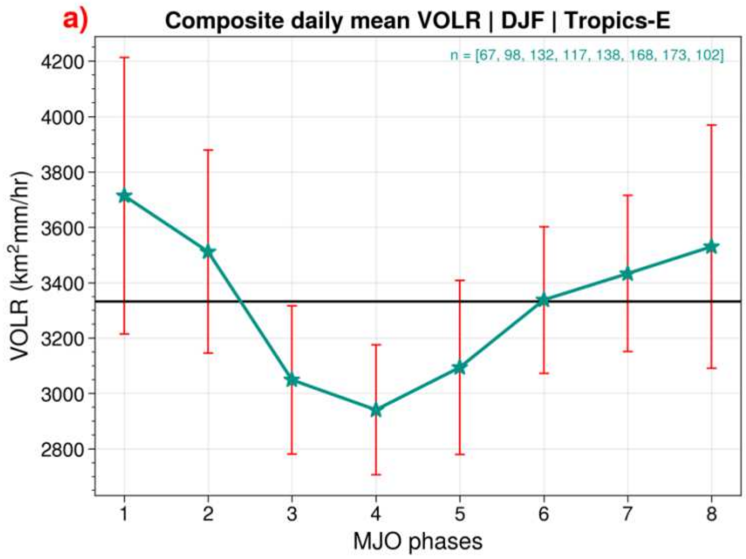

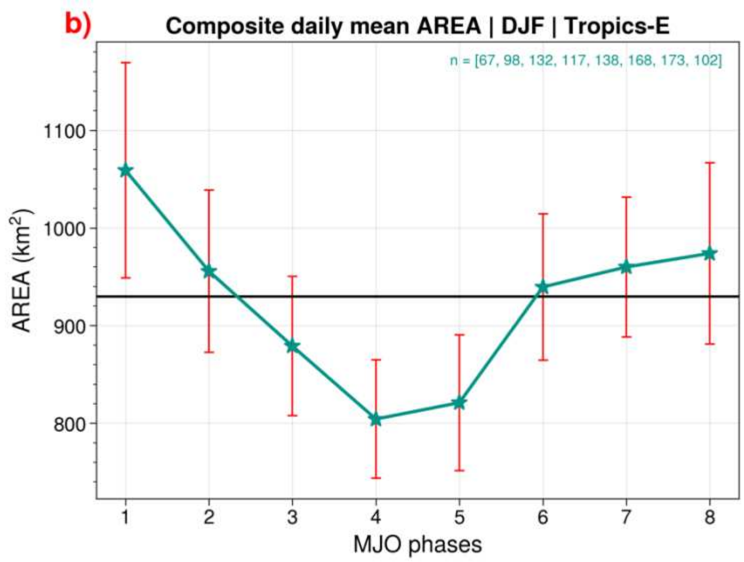

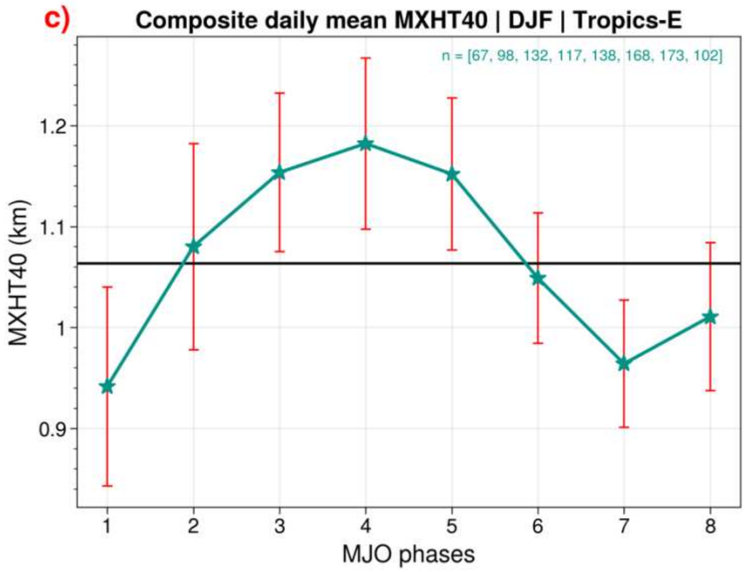

Figure 3.8. Mean distribution of (a) Volumetric rain rate, (b) Total area containing precipitating pixels, and (c) Maximum height of 40 dBZ echo, from all the PFs identified under each phase of the MJO, in tropical South America (see Figure 3.1). Error bars represent a 95% t-test confidence interval, using as degrees of freedom (n) the total number of MJO days per phase shown in the respective figure's top right.

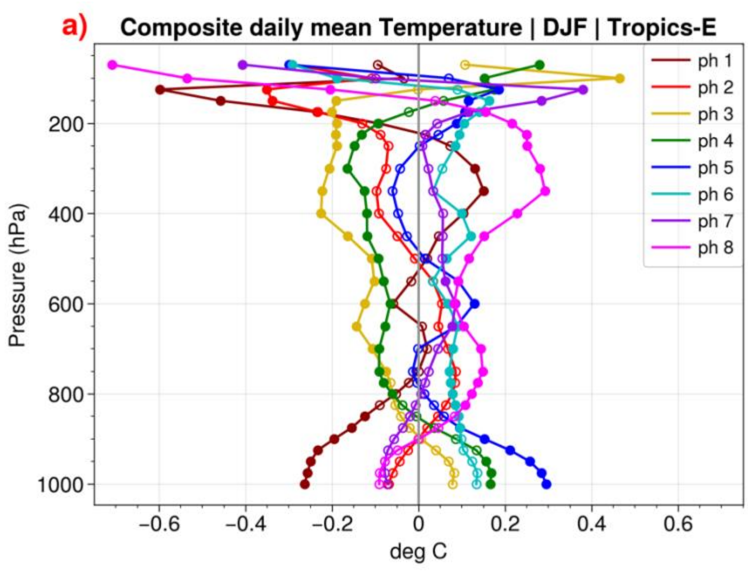

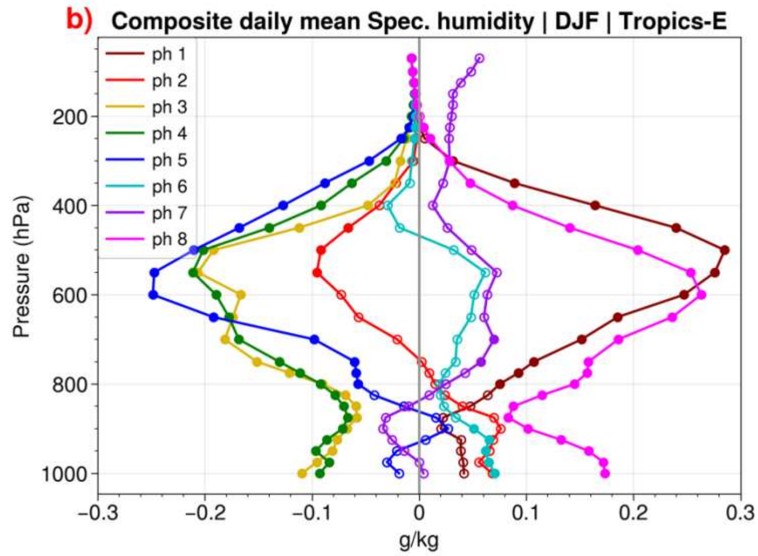

Figure 3.9. Composite anomalies in the vertical profiles of (a) temperature (ºC) and (b) specific humidity (g/kg), as a function of the MJO phases. The vertical profiles corresponding to the closest grid point of every individual PF observed during a specific MJO phase were averaged (after removing the mean profiles across the eight phases) and shown here. Values that are significantly different from zero at 90% confidence at every pressure level are represented with solid circles, based on a t-test using the total number of MJO days per phase as degrees of freedom.

3.3.4 Modulation of storm characteristics in the subtropics

For subtropical South America, an MJO modulation of storm modes appears to be less evident than in tropical South America. Figure 3.10 shows that a strong positive relationship between volumetric rain rate and storm horizontal extent also generally occurs, but covariability between these parameters and storm vertical extent is not consistent across the MJO cycle, unlike in the tropics. Additionally, the evolution of these parameters across MJO phases is not very smooth, with larger overlapping confidence levels compared to what is observed in the tropics. These differences may be caused by a larger variability in the nature of convection observed at sub-seasonal scales across the subtropics, including from synoptic-scale weather features (Garreaud and Wallace 1998; Rasmussen et al. 2016; Bruick et al. 2019). Despite the overall weaker modulation, a few interesting signals deserve some attention. Volumetric rain rate varies from 9,000 km^2 mm h^{-1} in phase 3 to 6,300 km^2 mm h^{-1} in phase 6, representing a ~36% variation relative to the mean. Phase 6 depicts shallower, smaller, and lower precipitation storms, while phases 8 and 1 show a significantly positive storm height anomaly.

Figure 3.11 provides some information about the storm environment to put Figure 3.10 results in context. For phase 3, the environment is on average slightly colder with weak positive moisture anomalies at low-levels, although these anomalies are not significant. In Phase 6, the middle tropospheric anomalies are warmer and wetter than surface levels. Lapse rates are smaller, which favors the inhibition of deeper convection (CAPE anomalies in the subtropics are slightly negative overall, according to Figure 3.7). The storm modulation and the associated environment are consistent with weak convection being predominant under this phase. For phases 8 and 1, the temperature profiles show a strong increase in boundary layer temperatures that maximize near the surface, indicating anomalously high lapse rates for storms under these phases. This supports favorable conditions for strong buoyancy and updrafts (i.e., strong CAPE) that cause the large MXHT40 values observed. This matches the enhanced CAPE observed in Figure 3.7 across the Andes foothills for phases 8 and (to a lesser extent) 1, suggesting that the storms adjacent to the Andes could grow deeper under these phases.

While tropical convective activity is modulated by the large-scale MJO tropical wind component, in the subtropics the storm scale modulation by the MJO appears to be broadly associated with variations in the SALLJ. Table 1 presents the mean meridional 850 hPa winds per MJO phase, averaged over the light blue box defining the SALLJ region in Figure 3.1. The modulation of the meridional winds associated with the SALLJ resembles the signal shown in Figure 3.10 for AREA and VOLR, and is consistent with the moisture transport anomalies shown in Figure 6 in the subtropics. The phases that show the largest enhancement in volumetric rain rate

(Phases 2 and 3) generally correspond to when the northerly winds are strongest (Table 3.1), and moisture transport anomalies bring moisture into the Argentine plains from the tropics (except phase 4). The phases with the deepest storms on average (8 and 1) correspond to the weakest SALLJ (Table 3.1) and moisture advection into the subtropics (Figure 3.6), causing dry anomalies over the northern plains (Figure 3.6). A weak SALLJ would limit significant wind shear in the subtropics, so having high instability without wind shear would favor isolated and short-lived storms (Weisman and Klemp 1982; Miller and Mote 2017). Therefore, despite not showing a clear storm mode modulation, the MJO may modulate aspects of midlatitude storm features by inducing changes in the positioning and strength of the SALLJ through its influence on large-scale pressure anomaly patterns.

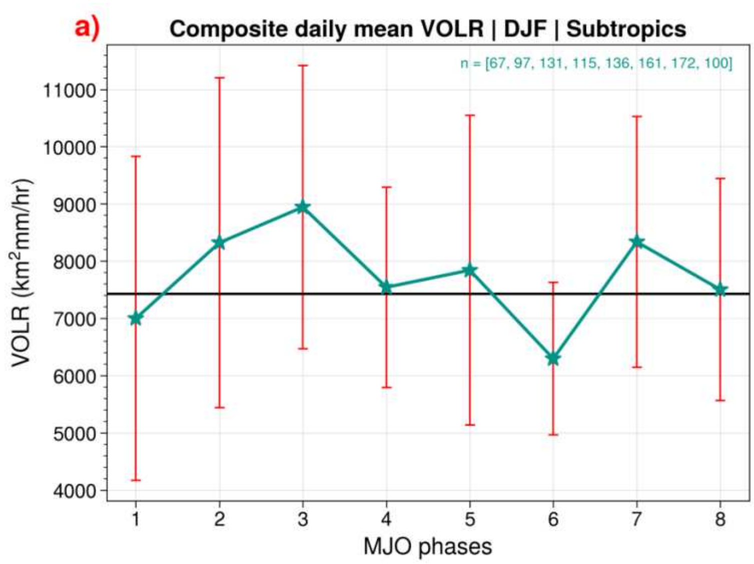

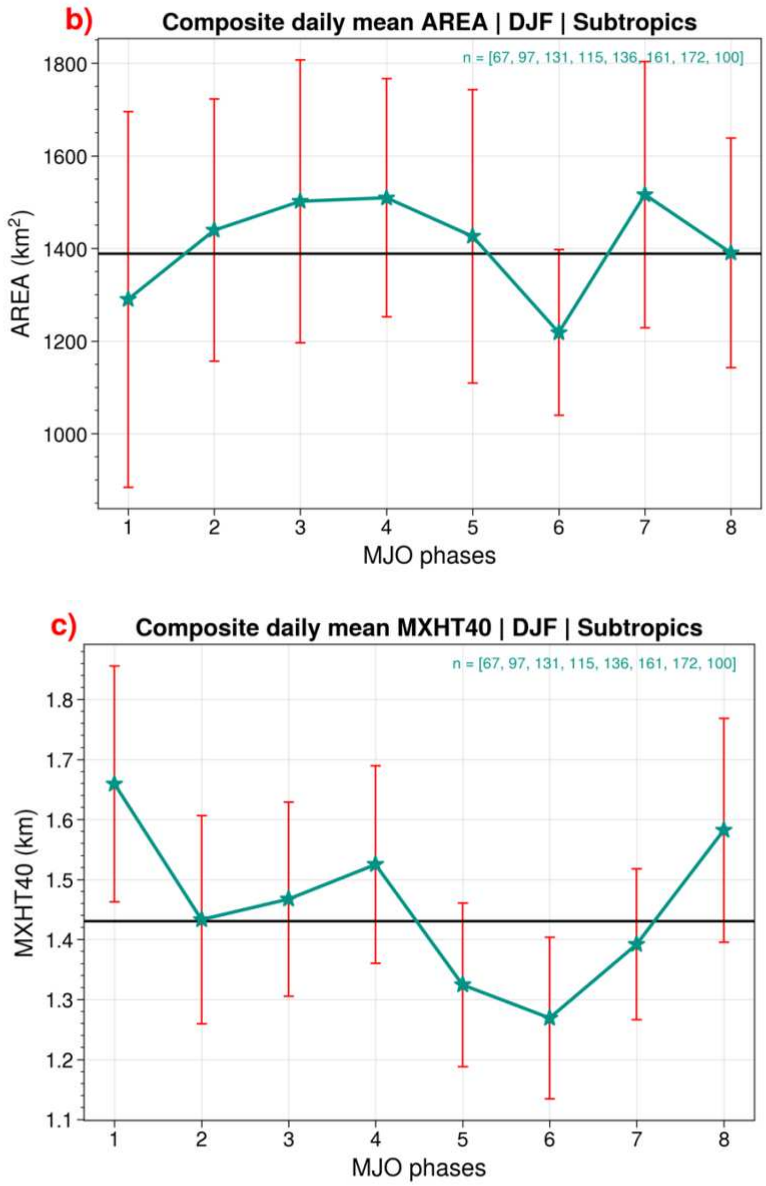

Figure 3.10. As in Figure 3.8, but for the subtropical area shown in Figure 3.1.

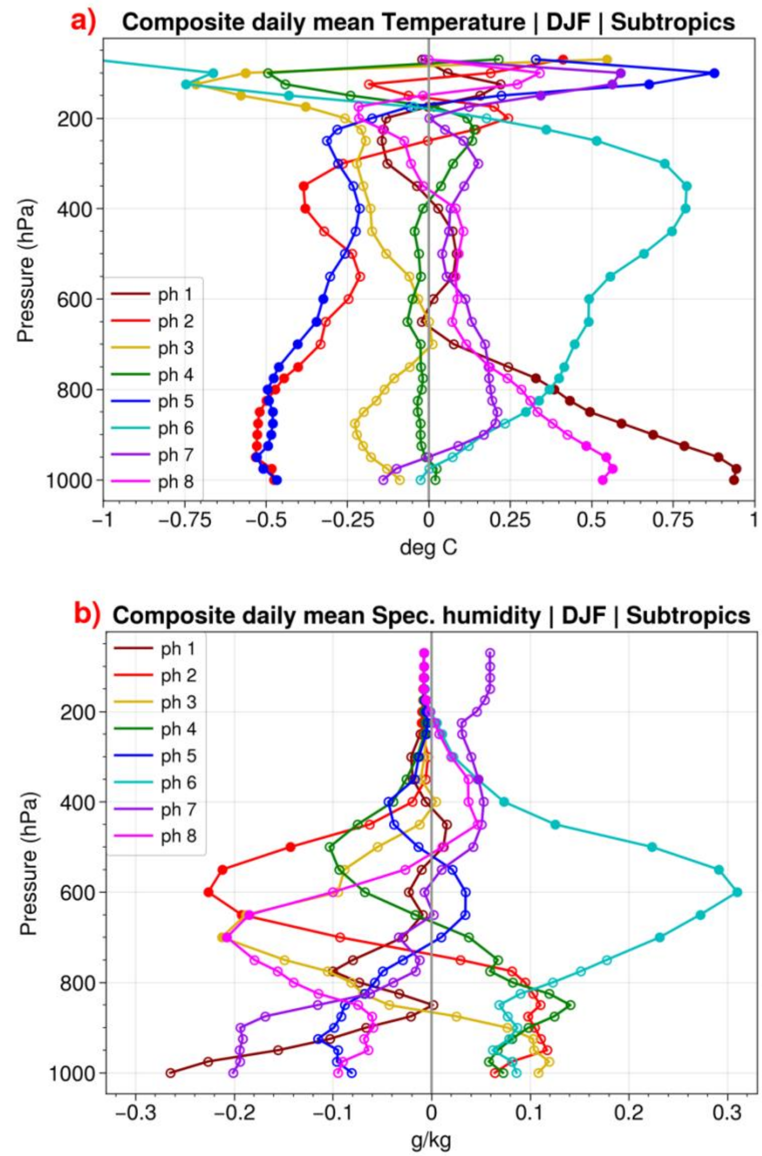

Figure 3.11. As in Figure 3.9, but for the subtropical area shown in Figure 3.1.

MJO phase	1	**2**	**3**	**4**	5	6	**7**	8
Northerly wind at 850 hPa (m/s)	1.2	**2.5**	**2.7**	**3.1**	2.0	1.7	**2.4**	0.6

Table 3.1. Absolute mean of austral summer 850 hPa meridional wind over the light blue box (20-30S, 65-58W) shown in Figure 3.1, as a function of MJO phase. This is used as a proxy for the

South American Low-Level Jet strength. Values were multiplied by −1 to represent northerly winds. The phases with the largest wind intensity are bolded. Data from ERA5.

3.4 Summary

The present study analyzes the influence of the Madden Julian Oscillation (MJO) on intraseasonal variability in convective storms in the tropics and subtropics of South America during austral summer. MJO activity is defined using the Real-time Multivariate MJO index (RMM), and the large-scale environment during different phases of the MJO lifecycle is analyzed using daily-mean ERA5 reanalysis data. Convective storms in South America are characterized by using the Precipitation Feature (PF) database from the Tropical Rainfall Measuring Mission satellite. This database uses three-dimensional precipitation radar observations to identify individual storms and provides several storm intensity-related metrics. Three main storm features describing storm horizontal and vertical extent and areal rainfall are used to summarize the MJO modulation at the storm scale. The main findings are summarized below:

- The MJO wind anomaly response to MJO heating anomalies in the west Pacific propagates eastward through the equatorial waveguide and modifies the large-scale environment in tropical South America. Phases 8 and 1 support periods of widespread large-scale upward motion anomalies over the central and eastern tropics of South America that initiate positive precipitable water and westerly moisture transport anomalies, which are associated with enhanced precipitation anomalies. The opposite occurs in the same region during phases 4 and 5, with downward motion anomalies, reduced atmospheric moisture, anomalous easterly moisture transport, and suppressed precipitation.
- The western tropics adjacent to the east slopes of the Andes exhibit opposite-signed MJO-related anomalies to the rest of tropical South America for atmospheric variables such as precipitable water, precipitation, and convective instability.

- A significant modulation of storm mode characteristics is observed in central and eastern tropical South America. Phases 8 and 1 favor days with wider and shallower storms that produce larger accumulated volumetric rain, which develop in an enhanced moisture and reduced instability environment (in association with steeper lapse rates). Other adjacent phases (2 and 7) inducing similar (but weaker) large-scale environments also coincide with predominantly shallower storms, but the signal is weaker. These storm structures and their associated environments resemble the “rains” regime described by Raymond et al. (2024). Storms during phases 3, 4, and 5 depict an opposite storm mode modulation, characterized by deeper and narrower storm structures that accumulate less rain per storm on average. The environment in which these storms grow is drier and more unstable (in association with smaller lapse rates), consistent with the “showers” regime (Raymond et al. 2024).
- MJO tropical-extratropical teleconnections also influence the large-scale environment in the subtropics via Rossby wave propagation through midlatitudes from the west Pacific. Precipitation and vertical motion anomalies in the subtropics are typically opposite signed to those in central and eastern tropics. East of the subtropical Andes, phases 7, 8, and 1 are associated with enhanced moisture divergence and a weaker SALLJ, which causes a reduction in moisture, thereby suppressing precipitation. Conversely, phases 3, 4, and 5 are associated with enhanced moisture convergence and a strengthened SALLJ, which translates into increased moisture values, thus enhancing precipitation over the region.
- In the subtropics, although extratropical teleconnections (Figure 3.2) alter the regional environment, including the positioning and strength of the South American low-level jet (SALLJ, Table 1), the modulation of storm modes by the MJO is less clear. The modulation of the storm vertical and horizontal structures broadly follows the anomalies of the

meridional low-level winds and associated moisture transport in the northern plains (where the SALLJ exerts its influence). However, given the larger variance in storm characteristics in this region, the storm mode modulation exerted by the MJO in the subtropics is less robust than in the tropics.

Most studies exploring the MJO modulation in convective storms over South America have described its influence in associated daily precipitation accumulation (Carvalho et al. 2004; Barrett et al. 2012; Alvarez et al. 2016; Grimm 2019; Mayta et al. 2019; Rondanelli et al. 2019; Recalde-Coronel et al. 2020) or severe storm occurrence (Barrett et al. 2020; Veloso-Aguila et al. 2024). This study is the first attempt (to our knowledge) to show how the direct and remote influences of the MJO modulate individual storm structures, which inherently occur at sub daily timescales.

The results of this study may contribute to improving the predictability of preferred storm modes up to several weeks in advance, thanks to recent progress in MJO prediction skill (Kim et al. 2018). Certain storm modes enhance the likelihood of severe weather events, such as increased chances of severe impacts from deep isolated storms under dry and unstable environments or flooding risk associated with wide mesoscale convective systems under wetter environments (Zhang 2013). Anticipating storm type and occurrence will aid decision makers and emergency services in warning populations about these different threats, especially in highly vulnerable regions such as the Amazon rainforest.

CHAPTER 4

Shifting Storm Modes: Projecting the Future of Extreme Convection in South America using Convection Permitting Climate Simulations

4.1 Introduction

Convective storms are a key component of the Earth's climate system, producing a significant fraction of global precipitation, and are often associated with severe weather, including flash floods, large hail, and strong winds. While convection is a global phenomenon, its nature is strongly modulated by geographical characteristics. South America, with its considerable meridional extent (12ºN-55ºS) and unique regional features such as the Amazon tropical rainforest and complex topography dominated by the Andes Mountains, is a natural laboratory for studying some of the planet's most intense convective storms (Zipser et al. 2006; Cecil and Blankenship 2012).

Precipitation events exhibit significant variability in frequency and intensity across the globe. While some regions experience frequent but light precipitation, others are characterized by short-lived but intense showers (Schumacher and Houze 2003). South America displays a wide spectrum of precipitation regimes (Ferreira and Reboita 2022). The Amazon Basin receives abundant year-round rainfall from diurnally forced isolated convection, whereas the subtropical plains east of the Andes experience a pronounced seasonal cycle, with much of the warm-season precipitation delivered by large mesoscale convective systems (Velasco and Fritsch 1987; Salio et al. 2007; Rasmussen et al. 2016). In this region, precipitation events are often less frequent but very intense, contributing substantially to annual rainfall accumulation and posing significant socioeconomic risks (Rasmussen et al. 2016)

The mode of convective organization strongly influences precipitation characteristics and the potential for high-impact weather. The TRMM-heritage storm mode classification (Houze et al. 2015) has allowed the identification of extreme precipitating systems representing different stages of a storm's lifecycle around the global tropics and subtropics by using three-dimensional reflectivity data. In South America, storm modes have been predominantly studied in the subtropical plains and the Amazon rainforest (Romatschke and Houze 2010; Rasmussen and Houze 2011; Rasmussen et al. 2014; Houze et al. 2015; Rasmussen et al. 2016). In the Amazon, the nature of convection resembles a maritime environment, with predominantly moderate convective systems. In the subtropics, extremely intense convection can occur, which can induce the occurrence of severe thunderstorms (Rasmussen et al. 2014; Veloso-Aguila et al. 2024; Salio et al. 2024).

Global warming is altering the global water cycle and, consequently, precipitation patterns (Douville et al. 2021). The Clausius-Clapeyron relationship dictates that a warmer atmosphere can hold more water vapor (~7% per degree Celsius of warming), which is expected to lead to an intensification of extreme precipitation events (Trenberth et al. 2003; Held and Soden 2006). Climate model projections consistently show an increase in the intensity of heavy rainfall in a warmer climate (Douville et al. 2021), with the greatest increases for subdaily precipitation events (Westra et al. 2014). For South America, while there is general agreement on future warming, projections of mean precipitation changes show significant regional variability and model uncertainty, with most models suggesting wetting of the subtropics and a reduction in precipitation frequency over most of the Amazon (Pascale et al. 2019; Reboita et al. 2022a; Kahana et al. 2024). Beyond changes in precipitation frequency and intensity, understanding future shifts in extreme events is paramount for climate adaptation. Coarse-resolution global climate models (GCMs) cannot explicitly resolve convective processes and the detailed structure of storm systems (Prein et al. 2015). While some efforts have been made to increase the horizontal resolution of climate projections in South America by downscaling GCMs with regional climate models (e.g., Reboita et al. 2022), the need for a better representation of storm structure changes calls for the utilization of convection-permitting climate models over South America. Fortunately, the first efforts to conduct such simulations were initiated by the South America Affinity Group (SAAG) with two long-term present and future climate simulations at a convection-permitting resolution of 4-km (Dominguez et al. 2024).

In the present study, a climatological analysis of austral summer precipitation and extreme storm structure distribution, frequency, and intensity is conducted over South America, based on the SAAG 22-year convection permitting present climate simulation. Future changes in precipitation and precipitating storm structures are assessed by contrasting the SAAG control simulation with the SAAG future climate simulation that uses the pseudo global warming (PGW) approach.

4.2 Data and methods

4.2.1 Model data

The Weather Research and Forecast (WRF) Model version 4.1.5 (Skamarock et al. 2019) was run by the South America Affinity Group (SAAG, Dominguez et al. 2024) to simulate long-term South America's climate at storm resolving scales. The model setup corresponds to a domain of 1,472 × 2,028 grid points covering the entire South American continent and surrounding ocean waters (Figure 4.1), with 4-km horizontal grid spacing and 61 vertical levels. The boundary and initial conditions are represented by ERA5 reanalysis data (Hersbach et al. 2020). Present climate conditions are represented by a 22-year control simulation (SAAG-CTL), covering the period from January 2000 to December 2021. A 22-year future climate simulation was run using a pseudo global warming (PGW) approach (SAAG-PGW, Schär et al. 1996). This approach adds a climate change perturbation to the environmental conditions used for SAAG-CTL to simulate a future climate scenario. In this case, this signal comes from the LENS2 monthly mean 100-member ensemble mean of climate change projections from the Community Earth System Model version 2 (CESM2), using the projected scenario SSP3-7.0 for 2060-2080. Further explanation of the computation and setup of both simulations can be found in Dominguez et al. (2024).

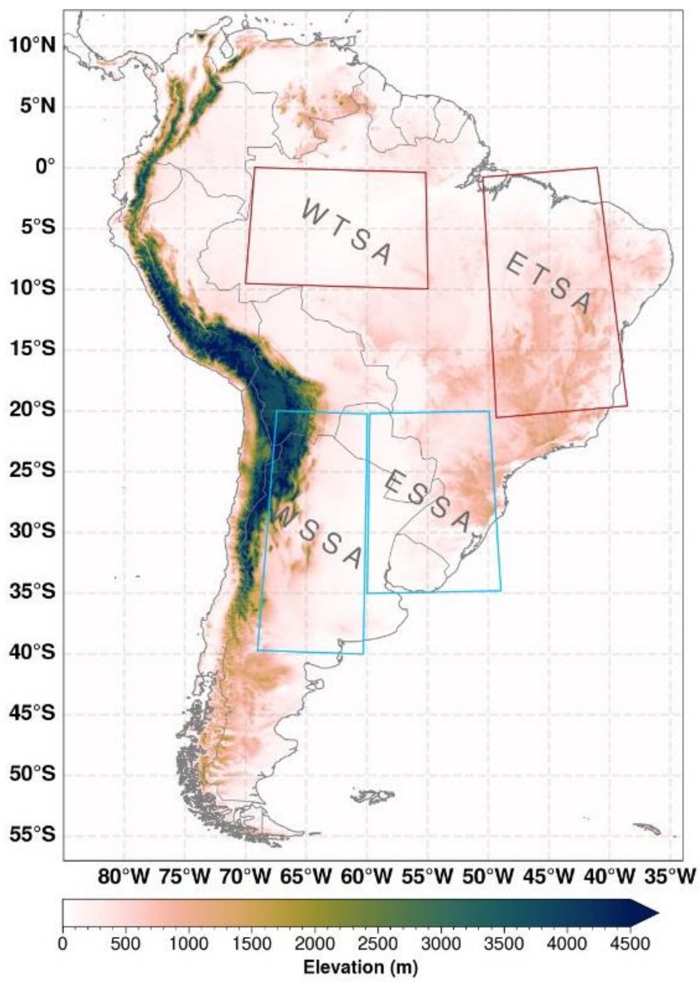

Figure 4.1. Map of the study region (South America) showing terrain elevation as represented by the WRF simulation. Different subregional boxes are selected across tropical and subtropical South America for the analyses shown in the results section (Chapter 4.4). See Chapter 4.2 for additional details.

4.2.2 Satellite data

The Global Precipitation Measurement (GPM) dual-frequency precipitation radar (DPR) (Hou et al. 2014) is utilized as ground truth to evaluate SAAG-CTL performance in reproducing climatological features of precipitation and convective storms over South America. In particular, we use interpolated GPM Ku-band three-dimensional reflectivity data from the University of Washington (accessible here https://gpm.atmos.washington.edu/), covering the period December 2014 – February 2025 at 0.05º horizontal grid spacing. Since the satellite overpasses across the global tropics and extratropics are not regular in time and space, we use a spatial field containing the total count of satellite overpasses in each grid point to normalize the frequency maps shown in the results section (Chapter 4.3).

4.2.3 Storm mode identification

GPM spaceborne reflectivity observations and WRF simulated reflectivity data are utilized as input for a convective-stratiform mask algorithm that identifies convective or stratiform radar echoes according to different reflectivity intensity criteria (Houze et al. 2015). This convective-stratiform mask is subsequently used as input for an algorithm that identifies storm echo objects representing different storm structures, based on a combination of reflectivity intensity, height, and horizontal extent. In this study, we focus on four different storm modes: Deep Convective Cores (DCCs), Wide Convective Cores (WCCs), Deep and Wide Convective Cores (DWCCs), and Broad Stratiform Regions (BSRs). The specific criteria used to identify these storm modes can be seen in Figure 4.2. In this study, storms are identified using the moderate intensity thresholds.

For each storm mode identified in South America, we conduct subregional analysis focused on four regions of interest shown in Figure 4.1: Western Tropical South America (WTSA), Eastern Tropical South America (ETSA), Western Subtropical South America (WSSA), and Eastern Subtropical South America (ESSA). In each subregion, a tracking algorithm (Hudson and Maloney 2023) is utilized to identify every individual storm having independent contiguous grid points every three hours. This allows storm-centered analysis where different storm characteristics can be extracted, which is not possible from the fixed grid point perspective. For this study, temporal tracking is not considered. For each individual storm identified in each subregion, different storm features are extracted: maximum reflectivity (*maxdbz*), height at which such reflectivity is observed (*maxdbzh*), echo top height of 0 and 40 dBZ (mxht00 and mxht40), storm area (*km2*), volumetric rain rate (*VOLR*), maximum rain rate (*maxRR*), maximum updraft (*maxW*), maximum updraft helicity (*maxUHEL*), and total number of storms identified within the subregion (*n_storms*). The domain-average storm feature conditions for each storm mode are computed at each timestep.

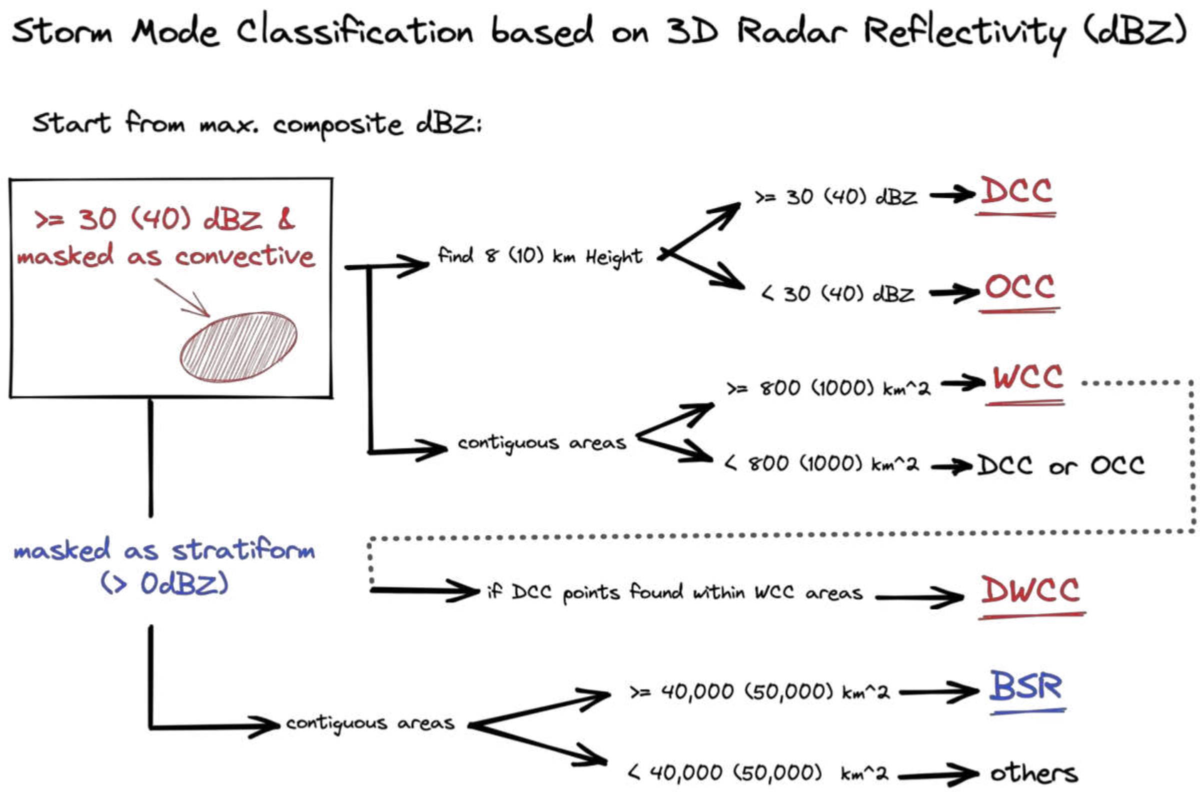

Figure 2. Flowchart with the criteria used to define different storm modes using moderate (strong) intensity thresholds. DCC: deep convective core; OCC: ordinary convective core; WCC: wide convective core; DWCC: deep and wide convective core; BSR: broad stratiform region. From Yu (2022).

4.3 SAAG model performance

4.3.1 Rain climatology

Figure 4.3 shows the model representation of rainfall frequency across South America and how it compares to GPM observed precipitation events. Given the non-continuous satellite temporal and spatial overpass frequency, the frequency of precipitation is shown as the probability of observing a rain event (> ~0.1 mm/h) at each grid point. This is obtained by counting all the instances where rain was identified at a certain pixel divided by the total number of times GPM overpassed that location. The observed frequency of rain events in summer (Figure 4.3a) shows a higher frequency of rain over the deep tropics (over 14% of the time), extending eastward into the climatological position of the South Atlantic Convergence Zone (SACZ), in comparison to lower frequencies over subtropical South America (under 8% of the time). Other areas with enhanced rainfall frequency are western Patagonia, portions of the tropical Andes' eastern slopes, and the Pacific/Atlantic ITCZ region. The simulated frequency of rain events (Figure 4.3b) captures well the observed spatial distribution from GPM, showing a higher probability of rain over the Amazon basin compared to the subtropics. WRF also well represents the enhanced frequencies over the ITCZ region, the Peruvian tropical Andes, and western Patagonia. However, there is an apparent overrepresentation of rain events over the western slopes of the tropical Andes.

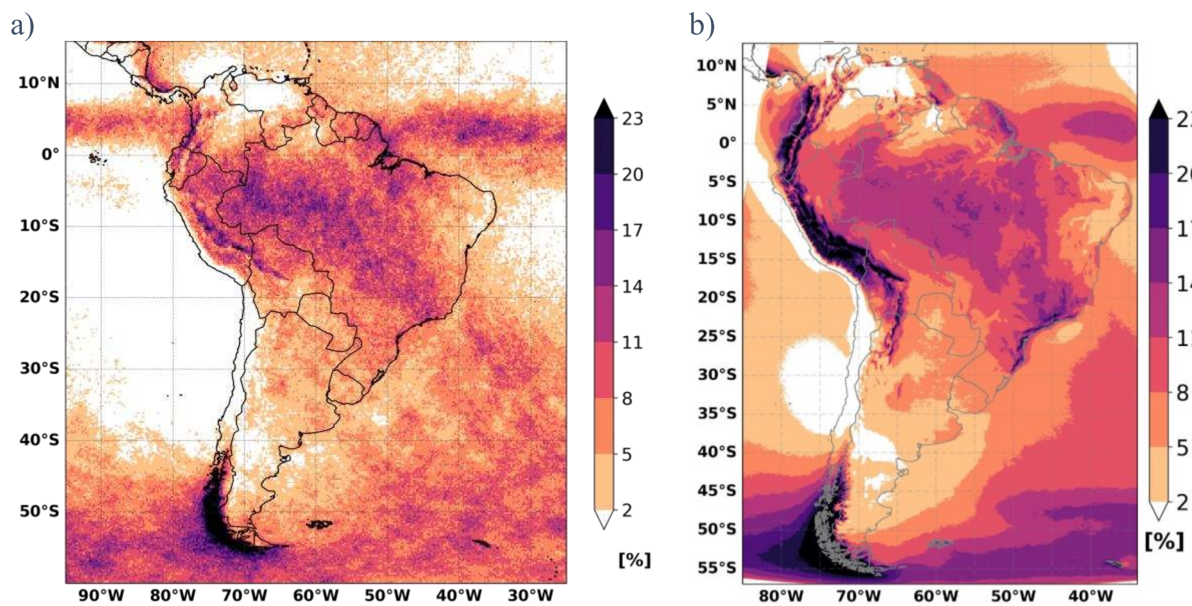

Figure 4.3. Climatological distribution of summer rain frequency over South America. (a) 2014-2024 GPM probability of sampling measurable rain per satellite overpass across the region. (b) 2000-2021 WRF wet hour (rain rate >= 0.1 mm/h) frequency, sampled every 3h.

4.3.2 Convective/Stratiform mask climatology

Precipitation events are also analyzed from a radar reflectivity standpoint. Figure 4.4 shows the frequencies of the simulated and observed radar echoes representing convective and stratiform rain events. Stratiform echoes generally represent the identification of large horizontal areas having weak upward motion, which is associated with weak to moderate rain intensities, while convective echoes are generally associated with areas having strong updrafts and moderate to strong rain rate intensities (Houze 2014). Based on GPM radar observations, the stratiform climatology (Figure 4.4a) resembles the wet hour frequencies shown in Figure 4.3, with a local maximum across the Amazon Basin, western Patagonia, and ITCZ regions. Over the ocean, stratiform precipitation is predominant in the extratropics, in association with baroclinic systems prevalent there. The observed convective echo climatology (Figure 4.4b) shows that this rain type predominates in the tropics, where it maximizes in the Amazon Basin and the ITCZ region. Convective precipitation is less frequent in middle latitudes. The 22-year simulation of summer convective and stratiform echoes (Figures 4.4c-d) generally captures the spatial distribution of convective and stratiform echoes in GPM, especially over the continent, where the simulated frequency values are very similar to the observed ones (note that the colorbars are the same for the GPM- and WRF-derived frequencies).

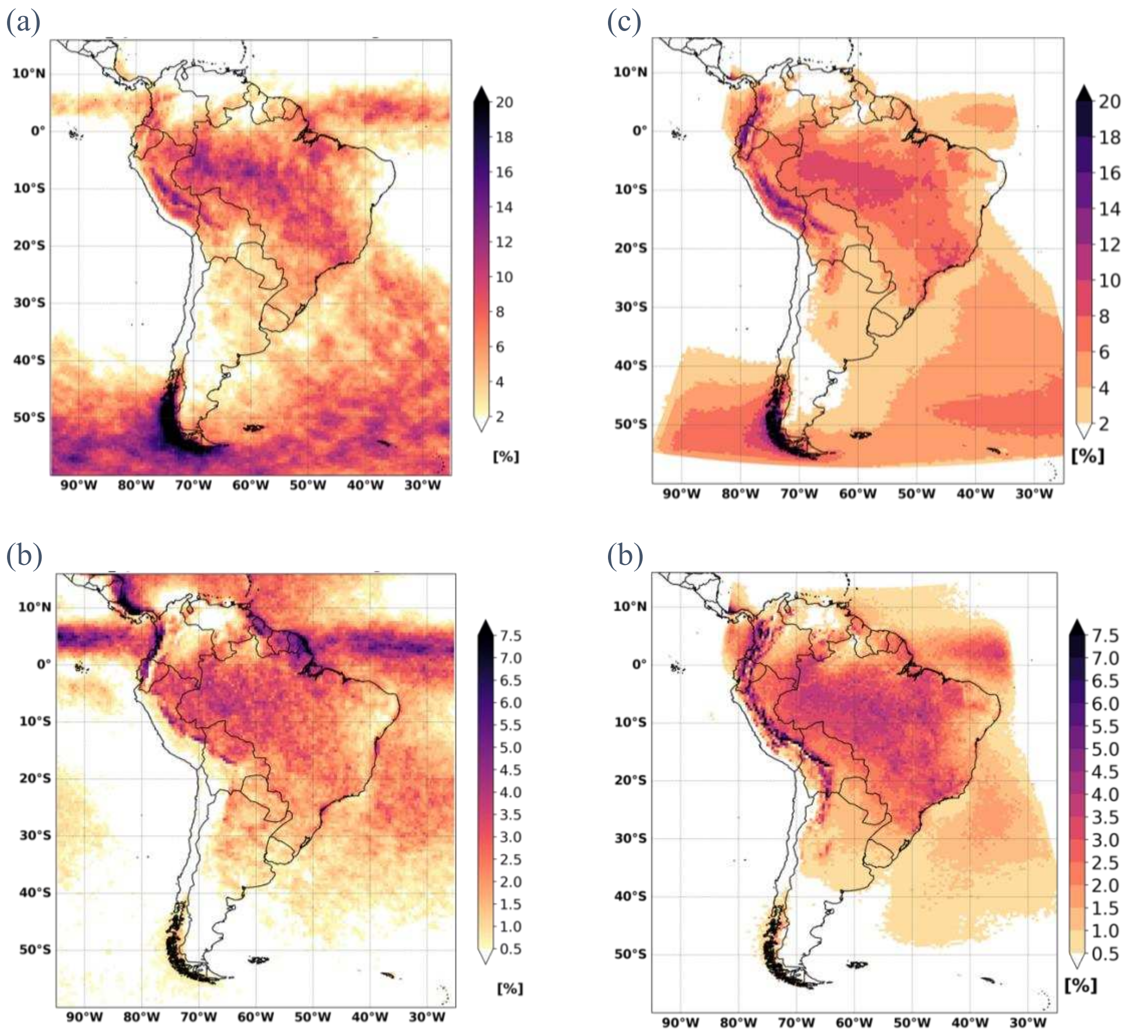

Figure 4.4. Climatological frequency of summer stratiform and convective echoes. GPM probability of identifying a (a) stratiform and (b) convective echo per each satellite overpass, and WRF frequency of (a) stratiform and (b) convective echoes at each grid point. GPM and WRF maps were interpolated to 0.5 × 0.5° and 48 × 48 km grids, respectively.

4.3.3 Storm mode climatology

Figure 4.5 shows the climatological frequency of different storm modes over South America during summer in GPM and WRF. From GPM observations, DCCs (Figure 4.5a) occur predominantly over the continental tropics and subtropics, having the highest occurrence over the southeastern portion of the Amazon basin, extending into the SACZ region, and also along the eastern Andes foothills that surround the Altiplano region. This pattern is slightly different from the pattern that previous studies using TRMM data have shown (e.g., Houze et al. 2015), where the region of enhanced DCC activity is not only located over southeastern Brazil but also extends across the subtropical plains and Andes foothills. The non-overlapping TRMM and GPM coverage periods, differences in sampling frequency in the subtropics, or model biases could explain these distribution frequency differences. The model shows good performance reproducing the DCC frequency distribution in South America (Figure 4.5b), generally capturing the areas of high and low DCC activity seen by GPM. However, the DCC frequency gradient across the Amazon in WRF is not as prominent as that in GPM. Overall, the model DCC distribution more strongly resembles GPM rather than TRMM distributions.

The observed WCC distribution (Figure 4.5c) highlights wide storms over both the continent and warm oceanic waters. Over the continent, WCCs peak in the deep tropics, extending to the eastern tropical Andes. Studies using precipitation datasets have also shown that MCS frequency peaks in that region (e.g., Prein et al. 2024), although others using TRMM radar reflectivity have shown WCC frequency instead maximizing in the subtropics (e.g., Houze et al. 2015). Over the Atlantic Ocean, WCC frequency maximizes over the ITCZ region but is also extensive over the subtropical Atlantic, where MCSs originating over the continent propagate and eventually dissipate (Romatschke and Houze 2010; Rasmussen and Houze 2011). WCCs identified using WRF (Figure 4.5d) present slight discrepancies with the regions where WCC peak in GPM. WRF indicates that WCCs are most frequent over the subtropical Atlantic and Pacific coast of Colombia, with a secondary maximum over the southern Andes of Chile. Next in frequency is tropical South America, with an evenly spread frequency across that region of about 0.10-0.16%, and then subtropical South America with less than 0.10-0.07% occurrence.

For DWCCs (Figure 4.5e), the observed frequency highlights both the tropics and subtropics as preferred areas of occurrence for these storms during the austral summer, predominantly over the continent. Over the subtropics plains and foothills is where these storms present the highest frequencies (over 1%). The simulated WRF distribution of DWCC in South America (Figure 4.5f), while presenting activity over all the regions highlighted by GPM, shows an apparent overrepresentation of DWCCs over the continental tropics, the Pacific Colombian coast, and portions of the tropical Andes eastern slopes.

For BSRs (Figure 4.5g), spaceborne radar observations over South America in austral summer highlight the extratropical oceans as an important location for extensive stratiform precipitation. Over the continent, western Patagonia presents the highest frequency of BSRs, predominantly associated with frequent synoptic disturbances and atmospheric river landfall (Falvey and Garreaud 2007; Viale et al. 2018) Over the tropics and portions of the subtropics, the occurrence of BSRs do not show large spatial differences, although some areas of enhanced activity can be noticed over portions of Brazil. The stratiform areas in the tropics are likely related to frequent convective systems occurring across the Amazon basin (Liu and Zipser 2013; Feng et al. 2021). The ITCZ over the Atlantic is also a region with increased BSR activity. The simulated BSR frequency (Figure 4.5h) reproduces the observed behavior reasonably well, maximizing their occurrence over the extratropical oceans and western Patagonia, and also featuring enhanced activity over parts of the tropics highlighted by observations.

In summary, despite some biases in the spatial distribution of certain storm modes, the model reproduces the dominant climatological patterns of the different storm modes reasonably well. This provides confidence in using this modeling framework to investigate how the characteristics of these precipitating storm systems may respond to future climate change.

(c)

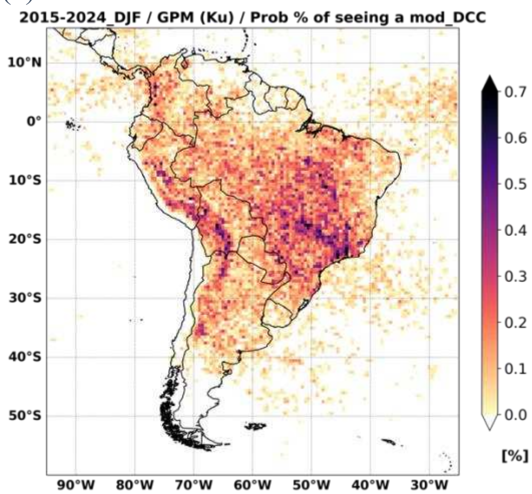
2015-2024_DJF / GPM (Ku) / Prob % of seeing a mod_DCC
10°N
0°
10°S
20°S
30°S
40°S
50°S
90°W 80°W 70°W 60°W 50°W 40°W 30°W
0.7
0.6
0.5
0.4
0.3
0.2
0.1
0.0
[%]

(b)

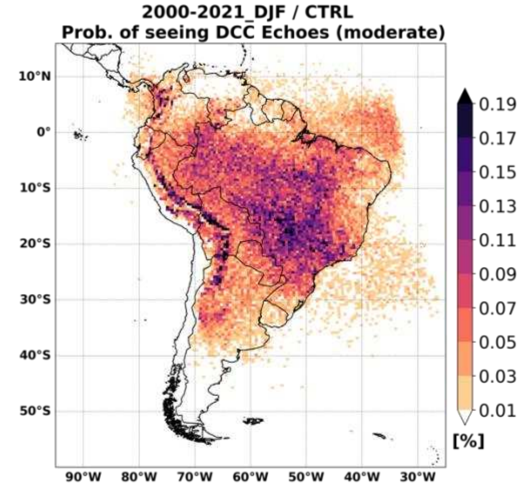
2000-2021_DJF / CTRL
Prob. of seeing DCC Echoes (moderate)
10°N
0°
10°S
20°S
30°S
40°S
50°S
90°W 80°W 70°W 60°W 50°W 40°W 30°W
0.19
0.17
0.15
0.13
0.11
0.09
0.07
0.05
0.03
0.01
[%]

(c)

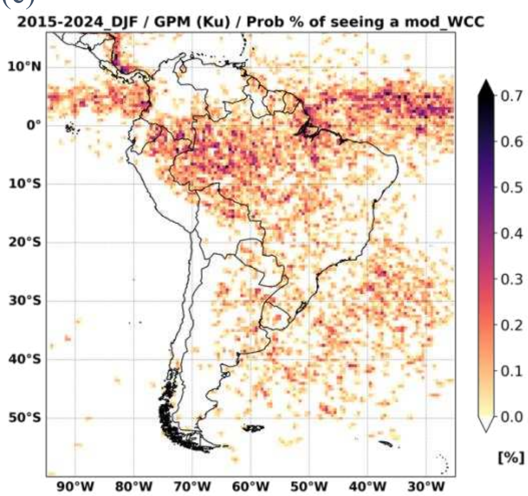
2015-2024_DJF / GPM (Ku) / Prob % of seeing a mod_WCC
10°N
0°
10°S
20°S
30°S
40°S
50°S
90°W 80°W 70°W 60°W 50°W 40°W 30°W
0.7
0.6
0.5
0.4
0.3
0.2
0.1
0.0
[%]

(d)

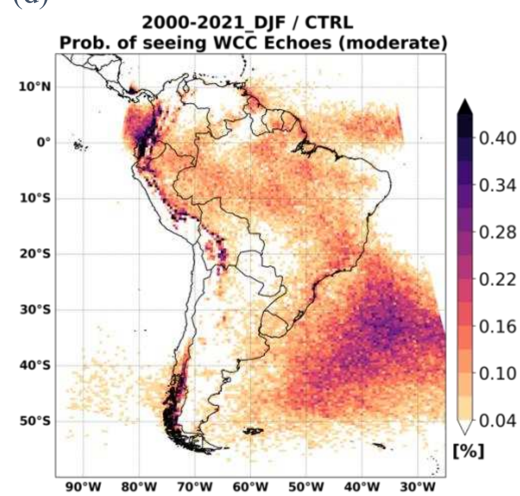
2000-2021_DJF / CTRL
Prob. of seeing WCC Echoes (moderate)
10°N
0°
10°S
20°S
30°S
40°S
50°S
90°W 80°W 70°W 60°W 50°W 40°W 30°W
0.40
0.34
0.28
0.22
0.16
0.10
0.04
[%]

(e)

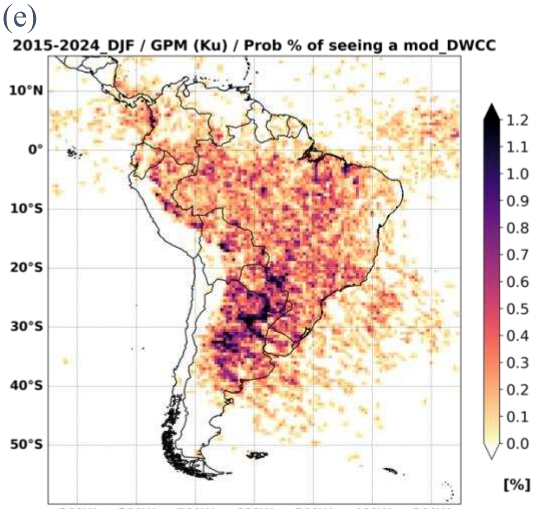
2015-2024_DJF / GPM (Ku) / Prob % of seeing a mod_DWCC
10°N
0°
10°S
20°S
30°S
40°S
50°S
90°W 80°W 70°W 60°W 50°W 40°W 30°W
1.2
1.1
1.0
0.9
0.8
0.7
0.6
0.5
0.4
0.3
0.2
0.1
0.0
[%]

(f)

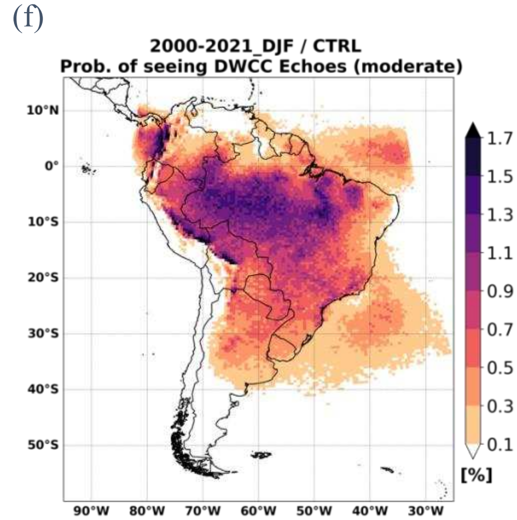
2000-2021_DJF / CTRL
Prob. of seeing DWCC Echoes (moderate)
10°N
0°
10°S
20°S
30°S
40°S
50°S
90°W 80°W 70°W 60°W 50°W 40°W 30°W
1.7
1.5
1.3
1.1
0.9
0.7
0.5
0.3
0.1
[%]

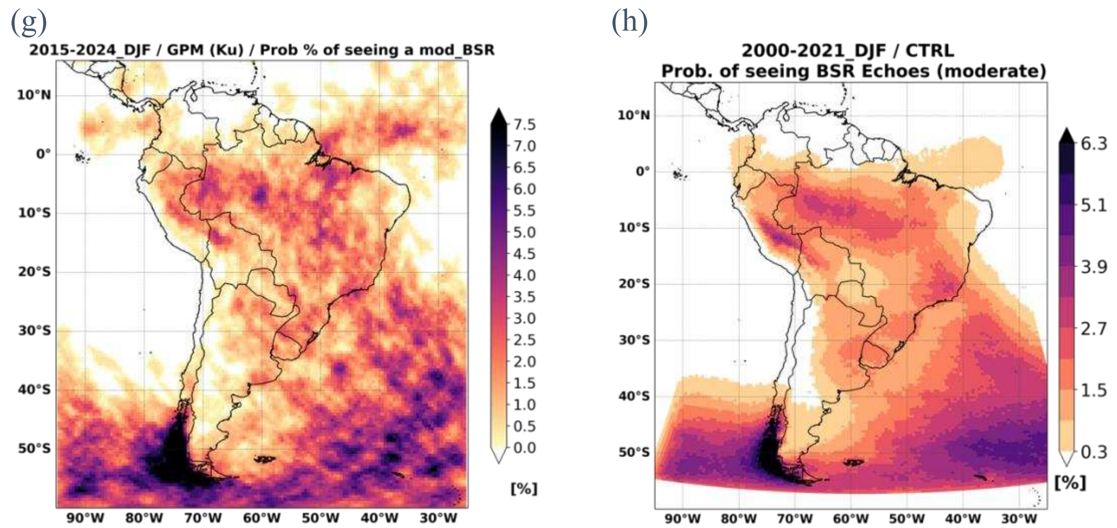

Figure 4.5. Climatological frequency of different storm modes in summer. GPM probability of identifying (a) DCCs, (c) WCCs, (e) DWCCs, and (g) BSRs per satellite overpass. 2020-2021 WRF frequency of (b) DCCs, (d) WCCs, (f) DWCCs, and (h) BSRs, at each gridpoint. GPM and WRF maps were interpolated to a 0.5 × 0.5° and 48 × 48 km grids, respectively.

4.4 Future changes

Using the pseudo global warming approach, a future climate simulation was run over the same domain as in the control simulation to assess a future scenario for South America's hydroclimate. Figure 4.6 presents the climatological difference between the SAAG-PGW and SAAG-CTL simulations for precipitation frequency and intensity. The changes in rain event frequency (Figure 4.6a) resemble some of the changes in summer precipitation shown in previous studies across South America (Llopart et al. 2020; Reboita et al. 2022a,b) The predominant continental pattern shows a dipole in tropical South America, with a small increase in precipitation frequency over eastern Brazil and a decrease across most of the Amazon region. A dipole is also observed in the subtropics with a decrease in rain events in the northeastern subtropics and a small increase across Argentina. Near the Andes, a large decline in rainfall events is evident across the tropical and southern Andes, including western Patagonia. Over the equatorial oceans, this change represents a southward shift in the ITCZ. A similar future southward shift has been projected by climate models over the eastern Pacific and Atlantic oceans during the austral summer (Mamalakis et al. 2021). The ITCZ shift likely influences some of the changes seen in tropical South America, given the proximity of the Atlantic ITCZ to the continent.

The changes in rain intensity (Figure 4.6b) generally show an increase in intensity across South American land areas, except for the northernmost part of the continent and portions of western Patagonia, which show slight decreases. Increases in rain intensity are observed even in regions where rain frequency is decreasing, and it seems to follow the response to the increase in global air temperature and the subsequent increased atmospheric moisture content following the Clausius-Clapeyron relationship (Held and Soden 2006). The concomitant reduction of precipitation frequency and increase in precipitation intensity in the tropics agrees with the theoretical - and recently observed - changes in precipitation expected under a warmer climate (Fischer and Knutti 2016; Fu and Wu 2024). The ITCZ shift is also observed in changes in rain intensity and appears to influence the reduced intensity in northern South America.

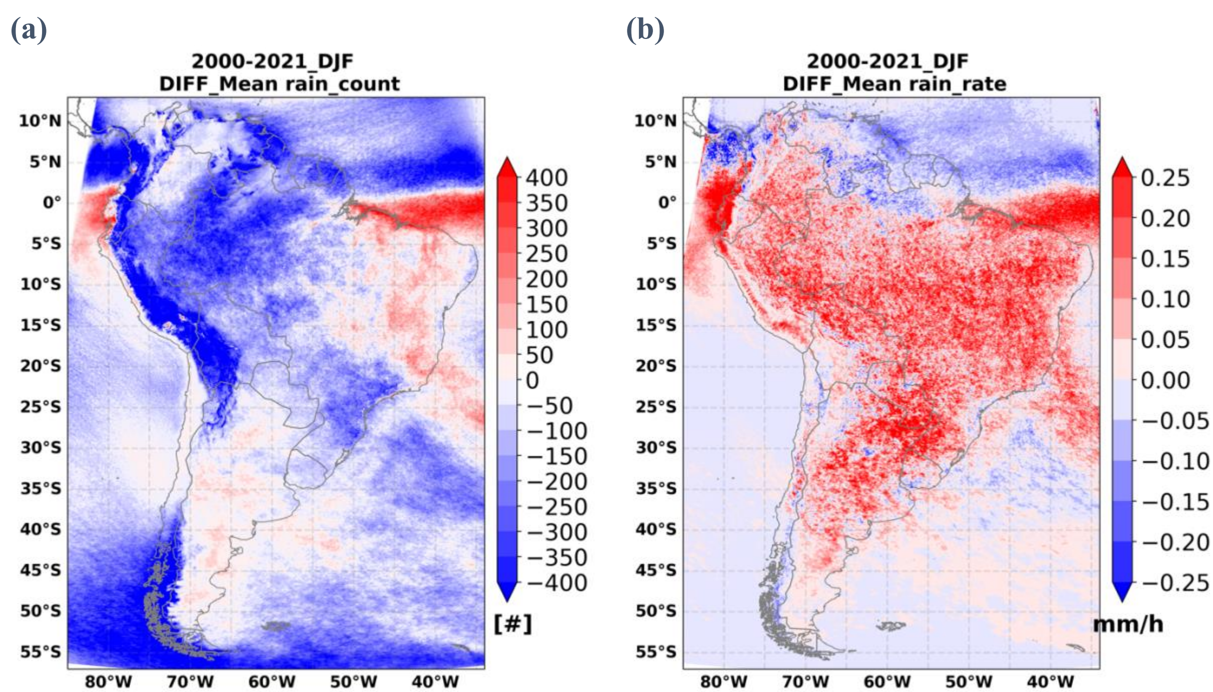

Figure 4.6. PGW – CTRL difference in (a) total count of wet hours and (b) mean rain rate for DJF.

For the convective-stratiform echoes (Figure 4.7), future frequency changes present some similarities among both types of precipitation, with a similar spatial structure to the precipitation frequency changes discussed above: frequency decreases over most of the Amazon Basin and increases over eastern Brazil and Argentina. While the ITCZ shift and continental dipole over tropical South America are reflected in both stratiform and convective precipitation changes, for convective rain, the increase in the eastern tropics extends further west (up to 40W). Over the tropical Andes, a large increase in convective precipitation seems to be counteracted by a decrease in stratiform precipitation. For southern South America, changes in frequency are only observed for stratiform precipitation (which is the predominant precipitation type), with decreases between 37S and 50S in southern Chile and increases in the southern tip of the continent and eastern Patagonia. These changes in southern South America agrees with similar projections made by other studies (Pachauri et al. 2015; Polade et al. 2017; Bozkurt et al. 2018).

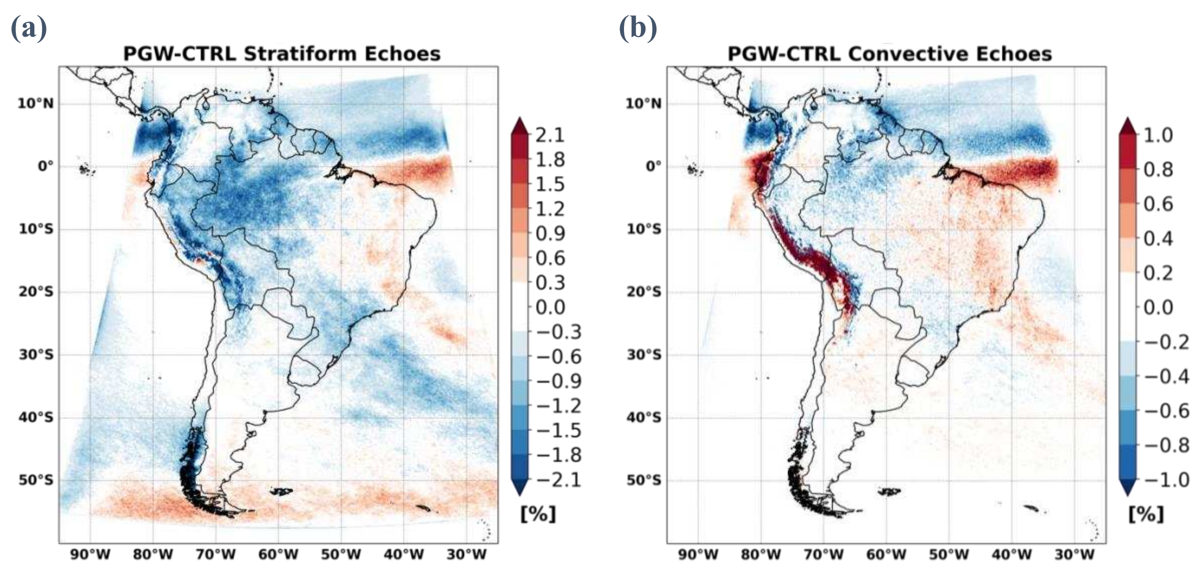

Figure 4.7. PGW – CTRL difference (%) in the probability of having a (a) stratiform and (b) convective echo in austral summer.

Future changes in the frequency of different extreme storm structures over South America are also assessed. Figure 4.8 presents the projected changes for DCC, WCC, DWCC, and BSR. Changes in these storms do not present the same spatial pattern as changes in precipitation. Overall, there is a clear increase in the frequency of storms containing DCCs (Figure 4.8a-b) almost everywhere these storms are capable of developing. The increase in DCC frequency appears larger over the tropics than the subtropics, with a particularly notable increase across the SACZ region. The largest increases are projected over the Atlantic ITCZ and along both slopes of the tropical Andes. WCC changes show an overall decrease in frequency across tropical South America, with the exception of the western tropical Andes foothills, where an increase is projected. The subtropical South Atlantic also shows a decrease in WCC activity, over the region where WCC occurrence peaks (Figure 4.5). The continental subtropics do not show any significant changes in WCC frequency. For DWCC, which contains both DCC and WCC within the same storm object, the spatial increase in frequency is very similar to that seen for DCC, but the strong increase across the tropical Andes is only apparent in parts of Altiplano. There is a notable increase in DWCC frequency on the coast of Ecuador and southern Colombia, which seems to be associated with the eastern Pacific ITCZ changes discussed previously. That region is characterized by strong convective systems that propagate offshore (Zuluaga and Houze 2015; Jaramillo et al. 2017), so this could indicate a reinforcement of that phenomenon due to climate change. Overall, it appears that the increase in DCC activity (Figure 4.5a) causes WCC storms to occur concurrently with DCC storms more often. As a result, more DWCC storms are identified (Figure 4.5c) in detriment of WCC alone that are decreasing (Figure 4.5b). For BSR changes, the spatial pattern follows the stratiform precipitation change in frequency, with some minor dissimilarities (Figure 4.7a). The largest decrease is observed in the eastern Amazon and over most of the subtropical to midlatitude

South Atlantic. In synthesis, a shift in the storm mode is projected in the tropics and subtropics of South America: increased frequency of intense convective cores (DCC and DWCC) producing more frequent heavy rainfall events, and decreased frequency of moderate MCS-like storms (WCC and BSR) associated to more moderate to light rainfall rates. This shift is consistent with the expected predominant reduction in precipitation frequency and concomitant increases in precipitation intensity over the Amazon Basin discussed above (Figure 4.6).

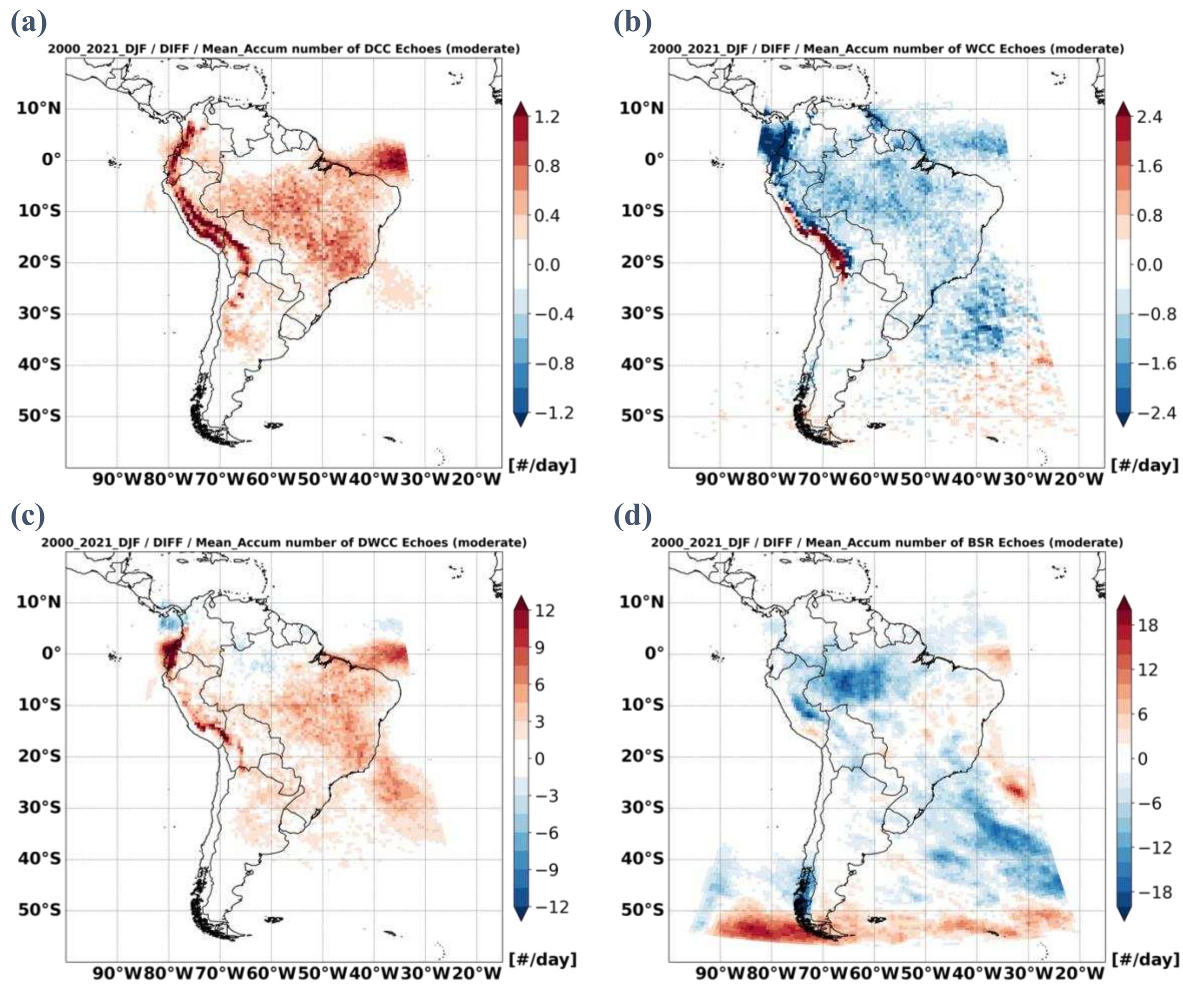

Figure 4.8. PGW – CTRL difference in storm mode frequency (units are events per day) during DJF. Storm modes are (a) DCCs, (b) WCCs, (c) DWCCs, and (d) BSRs. Events are accumulated into 60 km × 60 km grids.

To explore the environmental conditions leading to the changes in storm frequency discussed above, changes in the climatological austral summer CAPE and CIN environments in South America are analyzed (Figure 4.9). For CAPE, higher values with warming are projected everywhere. Continental land tends to show larger increases compared to the surrounding oceans, except in the tropical oceans and the subtropical Atlantic, where increases are also appreciable. For subtropical South America, CAPE changes are smaller compared to the tropics, while in tropical South America there is a gradual increase in CAPE from east to west. For CIN changes, increases are projected in many regions, including the coast of Perú, over northern South America, and across the entire continental extratropics. Over the continental tropics, the CIN does not seem to change significantly under future climate conditions. Predominant CAPE increases and CIN decreases have been also projected over South America by previous studies using GCMs (Chen et al. 2020b).

The effects of the CAPE and CIN changes (Figure 4.9) could explain the projected changes in precipitation frequency and intensity (Figure 6). The overall increase in instability and reduction in convective inhibition could be responsible for the predominant increase in rain intensity, as these changes would lead to stronger updrafts and subsequently stronger rain rates. Despite being small, CIN increases in the eastern Amazon could contribute to the reduction in the total number of wet hours by preventing weak rain events from occurring. In relation to the storm mode changes (Figure 4.8), the increased instability projected for South America's tropics and subtropics could drive stronger updrafts, thus favoring deeper storms (i.e., more DCCs).

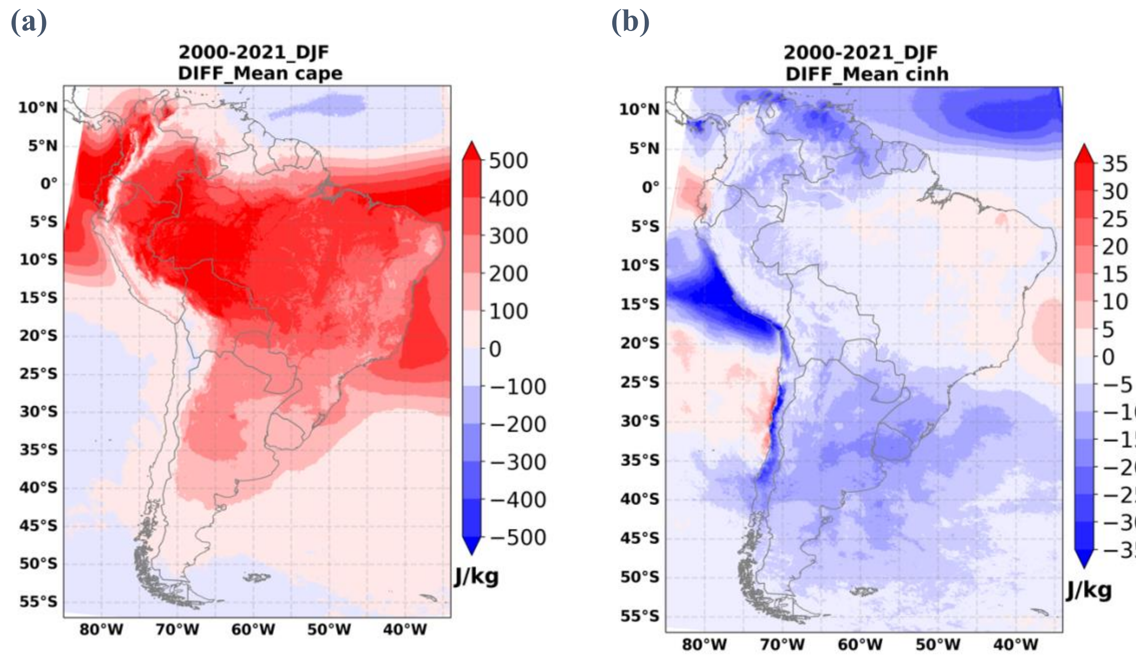

Figure 4.9. PGW – CTRL mean absolute difference (J/kg) in DJF: (a) CAPE and (b) CINH.

Storm changes can also be analyzed from a storm-centered standpoint, allowing the analysis of storm characteristics associated with each storm mode. Changes in storm features are summarized for four different subregions across tropical and subtropical South America (Figure 4.1) presenting different rainfall regimes and different future precipitation changes. A tracking algorithm (Hudson and Maloney 2023) is used to identify each individual storm observed across each subregion. With this information, statistics for different storm properties can be extracted at each time step for SAAG-CTL and then contrasted with SAAG-PGW. Figure 4.10 presents heatmaps indicating the intensity and sign of change for several different storm features (more details in Chapter 4.2.3). Overall, the changes in the total number of individual storms generally match the changes in storm mode frequency seen from a grid cell standpoint (Figure 4.8), with DCC and DWCC storms increasing almost everywhere and WCCs becoming less frequent in the future. Besides *n_storms*, only changes in *VOLR* can exceed 20% in some cases. The rest of the storm features typically show percentage values that are considerably lower but still statistically significant in most cases. The sign of change for all the DWCC-related storm features are generally positive everywhere. For DCCs, while predominantly positive, decreases are projected for some variables (e.g., *maxW*, *maxUHEL*, and *maxdbz*). WCCs present predominantly negative changes for most variables and subregions.

Some of the storm feature changes deserve closer inspection. *VOLR* changes in DCCs show a larger increase (>20%) in the tropical subregions, while the subtropical subregions show weak to no change. This contrast seems to be driven by changes in precipitation intensity rather than storm area, as *maxRR* increases in tropical regions compared to decreases in the subtropics. Despite this contrast, individual storm size areas are increasing for DCC and DWCC, thus making storms wider in the future. For *maxdbz*, a general reduction or no change across storm modes and subregions is observed, which contrasts with a general increase in *maxdbzh*. This means that while the maximum reflectivity observed in the storms may be decreasing to some degree, the height of this maximum increases. This suggests changes to storm vertical structure, which can be explored further by looking at echo top height changes. In the case of *mxht40*, a ~1% increase is observed for DCC and WCC, while for DWCC the increase is larger (~5%). For *mxht00*, 1-2% decreases are generally observed for DCC and WCC, while predominant increases (~2-4%) are expected for DWCC. All these changes in the vertical structure of the storms suggests that DWCC are becoming more intense, with higher echo top heights and similar maximum reflectivity values. However, for DCC and WCC, the opposite sign changes in *mxht40* and *mxht00* along with decreases in *maxdbz* seem to suggest a slight decrease in storm vertical development.

Another interesting connection can be made from the overall changes in WCC and DWCC frequency and intensity. It appears that a certain percentage of WCCs transition from WCC identified storms to DWCC. As shown in Figure 4.2, DWCC corresponds to a WCC containing embedded DCCs. This seems to occur due to an increase in DCCs across each subregion for SAAG-PGW, which increases the likelihood of having a DCC embedded within a WCC. When this happens, a storm identified as a WCC in SAAG-CTL would be now a DWCC in SAAG-PGW. The WCC decrease in frequency can be also caused by the transition of some moderate WCCs into strong WCCs in the future, which is considered a different storm mode category.

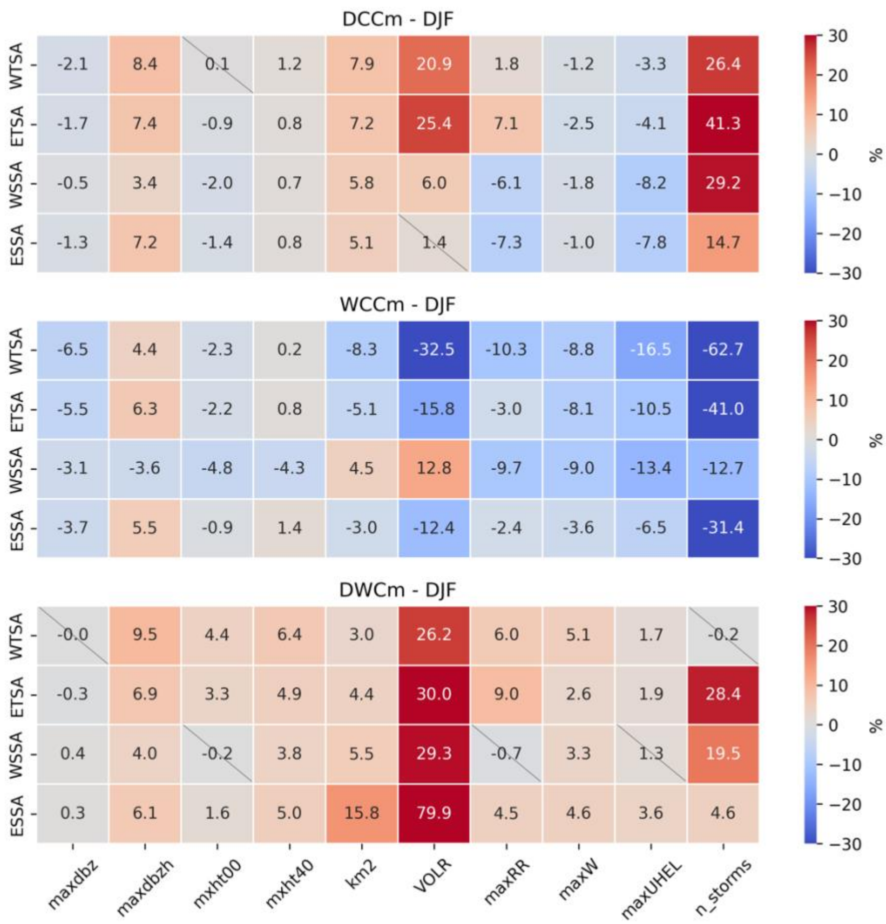

Figure 4.10. Heatmaps showing percentage change for several storm features in four different subregions in South America, for moderate DCC (top), WCC (middle), and DWCC (bottom). Values that are not statistically significant at 95% (t-test) have a strikethrough diagonal line. A description of what each variable represents can be found in Chapter 4.2.3.

To further explore the changes in frequency and intensity of storm modes across South America, the summary changes expressed in the heatmaps (Figure 4.10) are expanded into histograms for SAAG-CTL and SAAG-PGW. This perspective allows examination of the actual range of values each variable can reach and visualize any shifts in the distribution of storm characteristics in the future. Figure 4.11 shows the distribution of six different storm features associated with DCCs across the four different subregions for both simulations. Overall, the storm properties present differences in the mean values for different subregions, indicating that the nature of a DCC is not exactly the same in every part of South America. For example, while in the tropics the maximum rain rate within a DCC is normally around 25-30 mm/h, for the subtropics the mean is around 18 mm/h for ESSA and 12 mm/h for WSSA, which also explains the large tropics/subtropics differences in *VOLR*. For *VOLR*, the distribution of values is skewed towards smaller values, with subtropical storms presenting the largest skew. As a result, DCCs produce much more rainfall accumulation in the tropics despite presenting a similar size to subtropical storms. While some percentage changes seemed small, in absolute terms these changes can have large effects. For example, *maxdbz* shows a clear shift in the distribution towards smaller reflectivity values, especially in the tropics. The storm size area also presents a clear shift towards wider storms in all subregions, despite mean percentage changes below 8%. The maximum rain rate also shows a shift – although less evident – that aligns with the opposite sign changes discussed previously between the tropics and subtropics for DCCs. These changes in *maxRR* and *km2* result in a notable shift towards larger *VOLR* values for tropical DCCs that matches the percent changes discussed above. As for changes in echo-top height, a robust shift in the distributions is less evident, in line with the weak 0-2% changes expected for *mxht00* and *mxht40* in DCC storms.

Figure 4.12 shows similar histograms, but for WCCs. Unlike DCCs, WCC storms are less intense, which is evident in the distribution of variables such as maximum reflectivity and echo-top heights that span weaker reflectivities and lower heights. However, because WCCs are large systems by definition, they produce significantly more volumetric rain than DCCs (~10^6 versus

~10^4 km^2 mm h^{-1}). In terms of future changes in the distributions, some parameters such as *maxdbz*, *km2*, or *VOLR* generally depict a shift in the center or the mean of the distribution towards smaller values. Other parameters, however, show an increase in the spread of the distribution. This is clear in *mxht00* and *mxht40*, where values on both tails of the distribution increase in frequency while the center of the distributions gets flattened. This change in the distribution of echo-top heights can be explained by a combination of newly identified WCC storms and the strengthening of existing WCCs in SAAG-PGW. If a new WCC is identified over a region where no storm was identified under present climate, it means that this storm is now meeting the minimum thresholds to be identified as a WCC (it was probably close to be identified as a WCC in SAAG-CTL). As a result, this new storm in SAAG-PGW will probably be at the weaker end of the intensity spectrum, thus increasing the frequency of values on the left side of the distribution. Meanwhile, existing WCCs getting stronger will likely have higher echo-top heights, thus shifting their values to the right half of the distribution. Even the transition from WCC to DWCC could further explain the distribution changes, as the newly embedded DCCs are likely taking away WCC storms that present on average echo-top heights around the center of the distribution. It is also possible that weak WCC on SAAG-CTL could shift to the center of the distribution in SAAG-PGW, but given that the distribution changes for *mxht00* are showing larger increases in frequency on the left side of the distribution (Figure 4.12) we can infer that newly identified weak WCCs outnumber other WCC distribution changes.

For DWCCs, storm feature distribution changes are shown in Figure 4.13. Overall, the storm features analyzed do not present significant differences in the range of values across the different subregions analyzed. Only *maxRR* reaches higher rain rates in the tropics (~50 mm/h on average) compared to the subtropics (~35-45 mm/h). Compared to other storm modes, DWCCs show higher values for echo-top heights and maximum reflectivity than DCCs, higher rain rates than DCCs and WCCs, and one order of magnitude higher *VOLR* than that from WCC storms. The future changes in DWCC storm feature distributions are generally consistent with the summarized percent changes discussed previously. The variables showing increases in the future generally feature a shift in the distribution towards higher values, and variables showing no change such as *maxdbz* show an increase in the spread the with same mean. One interesting result is that when comparing tropics and subtropics, the change in the distribution of intensity-related features (*mxht00*, *mxht40*, *maxRR)* is clearer in the tropics, with a robust shift to the right, while in the subtropics such shift is not as clear. This difference may be associated with the larger range of values that some features can reach in the subtropics, which causes the histogram and mean changes to appear less prominent.

One important factor to be considered is that these differences PGW – CTL are not necessarily related to the same storms changing their features: there are storms in SAAG-CTL that change intensity but there are also new storms that are identified in SAAG-PGW in a same timestep, or even storms that no longer met the minimum criteria (see Figure 4.2). It is therefore difficult to conclude that a certain storm (e.g., DCC) is becoming stronger or weaker; instead, the focus should be on the overall population of storm types.

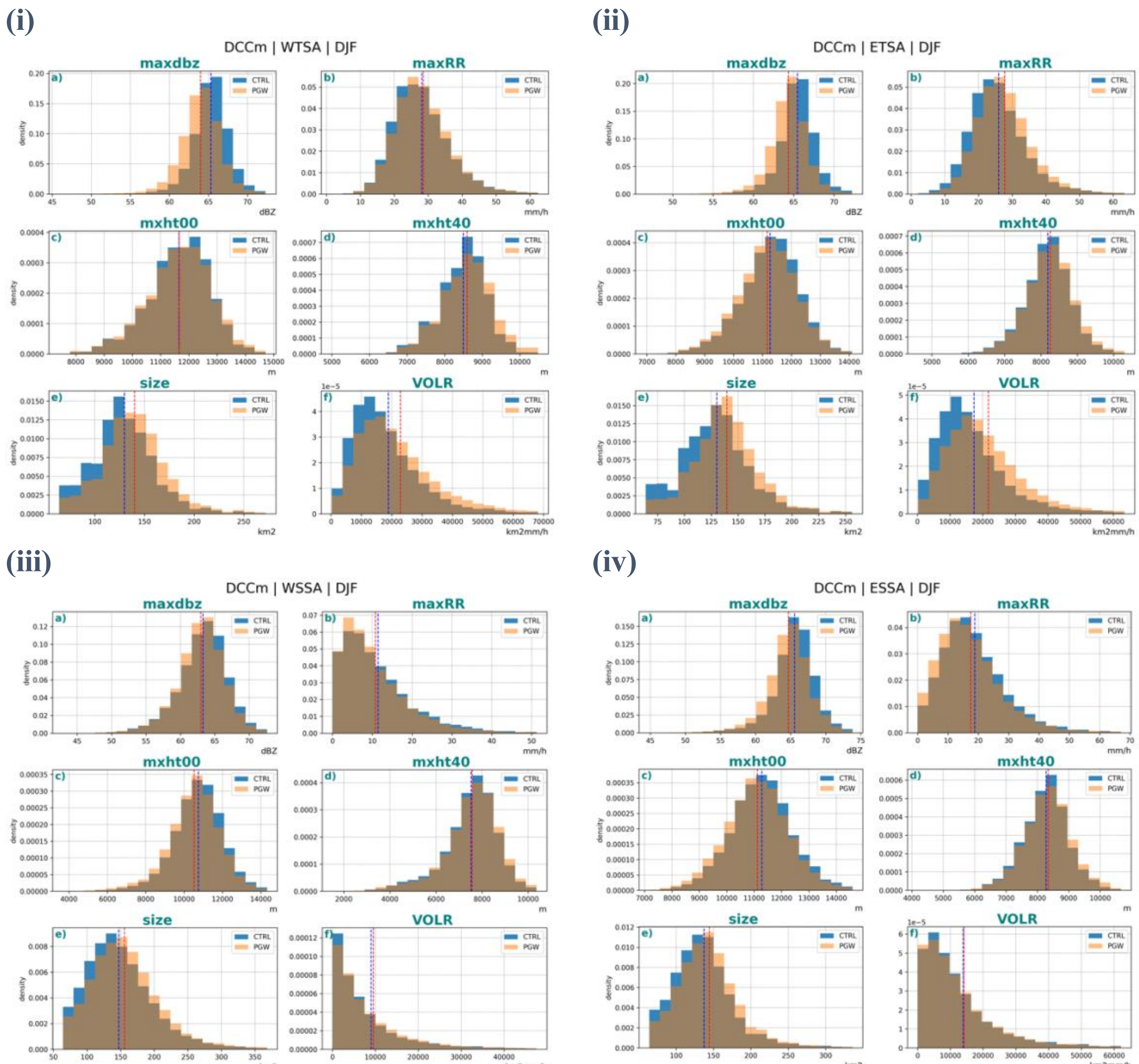

Figure 4.11. CTRL (blue) and PGW (pink) distribution for different storm features associated with DCCs identified over (i) WTSA, (ii) ETSA, (iii) WSSA, and (iv) ESSA. Storm features are: (a) maximum reflectivity (dBZ), (b) maximum rain rate (mmh^{-1}), (c) maximum 0 dBZ echo top height (m), maximum 40 dBZ echo top height (m), horizontal size (km^2), and volumetric rain (km^2mmh^{-1}). The vertical blue and red dashed lines represent the mean for the CTRL and PGW distributions, respectively.

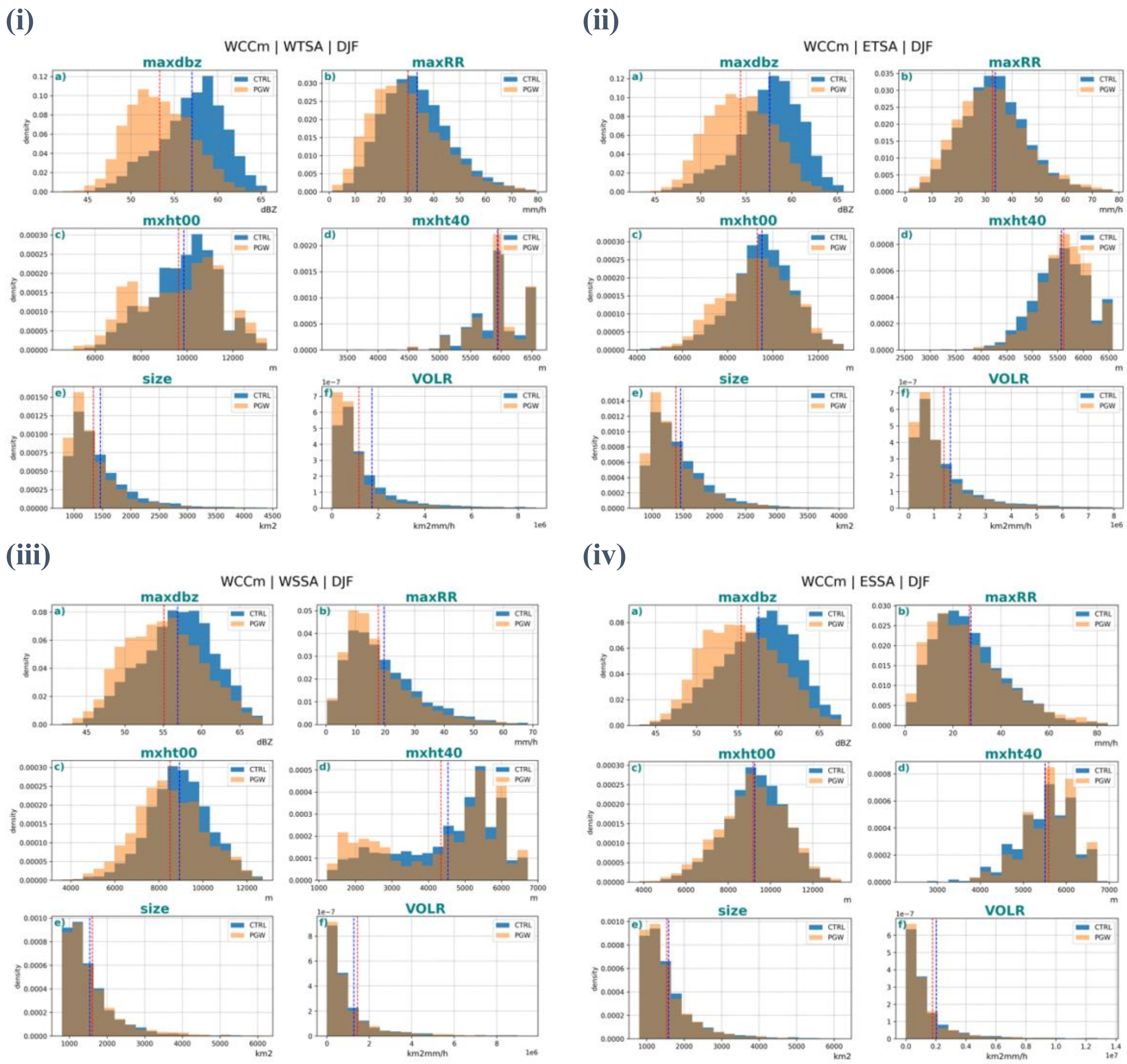

Figure 4.12. As in Figure 4.11, but for WCC.

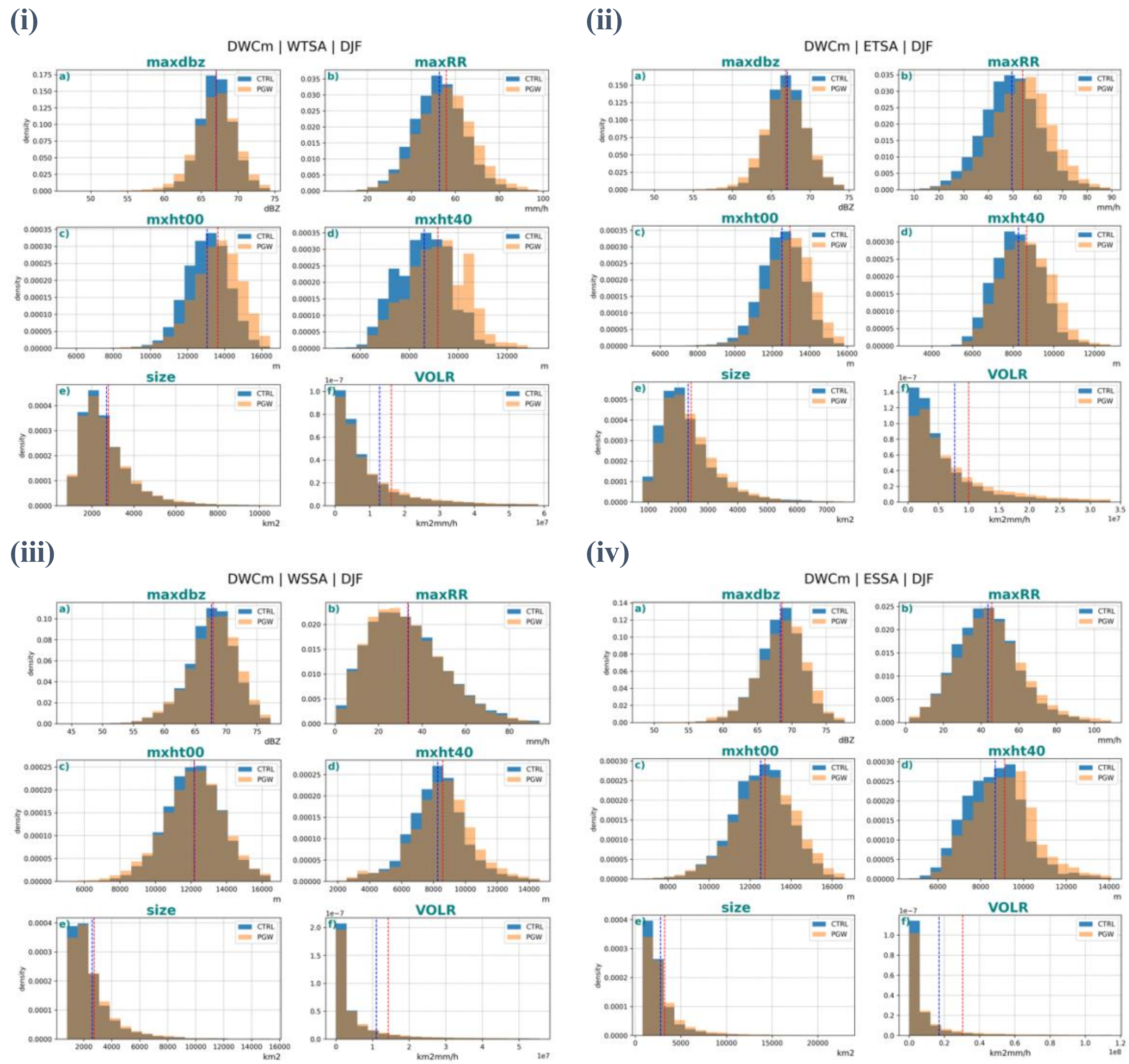

Figure 4.13. As in Figure 4.11, but for DWCC.

4.5 Conclusions

A 22-year convection-permitting WRF simulation conducted over South America was analyzed under present and future climate conditions. The long-term nature of the simulation at high resolution over the entire continent allows an unprecedented study of the climatological aspects of convective storms and their changes under a warmer climate. The future climate simulation uses the PGW approach to project changes under an SSP3-7.0 emissions scenario.

The historical period is first examined to determine its performance in reproducing austral summer precipitation and extreme storms across South America. Satellite observations from GPM are used as ground truth. The simulated precipitation frequency shows a good correspondence with the spatial pattern from satellite-derived precipitation frequency across South America. Subclassifications of precipitation as convective and stratiform are also well represented spatially. Stratiform rain shows a spatial pattern similar to that of the precipitation frequency climatology, with enhanced rainfall frequency over portions of the tropics and western Patagonia. Convective rain events are predominant over portions of the continental tropics and over the ITCZ regions, but become less frequent in the extratropics.

Four storm modes representing different extreme storm structures are also studied. The model represents well the spatial frequency of deep convective cores (DCCs), with higher occurrence over the continental tropics and subtropics, peaking over the Peruvian-Bolivian Andes and southeast Brazil (SACZ region). The model also performs well in capturing the spatial distribution of broad stratiform regions (BSRs), showing higher occurrence over the extratropical oceans and across the continental tropics. Some discrepancies between the observed and simulated climatology of wide convective cores (WCCs) are noticed. GPM-derived WCCs predominate over the continental tropics and warm oceanic waters. The WRF simulation also presents an enhancement of the WCC frequency in these regions, but with some discrepancies in the regions where these storms peak. The discrepancies for deep and wide convective cores (DWCCs) are larger. While GPM shows the largest frequency of these storms over the continental tropics and subtropics, with the highest occurrence over the subtropics, the model reproduces these storms more frequently across the Amazon Basin.

The present (SAAG-CTL) and future (SAAG-PGW) climate simulations are contrasted to assess changes in frequency and intensity of austral summer precipitation and extreme storms. Precipitation frequency changes depict a pattern change that has been observed in previous studies, with decreases in precipitation frequency in the Amazon Basin and the SACZ region, and increases in Argentina and eastern Brazil. Precipitation intensity is expected to increase almost everywhere across the continent, including in areas where the frequency is decreasing.

For precipitation classified as stratiform and convective, future changes in frequency show that both have a similar spatial pattern to the overall precipitation frequency changes. For convective rain, the increase in the eastern tropics extends further west, while for stratiform rain a more pronounced decrease in frequency region is evident over western Amazon. Over the tropical Andes, a shift from stratiform to more convective precipitation is projected.

Changes in frequency and intensity of extreme storms over South America are analyzed by looking at storm modes representing different storm structures. Changes in intensity are explored by analyzing changes in storm features extracted per individual storm.

For DCCs, frequency changes project increases across both tropical and subtropical South America. A DCC storm is expected to become wider, but with a slight decrease in its intensity (e.g., decrease in storm maximum reflectivity and maximum updraft) that becomes more pronounced in the subtropics (including decreases in storm maximum rain rate). However, these storms will contribute to more overall rainfall (volumetric rain) in the future, especially in the tropics.

For WCCs, a predominant decrease in frequency is expected across most of the continental tropics and subtropical Atlantic off the south Brazil coast, whereas the continental subtropics show almost no change. WCCs present a more pronounced decrease in storm intensity. A WCC storm would become narrower and less rainy in the future.

For DWCCs, changes follow a similar behavior as DCCs, with increases almost everywhere in the tropical and subtropical continental areas. DCC storms are projected to become larger and more intense, as features such as echo-top heights and maximum rainfall rates are generally expected to increase. Consequently, these storms are expected to increase their contribution to the overall rainfall accumulation in the future for both tropical and subtropical South America.

Based on the definition of DWCC storms (Figure 4.2), the fact that WCC storms are decreasing and DCC and DWCC storms are predominantly increasing over the same regions gives the impression that many WCC storms seen in SAAG-CTL are transitioning to DWCC in SAAG-PGW owing to new DCCs growing embedded in WCCs. Further analysis is required to confirm this hypothesis.

The increases in precipitation intensity concomitant with decreases in precipitation frequency in parts of tropical South America (e.g., Amazon Basin) are consistent with the changes expected under a warmer climate in the tropics (Fu and Wu 2024). These changes are also consistent with the future storm mode shift favoring more intense storms (DCCs and DWCCs) at the expense of WCCs and BSRs. Increases in CAPE across the continent along with weak increases in CIN explain most of the projected shifts in precipitation and storm modes in South America.

The changes in frequency and rainfall accumulation coming out from DCCs, WCCs, DWCCs, and BSRs described above could produce a shift in the contribution of each storm mode to the total rainfall accumulation over the region in the future. This could be an avenue for future research, with important implications for water security and disaster risk across vulnerable communities across South America.

CHAPTER 5

Dissertation Conclusions and Future Work

5.1 Summary

This dissertation has explored the multiscale nature of convective storms in South America, from the specific environmental conditions that support tornadoes in the subtropics to the broad influence of global climate patterns on storm structures in the tropics and subtropics, and future climate change effects on extreme convective storms. By integrating observational data, reanalysis products, and high-resolution climate simulations, a more comprehensive understanding of the continent's storm environments and structures has been developed. This work is separated into three distinct papers. The first paper (Chapter 2, published in *Monthly Weather Review*; Veloso-Aguila et al. 2024) relied on a self-constructed database of tornadoes reported across southeast South America and ERA5 reanalysis data to describe the mesoscale to planetary-scale environments that support tornado formation in this region. The second paper (Chapter 3, currently under review in *Journal of the Atmospheric Sciences*) used a TRMM-derived precipitation feature database and ERA5 reanalysis data to explore the MJO intraseasonal modulation of storm structures in the tropics and subtropics of South America. The third paper (Chapter 4, currently under preparation to be submitted to a scientific journal) used GPM three-dimensional radar observations and model data from a convection-permitting climate simulation over South America to first validate the model performance in reproducing South American convection in the current climate and then to project changes in the frequency and intensity of precipitation and extreme convective storms across South America in a warmer climate.

Chapter 2 presents a multiscale analysis of the environments supporting tornadoes in southeast South America (SESA). Tornadogenesis is favored by a combination of enhanced instability (CAPE), deep-layer vertical wind shear, and storm-relative helicity. At the synoptic scale, these conditions are often established by a strong trough crossing the Andes, which triggers lee cyclogenesis and strengthens the South American Low-Level Jet (SALLJ), thereby increasing moisture transport into the region. On a planetary scale, this tornadic environment is modulated by Rossby wave trains that appear to be forced by convection over the western Pacific, with a preferential occurrence of the Madden-Julian Oscillation (MJO) phase 3 a few weeks prior to tornado events. A key finding was that while many environmental parameters for SESA tornadoes are similar to those in the U.S. Great Plains, the low-level wind shear in SESA is often weaker, suggesting a different threshold for tornadogenesis in this region.

Chapter 3 investigates how the MJO modulates the characteristics of summer convective storms across tropical and subtropical South America. In tropical South America, the MJO influence is significant and follows distinct patterns. MJO phases 8 and 1 are associated with large-scale upward motion and enhanced column moisture, leading to wider, shallower storms that produce greater volumetric rain. Conversely, phases 3, 4, and 5 are linked to anomalous downward motion and a drier, more unstable atmosphere, resulting in deeper, narrower storms that produce less overall rainfall but are more intense. In subtropical South America, the MJO's modulation of storm features is less clear but is linked to variations in the SALLJ, which alters moisture transport and the convective environment. This chapter established for the first time a clear connection between MJO activity and the physical structure of individual storm systems over the continent.

Chapter 4 projected future changes in extreme convection over South America using a high-resolution, convection-permitting climate simulation under the present climate, and a future climate simulation that used the pseudo-global warming approach under a SSP3-7.0 projected scenario from the CESM LENS2 ensemble mean. The simulation projects a future decrease in precipitation frequency over the western Amazon but an increase over eastern Brazil and Argentina, while precipitation intensity is expected to increase across most of the continent. The structure of storms is also projected to shift. The frequency of storms with intense, deep convective cores (specifically Deep Convective Cores and Deep and Wide Convective Cores) is projected to increase continent-wide, with these storms becoming larger and producing more total rainfall. This shift appears to be driven by a projected increase in CAPE across the continent, pointing towards a future with more intense and potentially more severe convective weather.

5.2 Future work and beyond…

The research developed in this dissertation has improved our understanding of the multiscale nature of convective storms in South America during the warm season and provides some hints about how storms might change in a warmer and wetter climate. However, there are still many potential avenues for future research to pursue.

In Chapter 2 it was evident that there is a lack of routine reporting of severe weather events across South America. Improving observation systems and encouraging routine collection of severe weather reports in South America are key to fostering more research in severe weather (Salio et al. 2024). Future studies using denser observational data and reports would provide new and improved insights into the convective environments that support tornadoes in SESA. Geographical differences between the U.S. Great Plains and SESA such as the taller and steeper Andes in comparison to the Rockies, could explain some of the observed differences in frequency and environments supporting tornadic storms in the United States versus SESA. Thus, these differences should be more carefully analyzed in future work, likely in numerical modeling simulations, to understand how contrasts in topography, moisture sources, or environmental parameters can influence the nature and evolution of tornadic storms on both continents (e.g., Li et al. 2024). Finally, the exploration of new sources of predictability from tropical teleconnections and elsewhere may also be extremely useful for providing early weather outlooks to emergency management agencies to prepare the population for severe weather threats.

In Chapter 3, it was found that the MJO modulation of certain storm structures in the western tropics was not as clear as the strong relationship found for the central and eastern tropics. Finding an explanation for this spatial difference in the MJO modulation would be an interesting topic to pursue in future research. We hypothesize that there might be some local interference the MJO equatorial propagation signal caused by the tropical Andes, but this needs to be tested with, for example, model experiments that modulate the topography and examine how the dynamics change during MJO-induced equatorial propagation events. It would also be interesting to explore whether similar MJO modulations are present during austral spring or fall, when the frequency or intensity of convective activity would be different than in austral summer for both tropical and subtropical South America. Additionally, the CAPE – storm mode relationship observed in the Amazon aligns with similar relationships observed over portions of the tropical oceans (Morita et al. 2006; Virts and Houze 2015). A global analysis of the CAPE – storm structure relationship could provide further insight into the regional characteristics that are common in places that present similar storm mode modulations. Finally, expanding the TRMM observational record by integrating GPM observations utilizing Ku-band radar could be useful. Adding ten or more years of storms identified over South America would reduce the uncertainty in the MJO modulation of storm structures, especially in the subtropics where storms are less frequent.

In Chapter 4, a PGW simulation representing one future climate scenario is used to project future changes in the frequency and intensity of precipitation and extreme convective storms in

South America. Given the large spread in projected changes in precipitation over tropical South America shown by previous studies (e.g., Llopart et al. 2020), future work should seek techniques to account for natural variability while maintaining the storm-resolving resolution of such future scenarios. In addition, new simulations considering different emissions scenarios could further expand the range of possible future outcomes for convective storm changes in South America. Another important consideration is the fact that the SAAG simulations do not account for changes in land use, which are very important over regions such as the Amazon rainforest that have suffered dramatic anthropogenic changes in the last decades, and are projected to continue changing in the coming decades. The SAAG group is planning a new set of convection-permitting simulations that will consider a more realistic land use representation across the continent for both the present and current climate. This could alter the expected changes in precipitation and extreme convection presented in this study, but would ultimately provide a more trustworthy scenario for the future of convective storms in South America. In terms of the storm characteristics analyzed here, future work should refine the algorithms to identify individual storms and include storm tracking over time. This would allow the analysis of storm evolution, accounting for its duration and spatial propagation, which is another aspect that has not been addressed in either the present or future climate.

Collectively, this dissertation emphasizes the interconnectedness of atmospheric processes across scales and highlights the impact of different spatiotemporal processes can have on convective storms in South America. By linking storm structures and specific severe weather events such as tornadoes to large-scale climate drivers such as the MJO, this work provides a potential pathway for the subseasonal-to-seasonal prediction of severe weather risk, offering valuable lead times for emergency preparedness and risk mitigation. Investigating the nuanced interactions between topography, land surface processes, and storm evolution in a changing climate remains an important avenue for future research, promising to further refine our ability to predict and mitigate the impacts of high-impact weather in this vulnerable part of the world.

REFERENCES

Adams, D. K., and E. P. Souza, 2009: CAPE and Convective Events in the Southwest during the North American Monsoon. *Monthly Weather Review*, **137**, 83–98, https://doi.org/10.1175/2008MWR2502.1.

Alvarez, M. S., C. S. Vera, G. N. Kiladis, and B. Liebmann, 2016: Influence of the Madden Julian Oscillation on precipitation and surface air temperature in South America. *Clim Dyn*, **46**, 245–262, https://doi.org/10.1007/s00382-015-2581-6.

——, C. S. Vera, and G. N. Kiladis, 2017: MJO Modulating the Activity of the Leading Mode of Intraseasonal Variability in South America. *Atmosphere*, **8**, 232, https://doi.org/10.3390/atmos8120232.

Alves, L. M., R. Chadwick, A. Moise, J. Brown, and J. A. Marengo, 2021: Assessment of rainfall variability and future change in Brazil across multiple timescales. *International Journal of Climatology*, **41**, E1875–E1888, https://doi.org/10.1002/joc.6818.

Anderson, C. J., C. K. Wikle, and Q. Zhou, 2007: Population influences on tornado reports in the United States. *Wea. Forecasting*, **22**, 571–579. https://doi.org/10.1175/WAF997.1

Anderson-Frey, A. K., Y. P. Richardson, A. R. Dean, R. L. Thompson, and B. T. Smith, 2016: Investigation of near-storm environments for tornado events and warnings. *Wea. Forecasting*, **31(6)**, 1771-1790. https://doi.org/10.1175/WAF-D-16-0046.1

Anderson-Frey, A. K., Y. P. Richardson., A. R. Dean, R. L. Thompson., and B. T. Smith, 2017: Self-Organizing Maps for the Investigation of Tornadic Near-Storm Environments. *Wea. Forecasting*, **32**, 1467–1475, https://doi.org/10.1175/WAF-D-17-0034.1.

Baggett, C. F., K. M. Nardi., S. J. Childs, S. N. Zito, E. A. Barnes, and E. D. Maloney, 2018: Skillful Five Week Forecasts of Tornado and Hail Activity, J. *Geophy. Res. Atmos.*, **123**, 12,661–12,675. https://doi.org/10.1029/2018JD029059

Banacos, P. C., and M. L. Ekster, 2010: The Association of the Elevated Mixed Layer with Significant Severe Weather Events in the Northeastern United States. *Weather and Forecasting*, **25**, 1082–1102, https://doi.org/10.1175/2010WAF2222363.1.

Barnes, H. C., and R. A. Houze Jr., 2013: The precipitating cloud population of the Madden-Julian Oscillation over the Indian and west Pacific Oceans. *Journal of Geophysical Research: Atmospheres*, **118**, 6996–7023, https://doi.org/10.1002/jgrd.50375.

Barrett, B. S., J. F. Carrasco, and A. P. Testino, 2012: Madden–Julian Oscillation (MJO) Modulation of Atmospheric Circulation and Chilean Winter Precipitation. *Journal of Climate*, **25**, 1678–1688, https://doi.org/10.1175/JCLI-D-11-00216.1.

——, J. C. Marin, and M. Jacques-Coper, 2020: A multiscale analysis of the tornadoes of 30–31 May 2019 in south-central Chile. *Atmospheric Research*, **236**, 104811, https://doi.org/10.1016/j.atmosres.2019.104811.

Bettolli, M. L., and Coauthors, 2021: The CORDEX Flagship Pilot Study in southeastern South America: a comparative study of statistical and dynamical downscaling models in simulating daily extreme precipitation events. *Clim Dyn*, **56**, 1589–1608, https://doi.org/10.1007/s00382-020-05549-z.

Blumberg, W. G., K. T. Halbert, T. A. Supinie, P. T. Marsh, R. L. Thompson, and J. A. Hart, 2017: SHARPpy: An Open-Source Sounding Analysis Toolkit for the Atmospheric Sciences. *Bull. Amer. Meteor. Soc.*, **98**, 1625–1636, https://doi.org/10.1175/BAMS-D-15-00309.1.

Bouwer, L. M., 2019: Observed and Projected Impacts from Extreme Weather Events: Implications for Loss and Damage. *Loss and Damage from Climate Change: Concepts, Methods and Policy Options*, R. Mechler, L.M. Bouwer, T. Schinko, S. Surminski, and J. Linnerooth-Bayer, Eds., Springer International Publishing, 63–82, https://doi.org/10.1007/978-3-319-72026-5_3.

Bozkurt, D., M. Rojas, J. P. Boisier, and J. Valdivieso, 2018: Projected hydroclimate changes over Andean basins in central Chile from downscaled CMIP5 models under the low and high emission scenarios. *Climatic Change*, **150**, 131–147, https://doi.org/10.1007/s10584-018-2246-7.

Brooks, H. E., 2009: Proximity soundings for severe convection for Europe and the United States from reanalysis data. *Atmospheric Research*, **93**, 546–553, https://doi.org/10.1016/j.atmosres.2008.10.005.

Brooks, H. E., and J. Correia, 2018: Long-Term Performance Metrics for National Weather Service Tornado Warnings. *Weather and Forecasting*, **33**, 1501–1511, https://doi.org/10.1175/WAF-D-18-0120.1.

Brooks, H. E., and J. P. Craven, 2002: Database of proximity soundings for significant severe thunderstorms, 1957–1993. Preprints, *21st Conf. on Severe Local Storms*, San Antonio, TX, Amer. Meteor. Soc., 639–642.

Brooks, H. E., J. W. Lee, and J. P. Craven, 2003: The spatial distribution of severe thunderstorm and tornado environments from global reanalysis data. *Atmospheric Research*, **67–68**, 73–94, https://doi.org/10.1016/S0169-8095(03)00045-0.

Brotzge, J., and W. Donner, 2013: The Tornado Warning Process: A Review of Current Research, Challenges, and Opportunities. *Bulletin of the American Meteorological Society*, **94**, 1715–1733, https://doi.org/10.1175/BAMS-D-12-00147.1.

Bruick, Z. S., K. L. Rasmussen, A. K. Rowe, and L. A. McMurdie, 2019: Characteristics of Intense Convection in Subtropical South America as Influenced by El Niño–Southern Oscillation. *Monthly Weather Review*, **147**, 1947–1966, https://doi.org/10.1175/MWR-D-18-0342.1.

Bunkers, M., D. Barber, R. Thompson, R. Edwards, and J. Garner, 2014: Choosing a universal mean wind for supercell motion prediction. *J. Operational Meteor.*, **2**, 115–129, https://doi.org/10.15191/nwajom.2014.0211.

Carbajal, N., J. F. León-Cruz., L. F. Pineda-Martínez, J. Tuxpan-Vargas, and J. H. Gaviño-Rodríguez, 2019: Occurrence of Anticyclonic Tornadoes in a Topographically Complex Region of Mexico. *Adv. Meteorol.,* **2019**, 1–11, https://doi.org/10.1155/2019/2763153.

Carvalho, L. M. V., C. Jones, and B. Liebmann, 2004: The South Atlantic Convergence Zone: Intensity, Form, Persistence, and Relationships with Intraseasonal to Interannual Activity and Extreme Rainfall. *Journal of Climate*, **17**, 88–108, https://doi.org/10.1175/1520-0442(2004)017<0088:TSACZI>2.0.CO;2.

——, ——, and T. Ambrizzi, 2005: Opposite Phases of the Antarctic Oscillation and Relationships with Intraseasonal to Interannual Activity in the Tropics during the Austral Summer. *Journal of Climate*, **18**, 702–718, https://doi.org/10.1175/JCLI-3284.1.

Castro Cunningham, C. A., and I. F. De Albuquerque Cavalcanti, 2006: Intraseasonal modes of variability affecting the South Atlantic Convergence Zone. *International Journal of Climatology*, **26**, 1165–1180, https://doi.org/10.1002/joc.1309.

Cecil, D. J., and C. B. Blankenship, 2012: Toward a Global Climatology of Severe Hailstorms as Estimated by Satellite Passive Microwave Imagers. *Journal of Climate*, **25**, 687–703, https://doi.org/10.1175/JCLI-D-11-00130.1.

——, S. J. Goodman, D. J. Boccippio, E. J. Zipser, and S. W. Nesbitt, 2005: Three Years of TRMM Precipitation Features. Part I: Radar, Radiometric, and Lightning Characteristics. *Monthly Weather Review*, **133**, 543–566, https://doi.org/10.1175/MWR-2876.1.

Chen, J., A. Dai, Y. Zhang, and K. L. Rasmussen, 2020a: Changes in Convective Available Potential Energy and Convective Inhibition under Global Warming. *Journal of Climate*, **33**, 2025–2050, https://doi.org/10.1175/JCLI-D-19-0461.1.

Coffer, B. E., and M. D. Parker, 2015: Impacts of increasing low-level shear on supercells during the early evening transition. *Mon. Wea. Rev.*, **143**, 1945–1969, https://doi.org/10.1175/MWR-D-14-00328.1.

Coffer, B. E., M. D. Parker, R. L. Thompson, B. T. Smith, and R. E. Jewell, 2019: Using near-ground storm relative helicity in supercell tornado forecasting. *Wea. Forecasting*, **34(5)**, 1417–1435. https://doi.org/10.1175/WAF-D-19-0115.1

Coffer, B. E., M. Taszarek, and M. D. Parker, 2020: Near-Ground Wind Profiles of Tornadic and Nontornadic Environments in the United States and Europe from ERA5 Reanalyses. *Weather and Forecasting*, **35**, 2621–2638, https://doi.org/10.1175/WAF-D-20-0153.1.

Craven, J., R. Jewell, and H. E. Brooks, 2002: Comparison between observed convective cloud-base heights and lifting condensation level for two different lifted parcels. *Wea. Forecasting*, **17**, 885–890. https://doi.org/10.1175/1520-0434(2002)017<0885:CBOCCB>2.0.CO;2

Davis, J. M., and M. D. Parker, 2014: Radar Climatology of Tornadic and Nontornadic Vortices in High-Shear, Low-CAPE Environments in the Mid-Atlantic and Southeastern United

States. *Wea. Forecasting*, **11(4)**, 560-581. https://doi.org/10.1175/1520-0434(1996)011<0560:FFFAIB>2.0.CO;2

De Souza, E. B., and T. Ambrizzi, 2006: Modulation of the intraseasonal rainfall over tropical Brazil by the Madden–Julian oscillation. *International Journal of Climatology*, **26**, 1759–1776, https://doi.org/10.1002/joc.1331.

DNM, 2002: Tornado in the Department of Canelones (Uruguay), on March 10th, 2002, DNM, Montevideo, Uruguay, 4 pp. (in Spanish).

Dominguez, F., and Coauthors, 2024: Advancing South American Water and Climate Science through Multidecadal Convection-Permitting Modeling. *Bulletin of the American Meteorological Society*, **105**, E32–E44, https://doi.org/10.1175/BAMS-D-22-0226.1.

Doswell, C. A., H. E. Brooks, and R. A. Maddox, 1996: Flash flood forecasting: An ingredients-based methodology. *Wea. Forecasting,* **11(4)**, 560-581. https://doi.org/10.1175/1520-0434(1996)011<0560:FFFAIB>2.0.CO;2

Douville, H., and Coauthors, 2021: Water cycle changes. *Climate Change 2021: The Physical Science Basis. Contribution of Working Group I to the Sixth Assessment Report of the Intergovernmental Panel on Climate Change*, V. Masson-Delmotte et al., Eds., Cambridge University Press, 1055–1210, https://doi.org/10.1017/9781009157896.001.

Durañona, V., 2016: Extreme wind climate of Uruguay. Ph.D. Dissertation. Universidad de la Republica, Montevideo, Uruguay. https://www.colibri.udelar.edu.uy/jspui/handle/20.500.12008/8394

Emanuel, K. A., 1994: *Atmospheric Convection*. Oxford University Press, 580 pp.

Falvey, M., and R. Garreaud, 2007: Wintertime Precipitation Episodes in Central Chile: Associated Meteorological Conditions and Orographic Influences. *Journal of Hydrometeorology*, **8**, 171–193, https://doi.org/10.1175/JHM562.1.

Feng, Z., and Coauthors, 2021: A Global High-Resolution Mesoscale Convective System Database Using Satellite-Derived Cloud Tops, Surface Precipitation, and Tracking. *JGR Atmospheres*, **126**, https://doi.org/10.1029/2020JD034202.

Ferreira, G. W. S., and M. S. Reboita, 2022: A New Look into the South America Precipitation Regimes: Observation and Forecast. *Atmosphere*, **13**, 873, https://doi.org/10.3390/atmos13060873.

Fischer, E. M., and R. Knutti, 2016: Observed heavy precipitation increase confirms theory and early models. *Nature Clim Change*, **6**, 986–991, https://doi.org/10.1038/nclimate3110.

Fu, Y., and Q. Wu, 2024: Recent Emerging Shifts in Precipitation Intensity and Frequency in the Global Tropics Observed by Satellite Precipitation Data Sets. *Geophysical Research Letters*, **51**, e2023GL107916, https://doi.org/10.1029/2023GL107916.

Fujita, T. T., 1971: Proposed characterization of tornadoes and hurricanes by area and intensity. SMRP Research Paperv91, University of Chicago, Chicago, IL, 42 pp. [Available from Wind Engineering Research Center, Box 41023, Lubbock, TX 79409.]

Garreaud, R. D., and J. M. Wallace, 1998: Summertime Incursions of Midlatitude Air into Subtropical and Tropical South America. *Mon. Wea. Rev.*, **126**, 2713–2733, https://doi.org/10.1175/1520-0493(1998)126<2713:SIOMAI>2.0.CO;2.

Gibbs, J. G., 2021: Evaluating Precursor Signals for QLCS Tornado and Higher Impact Straight-Line Wind Events. *J. Operational Meteor.*, 62–75, https://doi.org/10.15191/nwajom.2021.0905.

Giangrande, S. E., T. S. Biscaro, and J. M. Peters, 2023: Seasonal controls on isolated convective storm drafts, precipitation intensity, and life cycle as observed during GoAmazon2014/5. *Atmos. Chem. Phys.*, **23**, 5297–5316, https://doi.org/10.5194/acp-23-5297-2023.

Giles, J. A., R. C. Ruscica, and C. G. Menéndez, 2020: The diurnal cycle of precipitation over South America represented by five gridded datasets. *International Journal of Climatology*, **40**, 668–686, https://doi.org/10.1002/joc.6229.

Goliger, A. M., and R. V. Milford, 1998: A review of worldwide occurrence of tornadoes. *Journal of Wind Engineering and Industrial Aerodynamics*, **74–76**, 111–121, https://doi.org/10.1016/S0167-6105(98)00009-9.

Grams, J. S., R. L. Thompson, D. V. Snively, J. A. Prentice., G. M. Hodges., and L. J. Reames, 2012: A climatology and comparison of parameters for significant tornado events in the United States. *Wea. Forecasting*, **27(1)**, 106-123. https://doi.org/10.1175/WAF-D-11-00008.1

Grimm, A. M., 2019: Madden–Julian Oscillation impacts on South American summer monsoon season: precipitation anomalies, extreme events, teleconnections, and role in the MJO cycle. *Clim Dyn*, **53**, 907–932, https://doi.org/10.1007/s00382-019-04622-6.

——, and T. Ambrizzi, 2009: Teleconnections into South America from the tropics and extratropics on interannual and intraseasonal timescales. *Past climate variability in South America and surrounding regions: from the last glacial maximum to the holocene*, 159–191.

Grimm, A. M., and R. G. Tedeschi, 2009: ENSO and Extreme Rainfall Events in South America. *J. Climate*, **22**, 1589-1609. https://doi.org/10.1175/2008JCLI2429.1

Guyer, J. L., and A. R. Dean, 2010: Tornadoes within weak CAPE environments across the continental United States. Preprints, 25th Conf. on Severe Local Storms, Denver, CO, Amer. Meteor. Soc., 1.5. [Available online at https://ams.confex.com/ams/pdfpapers/175725.pdf]

Halladay, K., R. Kahana, B. Johnson, C. Still, G. Fosser, and L. Alves, 2023: Convection-permitting climate simulations for South America with the Met Office Unified Model. *Clim Dyn*, **61**, 5247–5269, https://doi.org/10.1007/s00382-023-06853-0.

Hamill, T. M., R. S. Schneider, H. E. Brooks, G., S. Forbes, H. B. Bluestein, M. Steinberg, D. Melendez., and R. M. Dole, 2005: The May 2003 extended tornado outbreak. *Bull. Amer. Meteor. Soc*, **86(4),** 531–542. https://doi.org/10.1175/BAMS-86-4-531.

Held, I. M., and B. J. Soden, 2006: Robust Responses of the Hydrological Cycle to Global Warming. *Journal of Climate*, **19**, 5686–5699, https://doi.org/10.1175/JCLI3990.1.

Hersbach, H., and Coauthors, 2020: The ERA5 global reanalysis. *Quarterly Journal of the Royal Meteorological Society*, **146**, 1999–2049, https://doi.org/10.1002/qj.3803.

Holloway, C. E., and J. D. Neelin, 2009: Moisture Vertical Structure, Column Water Vapor, and Tropical Deep Convection. *Journal of the Atmospheric Sciences*, **66**, 1665–1683, https://doi.org/10.1175/2008JAS2806.1.

Hou, A. Y., and Coauthors, 2014: The Global Precipitation Measurement Mission. *Bulletin of the American Meteorological Society*, **95**, 701–722, https://doi.org/10.1175/BAMS-D-13-00164.1.

Houze, R. A., Jr., 2004: Mesoscale convective systems. *Rev. Geophys*., **42**, 10.1029/2004RG000150, 43 pp.

Houze, R. A., K. L. Rasmussen, M. D. Zuluaga, and S. R. Brodzik, 2015: The variable nature of convection in the tropics and subtropics: A legacy of 16 years of the Tropical Rainfall Measuring Mission satellite. *Reviews of Geophysics*, **53**, 994–1021, https://doi.org/10.1002/2015RG000488.

Hudson, J., and E. Maloney, 2023: The Role of Surface Fluxes in MJO Propagation through the Maritime Continent. *Journal of Climate*, **36**, 1633–1652, https://doi.org/10.1175/JCLI-D-22-0484.1.

IPCC, 2012: *Managing the Risks of Extreme Events and Disasters to Advance Climate Change Adaptation*. A Special Report of Working Groups I and II of the Intergovernmental Panel on Climate Change [Field, C.B., V. Barros, T.F. Stocker, D. Qin, D.J. Dokken, K.L. Ebi, M.D. Mastrandrea, K.J. Mach, G.-K. Plattner, S.K. Allen, M. Tignor, and P.M. Midgley (eds.)]. Cambridge University Press, Cambridge, UK, and New York, NY, USA, 582 pp.

Jacques-Coper, M., D. Veloso-Aguila, C. Segura, and A. Valencia, 2021: Intraseasonal teleconnections leading to heat waves in central Chile. *International Journal of Climatology*, **41**, 4712–4731, https://doi.org/10.1002/joc.7096.

Jaramillo, L., G. Poveda, and J. F. Mejía, 2017: Mesoscale convective systems and other precipitation features over the tropical Americas and surrounding seas as seen by TRMM. *Intl Journal of Climatology*, **37**, 380–397, https://doi.org/10.1002/joc.5009.

Jones, C., Y. Mu, L. M. V. Carvalho, and Q. Ding, 2023: The South America Low-Level Jet: form, variability and large-scale forcings. *npj Clim Atmos Sci*, **6**, 1–11, https://doi.org/10.1038/s41612-023-00501-4.

Jorgensen, D. P., and T. M. Weckwerth, 2003: Forcing and organization of convective systems. Radar and Atmospheric Science: A Collection of Essays in Honor of David Atlas, *Meteor. Monogr.*, **52**, Amer. Meteor. Soc., 75–103. https://doi.org/10.1175/0065-9401(2003)030<0075:FAOOCS>2.0.CO;2.

Kahana, R., K. Halladay, L. M. Alves, R. Chadwick, and A. J. Hartley, 2024: Future precipitation projections for Brazil and tropical South America from a convection-permitting climate simulation. *Front. Clim.*, **6**, https://doi.org/10.3389/fclim.2024.1419704.

Kennedy, P. C., N. E. Westcott, and R. W. Scott, 1993: Single-Doppler Radar Observations of a Mini-Supercell Tornadic Thunderstorm. *Mon. Wea. Rev.*, ***121*(6)**, 1860-1870. https://doi.org/10.1175/1520-0493(1993)121<1860:SDROOA>2.0.CO;2

Kiladis, G. N., K. H. Straub, and P. T. Haertel, 2005: Zonal and Vertical Structure of the Madden–Julian Oscillation. *Journal of the Atmospheric Sciences*, **62**, 2790–2809, https://doi.org/10.1175/JAS3520.1.

Kim, H., F. Vitart, and D. E. Waliser, 2018: Prediction of the Madden–Julian Oscillation: A Review. *Journal of Climate*, **31**, 9425–9443, https://doi.org/10.1175/JCLI-D-18-0210.1.

Knapp, K. R., A. H. Young, H. Semunegus, A. K. Inamdar, and W. Hankins, 2021: Adjusting ISCCP Cloud Detection to Increase Consistency of Cloud Amount and Reduce Artifacts. *J Atmos Ocean Technol*, **38**, 155–165, https://doi.org/10.1175/JTECH-D-20-0045.1.

Knupp, K. R., and Coauthors, 2014: Meteorological overview of the devastating 27 April 2011 tornado outbreak. *Bull. Amer. Meteor. Soc.*, **95(7)**, 1041–1062. https://doi.org/10.1175/BAMS-D-11-00229.1

Kummerow, C., W. Barnes, T. Kozu, J. Shiue, and J. Simpson, 1998: The Tropical Rainfall Measuring Mission (TRMM) Sensor Package. *Journal of Atmospheric and Oceanic Technology*, **15**, 809–817, https://doi.org/10.1175/1520-0426(1998)015<0809:TTRMMT>2.0.CO;2.

Li, F., D. R. Chavas, B. Medeiros, K. A. Reed, and K. L. Rasmussen, 2024: Upstream surface roughness and terrain are strong drivers of contrast in tornado potential between North and South America. *Proceedings of the National Academy of Sciences*, **121**, e2315425121, https://doi.org/10.1073/pnas.2315425121.

Liebmann, B., G. N. Kiladis, J. Marengo, T. Ambrizzi, and J. D. Glick, 1999: Submonthly Convective Variability over South America and the South Atlantic Convergence Zone. *Journal of Climate*, **12**, 1877–1891, https://doi.org/10.1175/1520-0442(1999)012<1877:SCVOSA>2.0.CO;2.

Liebmann B., and C.A. Smith, 1996: Description of a Complete (Interpolated) Outgoing Longwave Radiation Dataset. *Bull. Amer. Meteor. Soc.*, **77**, 1275-1277. http://www.jstor.org/stable/26233278

Lima, J. S., 1982: Analysis of a funnel-cloud occurrence in Santa Maria, Rio Grande do Sul: Application of a forecasting method (in Portuguese). *Proc. Second Brazilian Congress on Meteorology*, Pelotas, Brazil, Braz. Meteor. Soc., 382–392.

Liu, C., and E. Zipser, 2013: Regional variation of morphology of organized convection in the tropics and subtropics. *JGR Atmospheres*, **118**, 453–466, https://doi.org/10.1029/2012JD018409.

——, and E. J. Zipser, 2015: The global distribution of largest, deepest, and most intense precipitation systems. *Geophysical Research Letters*, **42**, 3591–3595, https://doi.org/10.1002/2015GL063776.

——, ——, D. J. Cecil, S. W. Nesbitt, and S. Sherwood, 2008: A Cloud and Precipitation Feature Database from Nine Years of TRMM Observations. *Journal of Applied Meteorology and Climatology*, **47**, 2712–2728, https://doi.org/10.1175/2008JAMC1890.1.

Liu, P., Q. Zhang, C. Zhang, Y. Zhu, M. Khairoutdinov, H.-M. Kim, C. Schumacher, and M. Zhang, 2016: A revised real-time multivariate MJO index. Mon. Wea. Rev., 144, 627–642, https://doi.org/10.1175/MWR-D-15-0237.1.

Llopart, M., M. Simões Reboita, and R. Porfírio da Rocha, 2020: Assessment of multi-model climate projections of water resources over South America CORDEX domain. *Clim Dyn*, **54**, 99–116, https://doi.org/10.1007/s00382-019-04990-z.

Lopes, M. M., 2020: Discriminando condições favoráveis a diferentes modos de tempo severo no leste da Bacia do Prata (in Portuguese). Master of Science Thesis, Universidade Federal de Santa Maria, Brazil, 122 pp, https://repositorio.ufsm.br/handle/1/22344?locale-attribute=pt_BR

Lopes, M. M., and E. L. Nascimento, 2020: Use of remote sensing via satellite in the identification of tornado damage paths in a severe weather event in Rio Grande do Sul. *Ciência E Natura*, **42**, e8. https://doi.org/10.5902/2179460X55309

López-Franca, N., P. Zaninelli, A. Carril, C. Menéndez, and E. Sánchez, 2016: Changes in temperature extremes for 21st century scenarios over South America derived from a multi-model ensemble of regional climate models. *Clim. Res.*, **68**, 151–167, https://doi.org/10.3354/cr01393.

Ma, H.-Y., X. Ji, J. D. Neelin, and C. R. Mechoso, 2011: Mechanisms for Precipitation Variability of the Eastern Brazil/SACZ Convective Margin. *Journal of Climate*, **24**, 3445–3456, https://doi.org/10.1175/2011JCLI4070.1.

Madden, R. A., and P. R. Julian, 1971: Detection of a 40–50 Day Oscillation in the Zonal Wind in the Tropical Pacific. *Journal of the Atmospheric Sciences*, **28**, 702–708, https://doi.org/10.1175/1520-0469(1971)028<0702:DOADOI>2.0.CO;2.

——, and ——, 1972: Description of Global-Scale Circulation Cells in the Tropics with a 40–50 Day Period. *Journal of the Atmospheric Sciences*, **29**, 1109–1123, https://doi.org/10.1175/1520-0469(1972)029<1109:DOGSCC>2.0.CO;2.

Maddox, R., 1976: An evaluation of tornado proximity wind and stability data. *Mon. Wea. Rev.*, **104**, 133–142, https://doi.org/10.1175/1520-0493(1976)104<0133:AEOTPW>2.0.CO;2.

Mamalakis, A., and Coauthors, 2021: Zonally contrasting shifts of the tropical rainbelt in response to climate change. *Nat Clim Chang*, **11**, 143–151, https://doi.org/10.1038/s41558-020-00963-x.

Marengo, J. A., W. R. Soares., C. Saulo, and M. Nicolini, 2004: Climatology of the low-level jet east of the Andes as derived from the NCEP–NCAR reanalyses: Characteristics and temporal variability. *J. Climate*, **17**, 2261–2280, https://doi.org/10.1175/1520-0442(2004)017<2261:COTLJE>2.0.CO;2.

Markowski, P., C. Hannon, J. Frame, E. Lancaster, A. Pietrycha, R. Edwards, and R. L. Thompson, 2003: Characteristics of vertical wind profiles near supercells obtained from the Rapid Update Cycle. *Wea. Forecasting*, **18(6)**, 1262-1272. https://doi.org/10.1175/1520-0434(2003)018<1262:COVWPN>2.0.CO;2

Markowski, P. M., and Y. P. Richardson, 2009: Tornadogenesis: Our current understanding, forecasting considerations, and questions to guide future research. *Atmos. Res.*, **93,** 3–10. https://doi.org/10.1016/j.atmosres.2008.09.015

Markowski, P. M., J. M. Straka, E. N. Rasmussen, and D. O. Blanchard, 1998: Variability of storm-relative helicity during VORTEX. *Mon. Wea. Rev.*, **126(11),** 2959-2971. https://doi.org/10.1175/1520-0493(1998)126<2959:VOSRHD>2.0.CO;2

Matthews, A. J., 2000: Propagation mechanisms for the Madden-Julian Oscillation. *Quarterly Journal of the Royal Meteorological Society*, **126**, 2637–2651, https://doi.org/10.1002/qj.49712656902.

Mayta, V. C., T. Ambrizzi, J. C. Espinoza, and P. L. Silva Dias, 2019: The role of the Madden–Julian oscillation on the Amazon Basin intraseasonal rainfall variability. *International Journal of Climatology*, **39**, 343–360, https://doi.org/10.1002/joc.5810.

McBride, J. L., and W. M. Frank, 1999: Relationships between Stability and Monsoon Convection. *Journal of the Atmospheric Sciences*, **56**, 24–36, https://doi.org/10.1175/1520-0469(1999)056<0024:RBSAMC>2.0.CO;2.

Mercer, A. E., C. M. Shafer, C. A. Doswell, L. M. Leslie, and M. B. Richman, 2012: Synoptic composites of tornadic and nontornadic outbreaks. *Mon. Wea. Rev.*, **137(12)**, 4355–4368. https://doi.org/10.1175/2009MWR2897.1

Miller, P. W., and T. L. Mote, 2017: A Climatology of Weakly Forced and Pulse Thunderstorms in the Southeast United States. *Journal of Applied Meteorology and Climatology*, **56**, 3017–3033, https://doi.org/10.1175/JAMC-D-17-0005.1.

Milliff, R. F., and R. A. Madden, 1996: The Existence and Vertical Structure of Fast, Eastward-Moving Disturbances in the Equatorial Troposphere. *J. Atmos. Sci.*, **53**, 586–597, https://doi.org/10.1175/1520-0469(1996)053<0586:TEAVSO>2.0.CO;2.

Mo, K. C., and R. W. Higgins, 1998: The Pacific–South American Modes and Tropical Convection during the Southern Hemisphere Winter. *Monthly Weather Review*, **126**, 1581–1596, https://doi.org/10.1175/1520-0493(1998)126<1581:TPSAMA>2.0.CO;2.

——, and J. N. Paegle, 2001: The Pacific–South American modes and their downstream effects. *International Journal of Climatology*, **21**, 1211–1229, https://doi.org/10.1002/joc.685.

Montini, T. L., C. Jones, and L. M. V. Carvalho, 2019: The South American Low-Level Jet: A New Climatology, Variability, and Changes. *Journal of Geophysical Research: Atmospheres*, **124**, 1200–1218, https://doi.org/10.1029/2018JD029634.

Morita, J., Y. N. Takayabu, S. Shige, and Y. Kodama, 2006: Analysis of rainfall characteristics of the Madden–Julian oscillation using TRMM satellite data. *Dynamics of Atmospheres and Oceans*, **42**, 107–126, https://doi.org/10.1016/j.dynatmoce.2006.02.002.

Mulholland, J. P., S. W. Nesbitt, and R. J. Trapp, 2019: A Case Study of Terrain Influences on Upscale Convective Growth of a Supercell. *Mon. Wea. Rev.,* **147**, 4305–4324, https://doi.org/10.1175/MWR-D-19-0099.1.

Mulholland, J. P., S. W. Nesbitt, R. J. Trapp, K. L. Rasmussen, and P. V. Salio, 2018: Convective storm life cycle and environments near the Sierras de Cordoba, Argentina. *Mon. Wea. Rev.*, **146**, 2541–2557, https://doi.org/10.1175/MWR-D-18-0081.1.

Nascimento, E. L., and C. A. Doswell III, 2006: The need for an improved documentation of severe thunderstorms and tornadoes in South America. *Symposium on the challenges of severe convective storms*. 86th Annual Meeting Atlanta, (GA). Amer. Meteor. Soc.

Nascimento, E. L., G. Held, and A. M. Gomes, 2014: A Multiple-Vortex Tornado in Southeastern Brazil, *Mon. Wea. Rev.*, **142**, 3017-3037, https://doi.org/10.1175/MWR-D-13-00319.1.

Nascimento, M. G. do, D. L. Herdies, and D. O. de Souza, 2016: The South American Water Balance: The Influence of Low-Level Jets. *Journal of Climate*, **29**, 1429–1449, https://doi.org/10.1175/JCLI-D-15-0065.1.

Natalini, B., J. L. Lassig., M. B. Natalini, and C. Palese, 2012: Wind-induced damage in two regions of Argentina. *J. Civil Eng. Archit.*, **6(2)**, 167.

Nesbitt, S. W., and Coauthors, 2021: A Storm Safari in Subtropical South America: Proyecto RELAMPAGO, *Bull. Amer. Meteor. Soc.*, **102(8)**, E1621-E1644. https://doi.org/10.1175/BAMS-D-20-0029.1

Nesbitt, S. W., E. J. Zipser, and D. J. Cecil, 2000: A Census of Precipitation Features in the Tropics Using TRMM: Radar, Ice Scattering, and Lightning Observations. *Journal of Climate*, **13**, 4087–4106, https://doi.org/10.1175/1520-0442(2000)013<4087:ACOPFI>2.0.CO;2.

Nogués-Paegle, J., and K. C. Mo, 1997: Alternating Wet and Dry Conditions over South America during Summer. *Monthly Weather Review*, **125**, 279–291, https://doi.org/10.1175/1520-0493(1997)125<0279:AWADCO>2.0.CO;2.

Nouri, N., N. Devineni, V. Were, and R. Khanbilvardi, 2021: Explaining the trends and variability in the United States tornado records using climate teleconnections and shifts in observational practices. *Sci Rep*, **11**, 1741, https://doi.org/10.1038/s41598-021-81143-5.

Nunes, L. H., L. De Bona, and D. H. Candido, 2011: Tornado and waterspout climatology in Brazil. *6th European Conference on Severe Storms (ECSS 2011)*, Palma de Mallorca. https://citeseerx.ist.psu.edu/viewdoc/download?doi=10.1.1.686.9041&rep=rep1&type=pdf

Nunes, L. H., G. Held, A. M. Gomes, K. P. Naccarato, and R. R. Amorim, 2021: Analysis of the Campinas tornado (Brazil) in June 2016: damage track, radar characteristics and lightning observations of the supercell, *Weather Clim. Dynam. Discuss*. [preprint]. https://doi.org/10.5194/wcd-2021-35.

Oliveira, I. P. V., 2004: Analysis of tornado events in Santa Catarina (Brazil): synoptic characterization and evaluation of data, INPE - National Institute of Space Research, Sao Jose dos Campos, Brazil, 225 pp. (in Portuguese).

Oliveira, M. I., F. S. Puhales, E. L. Nascimento, and V. Anabor, 2022: Integrated damage, visual, remote sensing, and environmental analysis of a strong tornado in southern Brazil. *Atmospheric Research*, 106188. https://doi.org/10.1016/j.atmosres.2022.106188

Ortiz-Royero, J. C., and M. Rosales, 2012: Severe tornadoes on the Caribbean coast of Colombia since 2001 and their relation to local climate conditions. *Nat. Hazards.,* **64**, 1805–1821. https://doi.org/10.1007/s11069-012-0337-8

Parker, M. D., 2014: Composite VORTEX2 Supercell Environments from Near-Storm Soundings. *Mon. Wea. Rev.*, **142**, 508–529, https://doi.org/10.1175/MWR-D-13-00167.1.

Pabón-Caicedo, J. D., and Coauthors, 2020: Observed and Projected Hydroclimate Changes in the Andes. *Front. Earth Sci.*, **8**, https://doi.org/10.3389/feart.2020.00061.

Paccini, L., and B. Stevens, 2023: Assessing Precipitation Over the Amazon Basin as Simulated by a Storm-Resolving Model. *Journal of Geophysical Research: Atmospheres*, **128**, e2022JD037436, https://doi.org/10.1029/2022JD037436.

Pachauri, R. K., L. Mayer, and Intergovernmental Panel on Climate Change, eds., 2015: *Climate change 2014: synthesis report*. Intergovernmental Panel on Climate Change 151pp.

Paegle, J. N., L. A. Byerle, and K. C. Mo, 2000: Intraseasonal Modulation of South American Summer Precipitation. *Monthly Weather Review*, **128**, 837–850, https://doi.org/10.1175/1520-0493(2000)128<0837:IMOSAS>2.0.CO;2.

Panasawatwong, W., K. L. Rasmussen, and M. M. Bell, 2022: A Climatology of Extreme Convective Storms in Tropical and Subtropical East Asia and Their Ingredients for Heavy Rainfall as Seen by TRMM. *Journal of Geophysical Research: Atmospheres*, **127**, e2022JD036863, https://doi.org/10.1029/2022JD036863.

Pascale, S., L. M. V. Carvalho, D. K. Adams, C. L. Castro, and I. F. A. Cavalcanti, 2019: Current and Future Variations of the Monsoons of the Americas in a Warming Climate. *Curr Clim Change Rep*, **5**, 125–144, https://doi.org/10.1007/s40641-019-00135-w.

Petersen, W. A., R. Cifelli, D. J. Boccippio, S. A. Rutledge, and C. Fairall, 2003: Convection and Easterly Wave Structures Observed in the Eastern Pacific Warm Pool during EPIC-2001. *Journal of the Atmospheric Sciences*, **60**, 1754–1773, https://doi.org/10.1175/1520-0469(2003)060<1754:CAEWSO>2.0.CO;2.

Pereira Filho, A. J., F. Vemado, and H. A. Karam, 2019: Evidence of Tornadoes and Microbursts in Sao Paulo State, Brazil: A Synoptic and Mesoscale Analysis. *Pure Appl. Geophys.*, **176**, 5079–5106. https://doi.org/10.1007/s00024-019-02276-3

Piersante, J. O., K. L. Rasmussen, R. S. Schumacher, A. K. Rowe, and L. A. McMurdie, 2021: A Synoptic Evolution Comparison of the Smallest and Largest MCSs in Subtropical South America between Spring and Summer. *Monthly Weather Review*, **149**, 1943–1966, https://doi.org/10.1175/MWR-D-20-0208.1.

Pita, G. L., and M. L. A. Schwarzkopf, 2016: Urban downburst vulnerability and damage assessment from a case study in Argentina. *Nat. Hazards*, **83**, 445–463. https://doi.org/10.1007/s11069-016-2323-z

Polade, S. D., A. Gershunov, D. R. Cayan, M. D. Dettinger, and D. W. Pierce, 2017: Precipitation in a warming world: Assessing projected hydro-climate changes in California and other Mediterranean climate regions. *Sci Rep*, **7**, 10783, https://doi.org/10.1038/s41598-017-11285-y.

Potvin, C. K., C. Broyles, P. S. Skinner, and H. E. Brooks, 2022: Improving Estimates of U.S. Tornado Frequency by Accounting for Unreported and Underrated Tornadoes. *Journal of Applied Meteorology and Climatology*, **61**, 909–930, https://doi.org/10.1175/JAMC-D-21-0225.1.

Powell, S. W., and R. A. Houze Jr., 2013: The cloud population and onset of the Madden-Julian Oscillation over the Indian Ocean during DYNAMO-AMIE. *Journal of Geophysical Research: Atmospheres*, **118**, 11,979-11,995, https://doi.org/10.1002/2013JD020421.

Prein, A. F., and Coauthors, 2015: A review on regional convection-permitting climate modeling: Demonstrations, prospects, and challenges. *Reviews of Geophysics*, **53**, 323–361, https://doi.org/10.1002/2014RG000475.

——, C. Liu, K. Ikeda, S. B. Trier, R. M. Rasmussen, G. J. Holland, and M. P. Clark, 2017: Increased rainfall volume from future convective storms in the US. *Nature Clim Change*, **7**, 880–884, https://doi.org/10.1038/s41558-017-0007-7.

——, and Coauthors, 2024: Km-Scale Simulations of Mesoscale Convective Systems Over South America—A Feature Tracker Intercomparison. *Journal of Geophysical Research: Atmospheres*, **129**, e2023JD040254, https://doi.org/10.1029/2023JD040254.

Rasmussen, E. N., and D. O. Blanchard, 1998: A baseline climatology of sounding-derived supercell and tornado forecast parameters. *Wea. Forecasting*, **13(4)**, 1148-1164. https://doi.org/10.1175/1520-0434(1998)013<1148:ABCOSD>2.0.CO;2

Rasmussen, K. L., and R. A. Houze, 2011: Orogenic Convection in Subtropical South America as Seen by the TRMM Satellite. *Monthly Weather Review*, **139**, 2399–2420, https://doi.org/10.1175/MWR-D-10-05006.1.

Rasmussen, K. L., and R. A. Houze, 2016: Convective Initiation near the Andes in Subtropical South America. *Monthly Weather Review*, **144**, 2351–2374, https://doi.org/10.1175/MWR-D-15-0058.1.

Rasmussen, K. L., M. D. Zuluaga, and R. A. Houze, 2014: Severe convection and lightning in subtropical South America. *Geophysical Research Letters*, **41**, 7359–7366, https://doi.org/10.1002/2014GL061767.

Rasmussen, K. L., M. M. Chaplin, M. D. Zuluaga, and R. A. Houze, 2016: Contribution of Extreme Convective Storms to Rainfall in South America. *Journal of Hydrometeorology*, **17**, 353–367, https://doi.org/10.1175/JHM-D-15-0067.1.

Ray, P. S., P. Bieringer, X. Niu., and B. Whissel, 2003: An improved estimate of tornado occurrence in the central plains of the United States. *Mon. Wea. Rev.*, **131**, 1026–1031. https://doi.org/10.1175/1520-0493(2003)131<1026:AIEOTO>2.0.CO;2

Raymond, D. J., Ž. Stone, and S. Sentić, 2024: Rains and Showers in OTREC; Weak Temperature Gradient Modeling. *Journal of Advances in Modeling Earth Systems*, **16**, e2023MS003980, https://doi.org/10.1029/2023MS003980.

Rehbein, A., and Coauthors, 2018: Severe weather events over Southeastern Brazil during the 2016 dry season. *Adv. Meteorol.*, **2018**, 4878503. https://doi.org/10.1155/2018/4878503

Reboita, M. S., C. A. C. Kuki, V. H. Marrafon, C. A. de Souza, G. W. S. Ferreira, T. Teodoro, and J. W. M. Lima, 2022a: South America climate change revealed through climate indices projected by GCMs and Eta-RCM ensembles. *Clim Dyn*, **58**, 459–485, https://doi.org/10.1007/s00382-021-05918-2.

——, R. P. da Rocha, C. A. de Souza, T. C. Baldoni, P. L. L. da S. Silva, and G. W. S. Ferreira, 2022b: Future Projections of Extreme Precipitation Climate Indices over South America Based on CORDEX-CORE Multimodel Ensemble. *Atmosphere*, **13**, 1463, https://doi.org/10.3390/atmos13091463.

Recalde-Coronel, G. C., B. Zaitchik, and W. K. Pan, 2020: Madden–Julian oscillation influence on sub-seasonal rainfall variability on the west of South America. *Clim Dyn*, **54**, 2167–2185, https://doi.org/10.1007/s00382-019-05107-2.

Ribeiro, B. Z., and L. F. Bosart, 2018: Elevated Mixed Layers and Associated Severe Thunderstorm Environments in South and North America. *Monthly Weather Review*, **146**, 3–28, https://doi.org/10.1175/MWR-D-17-0121.1.

Rickenbach, T. M., R. N. Ferreira, J. B. Halverson, D. L. Herdies, and M. A. F. Silva Dias, 2002: Modulation of convection in the southwestern Amazon basin by extratropical stationary fronts. *Journal of Geophysical Research: Atmospheres*, **107**, LBA 7-1-LBA 7-13, https://doi.org/10.1029/2000JD000263.

Riley, E. M., B. E. Mapes, and S. N. Tulich, 2011: Clouds Associated with the Madden–Julian Oscillation: A New Perspective from CloudSat. *Journal of the Atmospheric Sciences*, **68**, 3032–3051, https://doi.org/10.1175/JAS-D-11-030.1.

da Rocha, R. P., C. A. Morales, S. V. Cuadra, and T. Ambrizzi, 2009: Precipitation diurnal cycle and summer climatology assessment over South America: An evaluation of Regional Climate Model version 3 simulations. *Journal of Geophysical Research: Atmospheres*, **114**, https://doi.org/10.1029/2008JD010212.

Rocque, M. N., and K. L. Rasmussen, 2022: The Impact of Topography on the Environment and Lifecycle of Weakly- and Strongly-forced MCSs during RELAMPAGO. *Mon. Wea. Rev.*, **150(9)**, 2317-2338. https://doi.org/10.1175/MWR-D-22-0049.1

Romatschke, U., and R. A. Houze, 2010: Extreme Summer Convection in South America. *Journal of Climate*, **23**, 3761–3791, https://doi.org/10.1175/2010JCLI3465.1.

——, and ——, 2013: Characteristics of Precipitating Convective Systems Accounting for the Summer Rainfall of Tropical and Subtropical South America. *Journal of Hydrometeorology*, **14**, 25–46, https://doi.org/10.1175/JHM-D-12-060.1.

Rondanelli, R., B. Hatchett, J. Rutllant, D. Bozkurt, and R. Garreaud, 2019: Strongest MJO on Record Triggers Extreme Atacama Rainfall and Warmth in Antarctica. *Geophysical Research Letters*, **46**, 3482–3491, https://doi.org/10.1029/2018GL081475.

Rydbeck, A. V., E. D. Maloney, S.-P. Xie, J. Hafner, and J. Shaman, 2013: Remote Forcing versus Local Feedback of East Pacific Intraseasonal Variability during Boreal Summer. *Journal of Climate*, **26**, 3575–3596, https://doi.org/10.1175/JCLI-D-12-00499.1.

Salio, P., M. Nicolini, and E. J. Zipser, 2007: Mesoscale Convective Systems over Southeastern South America and Their Relationship with the South American Low-Level Jet. *Monthly Weather Review*, **135**, 1290–1309, https://doi.org/10.1175/MWR3305.1.

——, and Coauthors, 2024: Toward a South American High-Impact Weather Reports Database. *Bulletin of the American Meteorological Society*, **105**, E1204–E1217, https://doi.org/10.1175/BAMS-D-23-0063.1.

Sasaki, C. R. S., A. K. Rowe, L. A. McMurdie, and K. L. Rasmussen, 2022: New Insights into the South American Low-Level Jet from RELAMPAGO Observations. *Monthly Weather Review*, **150**, 1247–1271, https://doi.org/10.1175/MWR-D-21-0161.1.

——, ——, ——, A. C. Varble, and Z. Zhang, 2024: Influences of the South American Low-Level Jet on the Convective Environment in Central Argentina Using a Convection-Permitting Simulation. *Monthly Weather Review*, **152**, 629–648, https://doi.org/10.1175/MWR-D-23-0122.1.

Schär, C., C. Frei, D. Lüthi, and H. C. Davies, 1996: Surrogate climate-change scenarios for regional climate models. *Geophysical Research Letters*, **23**, 669–672, https://doi.org/10.1029/96GL00265.

Schiro, K. A., J. D. Neelin, D. K. Adams, and B. R. Lintner, 2016: Deep Convection and Column Water Vapor over Tropical Land versus Tropical Ocean: A Comparison between the Amazon and the Tropical Western Pacific. *Journal of the Atmospheric Sciences*, **73**, 4043–4063, https://doi.org/10.1175/JAS-D-16-0119.1.

Schumacher, C., and R. A. Houze, 2003: Stratiform Rain in the Tropics as Seen by the TRMM Precipitation Radar. *Journal of Climate*, **16**, 1739–1756, https://doi.org/10.1175/1520-0442(2003)016<1739:SRITTA>2.0.CO;2.

Schumacher, R. S., D. A. Hence, S. W. Nesbitt, R. J. Trapp, K. A. Kosiba, J. Wurman, P. Salio, Rugna, A. C. Varble, and N. R. Kelly, 2021: Convective-storm environments in subtropical South America from high-frequency soundings during RELAMPAGO-CACTI. *Mon. Wea. Rev.*, **149**, 1439-1458. https://doi.org/10.1175/MWR-D-20-0293.1

Schumacher, R., and K. L. Rasmussen, 2020: The Formation, Character, and Changing Nature of Mesoscale Convective Systems. *Nature Reviews Earth and Environment*, **1**, 300-314. https://doi.org/10.1038/s43017-020-0057-7.

Schwarzkopf, M. L. A., 1988: Climatology of the effects of severe convection over Argentina (in Spanish). PhD Dissertation, Universidad de Buenos Aires, 91 pp, https://bibliotecadigital.exactas.uba.ar/download/tesis/tesis_n2211_AltingerdeSchwarzkopf.pdf

Schwarzkopf, M. L. A., and L. C. Rosso, 1993: Risk of tornadoes and downbursts in Argentina, ed.: INTI - CIRSOC, Department of Atmospheric Sciences, School of Exact and Natural Sciences, Universidad de Buenos Aires, Buenos Aires, Argentina, 35 pp. (in Spanish).

Sena, A. C. T., Y. Peings, and G. Magnusdottir, 2022: Effect of the Quasi-Biennial Oscillation on the Madden Julian Oscillation Teleconnections in the Southern Hemisphere. *Geophys. Res. Lett.,* **49**, e2021GL096105. https://doi.org/10.1029/2021GL096105

Sherburn, K. D., and M. D. Parker, 2014: Climatology and ingredients of significant severe convection in high-shear, low-CAPE environments. *Wea. Forecasting*, **29,** 854–877, https://doi.org/10.1175/WAF-D-13-00041.1.

Sherburn, K. D., M. D. Parker, J. R. King, and G. M. Lackmann, 2016: Composite Environments of Severe and Nonsevere High-Shear, Low-CAPE Convective Events. *Wea. Forecasting*, **31**, 1899–1927, https://doi.org/10.1175/WAF-D-16-0086.1.

Silva, G. A. M., and T. Ambrizzi, 2006: Inter- El Niño variability and its impact on the South American low- level jet east of the Andes during austral summer - two case studies. *Adv. Geosci*. **6**, 283–287. https://doi.org/10.5194/adgeo-6-283-2006

Silva Dias, M. A. F., 2011: An Increase in the Number of Tornado Reports in Brazil. *Weather, Climate, and Society*, **3**, 209–217, https://doi.org/10.1175/2011WCAS1095.1.

Skamarock, W. C., and Coauthors, 2019: A Description of the Advanced Research WRF Model Version 4.

Smith, B. T., R. L. Thompson, J. S. Grams, C.Broyles, C., and Brooks H. E. (2012). Convective modes for significant severe thunderstorms in the contiguous United States. Part I: Storm classification and climatology. *Wea. Forecasting*, **27**, 1114–1135, https://doi.org/10.1175/WAF-D-11-00115.1.

Solman, S. A., and J. Blázquez, 2019: Multiscale precipitation variability over South America: Analysis of the added value of CORDEX RCM simulations. *Clim Dyn*, **53**, 1547–1565, https://doi.org/10.1007/s00382-019-04689-1.

Stan, C., D. M. Straus, J. S. Frederiksen, H. Lin, E. D. Maloney, and C. Schumacher, 2017: Review of Tropical-Extratropical Teleconnections on Intraseasonal Time Scales. *Reviews of Geophysics*, **55**, 902–937, https://doi.org/10.1002/2016RG000538.

Straub, K. H., 2013: MJO initiation in the real-time multivariate MJO index. *J. Clim.,* **26**, 1130–1151, https://doi.org/10.1175/JCLI-D-12-00074.1.

Swain, D., O. Wing, P. Bates, J. Done, K. Johnson, and D. Cameron, 2020: Increased flood exposure due to climate change and population growth in the United States. *Earth's Future*, **8(11)**. https://doi.org/10.1029/2020EF001778

Subrahmanyam, K. V., K. K. Kumar, and A. Narendra Babu, 2015: Phase relation between CAPE and precipitation at diurnal scales over the Indian summer monsoon region. *Atmospheric Science Letters*, **16**, 346–354, https://doi.org/10.1002/asl2.566.

Swain, D. L., O. E. J. Wing, P. D. Bates, J. M. Done, K. A. Johnson, and D. R. Cameron, 2020: Increased Flood Exposure Due to Climate Change and Population Growth in the United States. *Earth's Future*, **8**, e2020EF001778, https://doi.org/10.1029/2020EF001778.

Taszarek, M., J. T. Allen, T. Púčik, K. A. Hoogewind, and H. E. Brooks, 2020: Severe Convective Storms across Europe and the United States. Part II: ERA5 Environments Associated with Lightning, Large Hail, Severe Wind, and Tornadoes. *Journal of Climate*, **33**, 10263–10286, https://doi.org/10.1175/JCLI-D-20-0346.1.

——, N. Pilguj, J. T. Allen, V. Gensini, H. E. Brooks, and P. Szuster, 2021: Comparison of Convective Parameters Derived from ERA5 and MERRA-2 with Rawinsonde Data over Europe and North America. *Journal of Climate*, **34**, 3211–3237, https://doi.org/10.1175/JCLI-D-20-0484.1.

Tompkins, A. M., 2001: Organization of Tropical Convection in Low Vertical Wind Shears: The Role of Water Vapor. *Journal of the Atmospheric Sciences*, **58**, 529–545, https://doi.org/10.1175/1520-0469(2001)058<0529:OOTCIL>2.0.CO;2.

Thompson, D. B., and P. E. Roundy, 2013: The relationship between the Madden–Julian oscillation and U.S. violent tornado outbreaks in the spring. *Mon. Wea. Rev.*, **141**, 2087–2095. https://doi.org/10.1175/MWR-D-12-00173.1

Thompson, R. L., R. Edwards, J. A. Hart, K. L. Elmore, and P. Markowski, 2003: Close proximity soundings within supercell environments obtained from the Rapid Update Cycle. *Wea. Forecasting*, **18(6)**, 1243–1261. https://doi.org/10.1175/1520-0434(2003)018<1243:CPSWSE>2.0.CO;2

Thompson, R. L., R. Edwards, and C. M. Mead, 2004: An update to the supercell composite and significant tornado parameters. In Preprints, *22nd Conf. on Severe Local Storms*, Hyannis, MA, Amer. Meteor. Soc. P (Vol. 8).

Thompson, R. L., B. T. Smith, J. S. Grams, A. R. Dean, and C. Broyles, 2012: Convective modes for significant severe thunderstorms in the contiguous United States. Part II: Supercell and QLCS tornado environments. *Wea. Forecasting*, **27**, 1136–1154, https://doi.org/10.1175/WAF-D-11-00116.1.

Tippett, M. K., 2018: Robustness of relations between the MJO and US tornado occurrence. *Mon. Wea. Rev.*, **146**, 3873–3884. https://doi.org/10.1175/MWR-D-18-0207.1

Tochimoto, E., 2022: Environmental controls on tornadoes and tornado outbreaks. *Atmosphere-Ocean*, 1-23. https://doi.org/10.1080/07055900.2022.2079472

Trapp, R. J., D. M. Wheatley, N. T. Atkins, R. W. Przybylinksi, and R. Wolf, 2006: Buyer beware: Some words of caution on the use of severe wind reports in postevent assessment and research. *Wea. Forecasting*, **21,** 408–415, https://doi.org/10.1175/WAF925.1.

Trenberth, K. E., A. Dai, R. M. Rasmussen, and D. B. Parsons, 2003: The Changing Character of Precipitation. *Bulletin of the American Meteorological Society*, **84**, 1205–1218, https://doi.org/10.1175/BAMS-84-9-1205.

Tuckman, P. J., and K. Emanuel, 2024: Origins of Extreme CAPE Around the World. *Journal of Geophysical Research: Atmospheres*, **129**, e2024JD041833, https://doi.org/10.1029/2024JD041833.

Tuholske, C., K. Caylor, C. Funk, A. Verdin, S. Sweeney, K. Grace, P. Peterson, and T. Evans, 2021: Global urban population exposure to extreme heat. *Proceedings of the National Academy of Sciences*, **118**, e2024792118, https://doi.org/10.1073/pnas.2024792118.

Varga, Á. J., and H. Breuer, 2022: Evaluation of convective parameters derived from pressure level and native ERA5 data and different resolution WRF climate simulations over Central Europe. *Clim Dyn*, **58**, 1569–1585, https://doi.org/10.1007/s00382-021-05979-3.

Varuolo-Clarke, A. M., A. P. Williams, J. E. Smerdon, M. Ting, and D. A. Bishop, 2022: Influence of the South American Low-Level Jet on the Austral Summer Precipitation Trend in Southeastern South America. *Geophysical Research Letters*, **49**, e2021GL096409, https://doi.org/10.1029/2021GL096409.

Velasco, I., and J. M. Fritsch, 1987: Mesoscale convective complexes in the Americas. *Journal of Geophysical Research: Atmospheres*, **92**, 9591–9613, https://doi.org/10.1029/JD092iD08p09591.

Veloso-Aguila, D., 2023: Tornado Reports in Southeast South America (Version 2) [Data set]. Zenodo. https://doi.org/10.5281/zenodo.7072781

Veloso-Aguila, D., K. L. Rasmussen, and E. D. Maloney, 2024: Tornadoes in Southeast South America: Mesoscale to Planetary-Scale Environments. *Monthly Weather Review*, **152**, 295–318, https://doi.org/10.1175/MWR-D-22-0248.1.

Vera, C., and Coauthors, 2006: The South American Low-Level Jet Experiment. *Bulletin of the American Meteorological Society*, **87**, 63–78, https://doi.org/10.1175/BAMS-87-1-63.

Viale, M., R. Valenzuela, R. D. Garreaud, and F. M. Ralph, 2018: Impacts of Atmospheric Rivers on Precipitation in Southern South America. *Journal of Hydrometeorology*, **19**, 1671–1687, https://doi.org/10.1175/JHM-D-18-0006.1.

Vicencio, J., R. Rondanelli, D. Campos., R. Valenzuela, R. D. Garreaud,, Reyes, A., Padilla, R., Abarca, R., Barahona, C., Delgado, R., and Nicora, G. (2021). The Chilean Tornado Outbreak of May 2019: Synoptic, Mesoscale, and Historical Contexts. *Bull. Amer. Meteor. Soc.*, **102(3)**, E611-E634. https://doi.org/10.1175/BAMS-D-19-0218.1

Virts, K. S., and R. A. Houze, 2015: Variation of Lightning and Convective Rain Fraction in Mesoscale Convective Systems of the MJO. *Journal of the Atmospheric Sciences*, **72**, 1932–1944, https://doi.org/10.1175/JAS-D-14-0201.1.

Wall, C., C. Liu, and E. Zipser, 2013: A climatology of tropical congestus using CloudSat. *Journal of Geophysical Research: Atmospheres*, **118**, 6478–6492, https://doi.org/10.1002/jgrd.50455.

Weisman, M. L., and J. B. Klemp, 1982: The Dependence of Numerically Simulated Convective Storms on Vertical Wind Shear and Buoyancy. *Monthly Weather Review*, **110**, 504–520, https://doi.org/10.1175/1520-0493(1982)110<0504:TDONSC>2.0.CO;2.

Westra, S., and Coauthors, 2014: Future changes to the intensity and frequency of short-duration extreme rainfall. *Reviews of Geophysics*, **52**, 522–555, https://doi.org/10.1002/2014RG000464.

Wheeler, M. C., and H. H. Hendon, 2004: An All-Season Real-Time Multivariate MJO Index: Development of an Index for Monitoring and Prediction. *Monthly Weather Review*, **132**, 1917–1932, https://doi.org/10.1175/1520-0493(2004)132<1917:AARMMI>2.0.CO;2.

Williams, E., and Coauthors, 2002: Contrasting convective regimes over the Amazon: Implications for cloud electrification. *Journal of Geophysical Research: Atmospheres*, **107**, LBA 50-1-LBA 50-19, https://doi.org/10.1029/2001JD000380.

Williams, E. R., S. G. Geotis, N. Renno, S. A. Rutledge, E. Rasmussen, and T. Rickenbach, 1992: A Radar and Electrical Study of Tropical "Hot Towers." *J. Atmos. Sci.*, **49**, 1386–1395, https://doi.org/10.1175/1520-0469(1992)049<1386:ARAESO>2.0.CO;2.

Yang, J., L. Hu, and C. Wang, 2019: Population dynamics modify urban residents' exposure to extreme temperatures across the United States. *Science Advances*, **5**, eaay3452, https://doi.org/10.1126/sciadv.aay3452.

Young, A. H., K. R. Knapp, A Inamdar, A., W. Hankins, and W. B. Rossow, 2018: The International Satellite Cloud Climatology Project H-Series climate data record product. *Earth Syst. Sci. Data*, **10**, 583–593. https://doi.org/10.5194/essd-10-583-2018.

Yu, H., 2022: yuhungjui/Cloud_System_Classification: v1.0, https://doi.org/10.5281/zenodo.6491940.

Yu, W., W. Han, E. D. Maloney, D. Gochis, and S.-P. Xie, 2011: Observations of eastward propagation of atmospheric intraseasonal oscillations from the Pacific to the Atlantic. *J. Geophys. Res.*, **116**, D02101, https://doi.org/10.1029/2010JD014336.

Zaninelli, P. G., C. G. Menéndez, M. Falco, N. López-Franca, and A. F. Carril, 2019: Future hydroclimatological changes in South America based on an ensemble of regional climate models. *Clim Dyn*, **52**, 819–830, https://doi.org/10.1007/s00382-018-4225-0.

Zhang, C., 2013: Madden–Julian Oscillation: Bridging Weather and Climate. *Bulletin of the American Meteorological Society*, **94**, 1849–1870, https://doi.org/10.1175/BAMS-D-12-00026.1.

Zhou, Y., W. K. M. Lau, and C. Liu, 2013: Rain characteristics and large-scale environments of precipitation objects with extreme rain volumes from TRMM observations. *Journal of Geophysical Research: Atmospheres*, **118**, 9673–9689, https://doi.org/10.1002/jgrd.50776.

Zilli, M. T., and Coauthors, 2024: The added value of using convective-permitting regional climate model simulations to represent cloud band events over South America. *Clim Dyn*, **62**, 10543–10564, https://doi.org/10.1007/s00382-024-07460-3.

Zipser, E. J., and C. Liu, 2021: Extreme Convection vs. Extreme Rainfall: a Global View. *Curr Clim Change Rep*, **7**, 121–130, https://doi.org/10.1007/s40641-021-00176-0.

Zipser, E. J., D. J. Cecil, C. Liu, S. W. Nesbitt, and D. P. Yorty, 2006: WHERE ARE THE MOST INTENSE THUNDERSTORMS ON EARTH? *Bull. Amer. Meteor. Soc.*, **87**, 1057–1072, https://doi.org/10.1175/BAMS-87-8-1057.

Zuluaga, M. D., and R. A. Houze, 2013: Evolution of the Population of Precipitating Convective Systems over the Equatorial Indian Ocean in Active Phases of the Madden–Julian Oscillation. *Journal of the Atmospheric Sciences*, **70**, 2713–2725, https://doi.org/10.1175/JAS-D-12-0311.1.

——, and ——, 2015: Extreme Convection of the Near-Equatorial Americas, Africa, and Adjoining Oceans as seen by TRMM. *Monthly Weather Review*, **143**, 298–316, https://doi.org/10.1175/MWR-D-14-00109.1.